UNIVERSIDAD NACIONAL AUTÓNOMA DE MÉXICO
PROGRAMA DE MAESTRÍA Y DOCTORADO EN INGENIERÍA
INGENIERÍA ELÉCTRICA – INSTRUMENTACIÓN

DEVELOPMENT OF COST-EFFECTIVE NANOPLASMONIC-BASED PLATFORMS FOR PORTABLE SENSING APPLICATIONS

TESIS
QUE PARA OPTAR POR EL GRADO DE:
DOCTOR EN INGENIERÍA

PRESENTA:
M. en I. Juan Manuel Gomez Cruz

TUTORES PRINCIPAL
Dr. Gabriel Ascanio Gasca
Instituto de Ciencias Aplicadas y Tecnología, UNAM
Dr. Carlos Roberto Escobedo Canseco
Department of Chemical Engineering, Queen´s University

CIUDAD DE MÉXICO, ABRIL 2021

JURADO ASIGNADO:

Presidente: Dr. Garduño Mejía Jesús

Secretario: Dr. Qureshi Naser

1 er. Vocal: Dr. Ascanio Gasca Gabriel

2 do. Vocal: Dr. Escobedo Canseco Carlos Roberto

3 er. Vocal: Dr. Docoslis Aristides

Lugar o lugares donde se realizó la tesis: Instituto de Ciencias Aplicadas y Tecnología, UNAM, Department of Chemical Engineering, Queen´s University.

TUTORES DE TESIS:

Dr. Gabriel Ascanio Gasca

FIRMA

Dr. Carlos Roberto Escobedo Canseco

FIRMA

(Segunda hoja)

Abstract

In the last decade, the need for faster, real-time and highly sensitive methods to characterize biomolecular interactions has yielded tremendous progress in the development of label-free biosensor techniques. The rapid progress in nanofabrication techniques and material science has propelled the development of novel nanostructures. Specifically, (bio)sensing is a critical field that nanostructured materials have impacted in recent years. Metallic nanostructures, such as nanohole arrays (NHAs) and crossed surface relief gratings (CSRGs), are able to couple incident light with the free electrons on the metallic surface, promoting a photonic phenomenon called surface plasmon resonance (SPR). SPR offers label-free sensing with high-sensitivity and reproducibility, providing the technique with noteworthy popularity as a commercial biomolecular analysis technique. However, commercial SPR systems involve complex optical setups that increase the cost and the size of the devices, making them impractical for portable point-of-care (POC) applications. NHAs and CSRGs offer all the advantages of the SPR technique, but with the possibility of collinear optics that reduce cost and allow for miniaturization.

In this dissertation, novel plasmonic nanostructures such as nanohole arrays and cross surface relief gratings were designed, investigated and characterized to evaluate their sensing and biosensing potential. Theoretical and simulation approaches were performed to evaluate the plasmonic effects of the fabrication parameters, such as size, material, and periodicity. The fabricated nanostructures were experimentally characterized and implemented on the SPR-based POC platforms presented in this thesis. The platforms are built with collinear optical setups consisting of off-the-shelf electronics and optical components. The applications demonstrated in this work include: 1) the development of a portable POC platform for the diagnosis of urinary tract infections (UTIs) using nanohole arrays and CSRGs — The platform allowed for the detection of pathogenic bacteria in clinically relevant concentrations in real-time analyte-analyte binding kinetic assays; 2) Variable pitch CSRGs evaluation for POC sensing applications; 3) Structural stability evaluation of flow-through NHAs; 4) A novel bioinspired template-stripped CSRGs (TS-CSRGs) demonstrated as a label-free surface-enhanced Raman scattering (SERS) substrates for biochemical sensing applications; 5) Study of diffusion kinetics of volatile organic compounds (VOC) on silicone-coated flow through NHAs for sensing applications. This dissertation demonstrates the potential of unique, miniaturized SPR-based POC platforms with high sensitivity and performance for several applications.

Co-Authorship

The PhD thesis has been prepared by Juan Manuel Gomez Cruz (J G-C) and reviewed by Dr. Carlos Escobedo according to the regulations for a manuscript format thesis by School of Graduate Studies at the Queen's University. The published articles and unpublished manuscripts in this thesis include collaborations between my supervisors, Dr. Carlos Escobedo and Dr. Gabriel Ascanio (*Instituto de Ciencias Aplicadas y Tecnolgía , Universidad Nacional Autónoma de México*, *UNAM*, *Mexico*) with Dr. Ribal Georges Sabat (Department of Physics and Space Science, Royal Military College of Canada, Kingston ON), Dr. Angel Manjarrez-Hernandez and Dr. Sandra Gavilanes-Parra (*Departamento de Salud Pública, Facultad de Medicina*, *UNAM*, *Mexico*), Dr. Eduardo Carrasco (*Universidad Politécnica de Madrid*, Spain), Dr. Aristides Docoslis (Department of Chemical Engineering, Queen's University, Kingston, ON, Canada), and Dr. Hans-Peter Loock (Department of Chemistry, University of Victoria, BC, Canada. Previously at Department of Chemistry, Queen´s University, Kingston, ON, Canada).

The work presented in this thesis also includes co-authorship with Srijit Nair (SN) and Yazan Bdour (YB) from the Escobedo research group, and Gaurav Verma (GV) and Jack A. Barnes (JB) from the Department of Chemistry, Queen´s University, Kingston, ON, Canada, and the contributions are detailed below:

Chapter 2: Flow-through nanohole array based sensor implemented on analogue smartphone components

J.G-C contributed with the conceptualization of the original idea, and all the numerical simulations and nanofabrication. SN contributed with J.G-C in experimental design, experimental work, data analysis and manuscript writing.

Chapter 3: Cost-effective flow-through nanohole array-based biosensing platform for the label-free detection of uropathogenic E. coli in real time

J.G-C contributed with the conceptualization of the original idea and all the numerical simulations. J.G-C contributed equally with SN in experimental design, experimental work, data analysis and manuscript writing.

Chapter 4: Selective Uropathogenic E. coli Detection Using Crossed Surface-Relief Gratings

J.G-C contributed equally with SN in experimental design, experimental work, data analysis and manuscript writing. SN further performed the fabrication of the nanostructures.

Chapter 5: Rapid label-free detection of intact pathogenic bacteria in situ via surface plasmon resonance imaging enabled by crossed surface relief gratings

J.G-C contributed with all the numerical simulations. J.G-C contributed equally with SN in experimental design, experimental work, data analysis and manuscript writing. SN further performed the fabrication of the nanostructures.

Chapter 6: Structural stability of optofluidic nanostructures in flow-through operation

J.G-C contributed equally with YB in experimental design, experimental work, data analysis and manuscript writing.

Chapter 7: Variable Pitch Crossed Surface Relief Gratings for Point-of-Care Sensing

J.G-C contributed with all the numerical simulations. J.G-C contributed equally with YB in experimental design, experimental work, data analysis and manuscript writing. YB further performed the fabrication of the nanostructures.

Chapter 8: Cicada Wing Inspired Template-Stripped SERS Active 3D Metallic Nanostructures for the Detection of Toxic Substances

J.G-C contributed with all the numerical simulations. J.G-C contributed equally with SN in experimental design, experimental work, data analysis and manuscript writing.

Chapter 9: Volatile Organic Compound Detection Using Silicone-Coated Metallic Flow-Through Nanohole Arrays

J. G-C contributed with the original conceptualization, and performed all the numerical simulations, experimental design, experimental work, data analysis and manuscript writing. GV contributed with experimental work and data analysis. JB contributed with mathematical modeling.

Acknowledgments

I would like to thank my supervisors, Professor Carlos Escobedo and Professor Gabriel Ascanio, for all these years of trust, guidance, and unconditional support. Thank you for giving me the opportunity to demonstrate my passion for research and always encouraging, inspiring, and reminding me why I love what I do. I also want to thank you so much for your friendship. All these years of incredible memories will stay with me forever.

This would not have been possible without my mom and dad, Aida and Juan, and my brothers, Osmar and Pepe. Thank you for being my motivation and inspiration, my guidance and support. I love you with all my heart, and I do not find enough words to tell you how lucky and grateful I am to have such a beautiful and amazing family. Brianna, thank you for your patience, incredible support, and love. Your beautiful smile and your lovely company make my days easier and shinier. Thank you for making me a better person, athlete, and cat lover every day. I love you!

Thank you to all my lab mates and friends in Mexico who have been part of this journey and a great support, especially Jorge, Isaac, Jenny, Jair, and Bruno. Thank you as well to my lab mates of the QuSENS lab and friends in Canada that have made me feel at home, especially to Yaz, Josh, Srijit, Hannah, Erica, Ryan, Praph, Prashant, Joe, Mary, Peyman, Connor, David, Eva and many, many more.

Thank you to the funding sources that contributed to the completion of my degree, including CONACyT, ELAP, UNAM, Queen’s University, and my supervisors. Finally, I am grateful for being part of two great institutions, Instituto de Ciencias Aplicadas y Tecnología, UNAM, and the Department of Chemical Engineering, Queen´s University. Thank you very much.

Agradecimientos

Quiero agradecer a mis supervisores, el Dr. Carlos Escobedo y el Dr. Gabriel Ascanio por todos estos años de confianza, guía y apoyo incondicional. Gracias por darme la oportunidad de demostrar mi pasión por la investigación, y por siempre alentarme, inspirarme y recordarme el por qué amo a lo que me dedico. Además, quiero agradecerles por su amistad. Todos estos años de increíbles recuerdos permanecerán siempre conmigo.

Todo esto no habría sido posible sin mi mamita y mi papito, Aida y Juan, y sin mis hermanitos, Osmar y Pepe. Muchas gracias por ser mi motivación e inspiración, mi guía y apoyo. Los amo con todo mi corazón, y no encuentro las palabras suficientes para demostrarles lo agradecido y afortunado que soy de tener una familia tan hermosa e increíble. Brianna, gracias por toda tu paciencia, increíble apoyo y amor. Tu hermosa sonrisa y tu encantadora compañía hacen que mis días sean más radiantes y fascinantes. Gracias por convertirme en amante de los gatos, y por hacerme una mejor persona y atleta cada día. ¡Te amo!

Gracias a todos mis compañeros de laboratorio y amigos en México que me han apoyado en esta experiencia. Especialmente gracias a Jorge, Isaac, Jenny, Jair, and Bruno. También muchas gracias a mis compañeros del laboratorio QuSENS y amigos en Canadá que me han hecho sentir como en casa. Especiales agradecimientos a Yaz, Josh, Srijit, Hannah, Erica, Ryan, Praph, Prashant, Joe, Mary, Peyman, Connor, David, Eva y muchos, muchos más.

Gracias a todos los que financiaron este proyecto, incluyendo a CONACyT, ELAP, UNAM, Queen´s University y mis supervisores. Finalmente, me encuentro sumamente agradecido de ser parte de dos grandes instituciones, Instituto de Ciencias Aplicadas y Tecnología, UNAM, y el Departamento de Ingeniería Química, Queen´s University. Muchas gracias.

Table of Contents

Abstract ... iii
Co-Authorship ... v
Acknowledgements ... viii
Agradecimientos ... ix
List of Figures ... xiv
List of Tables ... xx
Chapter 1 ... 2
  1.1 Motivation ... 2
  1.2 Maxwell equations ... 3
  1.3 Optical properties of metals ... 6
  1.3.1 Drude model ... 6
  1.3 Surface plasmon resonance (SPR) ... 8
  1.3.1 Surface plasmon polaritons (SPP) ... 9
  1.4 SPR in metallic nanostructures ... 14
  1.4.1 Metallic nanohole arrays ... 14
  1.4.2 Cross surface relief gratings ... 16
  1.4.3 SPR sensing ... 17
  1.4.4 Surface plasmon resonance imaging ... 19
  1.6 References ... 23
Chapter 2 ... 27
  2.1 Introduction ... 28
  2.2 Results and Discussion ... 30
  2.3 Conclusion ... 36
  2.4 References ... 37
Chapter 3 ... 40
  3.1 Introduction ... 41
  3.2 Experimental section ... 43
    3.2.1 Overview of the integrated sensing platform ... 43
    3.2.2 Fabrication of flow-through nanohole arrays ... 44
    3.2.3 Custom-made nanometric positioning system ... 45
    3.2.4 Bacterial culture ... 45
    3.2.5 Production of antibodies ... 45

3.2.6 Human urine preparation 46
3.3 Results and discussion 46
3.3.1 Nanohole arrays 46
3.3.2 Characterization of the custom-made nanometric positioning stage 49
3.3.3 Sensing test 49
3.3.4 Detection of uropathogenic E. coli 50
3.4 Conclusions 54
3.5 References 55
Chapter 4 59
4.1 Introduction 60
4.2 Materials and methods 62
4.2.1 Azo-glass film 62
4.2.2 CSRG Fabrication 63
4.2.3 Experimental Setup 63
4.2.4 Bacteria Culture 64
4.2.5 Antibody Production 64
4.2.6 Bulk RI Sensing Experiments 65
4.2.7 Bacterial Detection 65
4.3 Results and discussion 66
4.3.1 Crossed Surface-Relief Gratings 66
4.3.2 Optical Characterization 68
4.3.3 Bulk Refractive Index Sensing 69
4.3.3 Bacterial Detection 71
4.4 Conclusions 74
4.5 References 75
Chapter 5 80
5.1 Introduction 81
5.2 Materials and Methods 83
5.2.1 Fabrication of nanostructures 83
5.2.2 Experimental setup 85
5.2.3CSRGs topography and optical characterization 85
5.2.4 CSRGs FDTD simulations 86
5.2.5 Bulk RI sensing test 87
5.2.6 Bacterial detection 87

- 5.2.7 Bacterial culture 88
- 5.2.8 Antibody production 88
- 5.2.9 Human urine preparation 89
- 5.2.10 Dot-blot immunoassay 89
- 5.3.1 Crossed surface relief gratings (CSRGs) 89
- 5.3.2 Optical characterization 92
- 5.3.3 Quantitative detection of uropathogenic E. coli via CSRG-based SPRi 96

5.5 References 101

Chapter 6 106

6.1 Introduction 106

6.2 Materials and Methods 108
- 6.2.1 Fabrication of periodic through subwavelength apertures 108
- 6.2.2 Fabrication of microfluidic chips 108
- 6.2.3 Optofluidic Structure Deflection Analysis 109
- 6.3 Results and Discussion 111
- 6.4 Conclusions 118

6.4 References 119

Chapter 7 123

7.1 Abstract 123

7.2 References 125

Chapter 8 126

8.1 Introduction 127

8.2 Materials and Methods 129
- 8.2.1 Atomic Force Microscopy 129
- 8.2.2 Fabrication of Nanogratings 130
- 8.2.3 Template-Stripping Procedure 131
- 8.2.4 Raman Measurements 131
- 8.2.5 Analyte Sample Preparation 131
- 8.2.6 Contact Angle Measurements 132
- 8.2.7 Enhancement Factor Calculations 132
- 8.2.8 Finite-Difference Time-Domain (FDTD) simulations 133
- 8.2.9 Scanning Electron Microscopy 134

8.3 Results and Discussion 134

8.4 Conclusions 141

8.5 References 142
Chapter 9 148
9.1 Introduction 148
9.2 Materials and Methods 151
9.2.1 PDMS-coated flowthrough NHAs 151
9.2.2 Experimental setup 151
9.2.3 FDTD simulations 151
9.3 Results and Discussion 152
9.3.1 FDTD Model 152
9.3.2 VOC detection with PDMS-coated flow-through NHAs 154
9.3.3 Mole fraction model 155
9.4 Conclusions 159
9.5 References 160
Chapter 10 163
10.1 Conclusions 163
10.2 Future work 165
Appendix A 166
Dot blot immunoassay 166
References 167
Appendix B 168
SPR peak drift experiments 168
References 170
Appendix C 171
Contact angle measurements 171
Preparation and inspection of the TS-CSRG SERS substrates 172
Scanning Electron Microscopy (SEM) Characterization 173
References 173

List of Figures

Figure 1.1 Surface plasmons polaritons (SPPs). SPPs are electromagnetic waves, confined along the metal-dielectric interface. The energy in both the metal and the dielectric medium, decay exponentially with length $\boldsymbol{\delta m}$ and $\boldsymbol{\delta d}$, respectively. 10

Figure 1.2 A plot of the dispersion relation as a function of frequency. It can be seen from the dispersion curves that the momentum of the light traveling in a vacuum (black-dotted line) does not match the momentum of the surface plasmons in a flat semi-infinite metal surface (blue line). However, by using elements such as prisms (green line) or nanostructures such as gratings (red line), the momentum of the incident light can be modified so that the surface plasmons are excited, creating evanescent waves at the metal-dielectric interface. 14

Figure 1.3 Momentum matching of light to SPPs in NHAs. 16

Figure 1.4 Schematic representation of direct detection: the analyte is captured by the ligands immobilized on the sensor surface [40]. 18

Figure 1.5 EOT spectrum of a periodic nanohole array. The nanohole array is made of Au with a thickness of 200 nm, with hole size and the periodicity of 200 and 500 nm, respectively. Maximum and minimum peaks correspond to (1,0) and (1,1) resonance orders at the gold-air interface.[21] 19

Figure 1.6 SPR imaging principle. When a monochromatic light illuminates the NHAs, the spectral shifting causes a decrease in the intensity of the transmitted light. 20

Figure 1.7 Finite-difference time-domain (FDTD) Yee cell discretization. Each unit cell owns specific RI ($\boldsymbol{ni,j,k}$)[19,43] 21

Figure 2.1 Schematic of the SPR imaging experimental setup, displaying the experimental configuration for measuring light transmission through nine arrays of sub-wavelength holes. Magnified image shows the visualised image of nanohole arrays using white LED. 30

Figure 2.2 FDTD simulation results. (a) Electric ($|E|^2$) field intensity distributions calculated at the transmission peak (λ = 588 nm for air) for the nanohole arrays with periodicity = 520 nm and diameter = 260 nm (Scale bar = 100 nm). (b) Simulated transmission spectra for nanohole arrays when exposed to water and aqueous sucrose solutions of different concentrations (5% and 10%). 32

Figure 2.3 (a) Normalised spectra for smartphone (LG G3 STYLUS) flash LED and the white LED used in this work. (b) Line of best fit for a series of mean pixel intensities and bulk refractive index points, where the error bars represent the standard deviations for sample measurements. A linear fit of the pixel intensity units (PIU) vs. refractive index unit (RIU) of each solution characterizes the sensitivity of the sensor (266.08 PIU/RIU). 33

Figure 2.4 Time dependent streptavidin detection assay. (a) Observed real-time PIU shift versus streptavidin incubation time at 830 nM concentration. (b) Total shift in PIU observed after the addition of biotin and streptavidin to the cysteamine-SAM system, taking observed PIU after cysteamine-SAM formation as baseline. 35

Figure 3.1 Schematic representation (not to scale) of the biosensing SPRi platform, consisting of a CMOS detector, light source (LED, peak wavelength = 626 nm), flow-through nanohole array sensor and off-the-shelf optical elements. The optics, light source and nanohole array are contained in a customized holder of 45 cm3. The magnified images of an actual 9-window TEM grid and transmitted light through a nanohole array are shown. 43

Figure 3.2 (a) SEM image of the fabricated nanohole arrays with a periodicity of 560 nm and diameter of 280 nm. Scale bar indicates 1 µm. The inset shows the electric field intensity distribution obtained from FDTD simulations, using light source peak wavelength at λ = 626 nm. Scale bar indicates 100 nm. (b) White light transmission spectrum (raw data) from the nanohole arrays. 47

Figure 3.3 Bulk sensitivity test. Average pixel intensity (a.u.) values of the transmitted light from the nanohole arrays as a function of RI for water and sucrose solutions (10%, 15% and 20% in concentration). Actual images of the light intensity, corresponding to each RI, are shown as insets. The line of best fit yields a slope (i.e. sensitivity) of 212 pixel intensity/RIU. Standard deviations (N = 3) are smaller than the symbols representing data points. 51

Figure 3.4 Time-dependent uropathogenic *E. coli* detection assay. (a) Real-time relative intensity shift corresponding to detection of bacteria at a concentration of 109 CFU/ml. Three-dimensional renderings (not to scale) illustrate the scheme employed for bacteria detection. The inset shows the cumulative intensity shift observed after addition of anti-UPEC antibody and UPEC. (b) Relative intensity shift corresponding to different concentrations of UPEC in PBS buffer (103, 105, 106, 108, 109 CFU/ml; black squares; R2=0.947) and in human urine (105, 108 CFU/ml; red stars). Error bars indicate the standard deviation observed for each bacterial measurement for N = 3. 53

Figure 4.1 (a) Schematics of the fabrication procedure for CSRGs. (b) Normalized spectra for white LED used in this work. (c) AFM scan of 4 µm × 4 µm crossed region showing the orthogonally superimposed SRGs. (d) Actual image of the fabricated CSRGs with the crossed region marked with red box. White scale bar corresponds to 1 cm. 68

Figure 4.2 Schematic of the optical platform for transmission-based spectroscopy using CSRGs. All the elements are arranged in a collinear arrangement on a vertical rail. The light from the white LED passes through a variable iris, to control the spot diameter upon the horizontal polarizer, which is then incident on the CSRGs exciting the plasmons. The resulting out-coupled light then traverses the vertical polarizer, annulling all residual light from the white LED source, except the plasmonic signal detected by the spectrometer. 69

Figure 4.3 Bulk sensitivity test. (a) Normalized SPR peaks for water acquired using two different pitch CSRGs (450 nm and 550 nm). (b) Normalized SPR peaks for aqueous sucrose solutions of different concentrations (5%, 10%, 15% and 20%). The SPR spectrum shifts toward red as the refractive index increases. (c) Wavelength (nm) vs refractive index (RIU) for each solution. The sensitivity of the platform is 382.2 nm/RIU, based on the slope of the linear fit. No error bars are indicated since the standard deviation for $N = 3$ is smaller than the size of the symbol representing the mean in the graph. 71

Figure 4.4 Selective uropathogenic *E. coli* (UPEC) detection assay. (a) Real-time relative shift corresponding to capture of UPEC bacteria, and other UTI-causing Gram-negative bacteria at concentration 10^9 CFU/mL. Inset shows the relative cumulative shift in SPR signal observed after binding of UPEC-specific antibody and UPEC. (b) Relative shift corresponding to different concentrations of UPEC in PBS buffer (10^5, 10^7, 10^9 CFU/mL). Error bars indicate the standard deviation observed for each bacterial measurement for $N = 3$. 74

Figure 5.1 a) Signal quality (Intensity/FWHM) for transmitted SPR signal acquired from metallic CSRG fabricated on azo-glass thin film spin-coated on glass slides at different RPMs (800, 1000 and 1200). The dielectric medium in contact with the metallic CSRG was water (RI = 1.330). Error bars represent the standard deviation (n = 3). b) AFM scan of the CSRG (scan area = 5 µm × 5 µm) displaying the surface topography (pitch = 450 nm, depth c.a. 75 nm). Scale bar represents 500 nm. c) Schematic of the optical assembly for SPRi measurements. 92

Figure 5.2 FDTD simulations and control experiments using PBS and changes in bulk RI. a) Isometric view of the simulation environment. b) Simulated electric field enhancement $|EE0|2$ for : (Top) plain gold surface (Bottom) CSRG for air (RI = 1) as the dielectric medium. White scale bar = 100 nm. c) Top-bottom represents simulated electric field enhancement $|EE0|2$ for CSRG at $\lambda = 613$ nm for increasing refractive indices (RI = 1.330 to 1.357). d) Relative intensity variation of the acquired signal using PBS solution as control, for four independent measurements (n = 8). e) Experimental bulk refractive index sensing plot representing the data points for transmitted intensity vs. the refractive indices of the test solutions. Actual acquired images are shown as inset. The slope of the linear fit represents the sensitivity of the platform, with a value of ~ 613 pixel intensity/RIU. Error bars (n = 3) are smaller than the size of the symbol representing the mean in the graph. 95

Figure 5.3 Quantification and evaluation of selective UPEC capture and detection. a) Plot represents the real-time binding of the UPEC-specific antibody (t = 1 min to 16 min) and UPEC at 10^9 CFU/mL in PBS (t > 16 min) via corresponding shift in pixel intensity observed over time. Error bars represent the standard deviation (n=3). (inset) Schematic depiction of the biodetection scheme, where bacteria are captured by immobilized antibodies on the CSRG surface. b) Relative transmitted light intensity change for *Klebsiella pneumonia*, *Proteus mirabilis* and *Pseudomonas aeruginosa*, in comparison to UPEC. The experiments were conducted using the same bacterial concentration and procedure of detection in all cases. Error bars represent standard deviation (n = 3). (Inset) Dot-blot affinity immunoassay of anti-*E. coli* antibody for Gram-negative bacteria. From left to right: positive control, uropathogenic *E. coli* (UPEC), *Klebsiella pneumonia*, *Pseudomonas aeruginosa* and *Proteus mirabilis*." 97

Figure 5.4 Standard calibration curve for selective detection of UPEC for concentrations ranging from 10^3 to 10^9 CFU/mL. Signals are obtained by flowing UPEC suspensions in both PBS (black triangle) and human urine (red circles) at different concentrations over UPEC-specific antibodies immobilized on the CSRG surface. Some of the error bars (n = 3) are comparable to the size of the symbol representing the mean. . 99

Figure 6.1 Schematic representation of the experimental setup. 111

Figure 6.2 Membrane deflection before and after the application of a pressure of 20 psi. Scale bar represents 100 μm. 114

Figure 6.3 Experimental, theoretical and simulation results of the maximum membrane deflection (apex). Error bars indicate standard deviation (n = 5). 116

Figure 7.1 a) AFM image of the VP-CSRG (top) and the model used for the FDTD simulations (bottom). b) Simulation results for p- and s-polarized light in the x- and y-directions along 540-nm-pitch VP-CSRGs. 125

Figure 8.1 (a) Picture of a cicada *Neotibicen canicularis*. (b) atomic force microscope (AFM) image of the external surface from a piece of the wing of the cicada; inset: wetting state of a water droplet on a cicada *Neotibicen canicularis.* (c) AFM image of the external surface of the wing of a cicada *Cryptotympana atrata fabricius*. Reprinted with permission.[48] Copyright 2017, The Royal Society of Chemistry. (d) Schematic representation of the fabrication procedure for creating template-stripped Ag template-stripped crossed surface relief grating (TS-CSRG). AFM scan of a 5 µm × 5 µm area of a 500-nm-pitch (e) Ag CSRG, and (f) Ag TS-CSRG; inset: wetting state of a water droplet on an Ag TS-CSRG; scale bars correspond to 1 µm. (g) SEM image of a 500 nm-pitch Ag TS-CSRG. 135

Figure 8.2 Finite-difference time-domain (FDTD) simulations. (a) 3D surface created from Equation (3). (b) FDTD simulation model. (c–f) Electric field distribution along *xy* cross-section for Ag TS-CSRGs with grating pitch spanning from 450 nm to 600 nm, with 50 nm increments. 139

Figure 8.3 Surface-enhanced Raman scattering (SERS) activity of Ag TS-CSRG. (a) Pitch-dependency of SERS spectra for R6G (10^{-5} M) with pitches ranging 450 nm to 600 nm, and for a flat Ag substrate for R6G (10^{-2} M). (b) Average SERS spectra of melamine on Ag TS-CSRG for concentrations ranging from 1 ppm to 1000 ppm. 140

Figure 9.1 Schematic representation (not to scale) of the NHA sensor covered with a thin layer (d = 10 µm) of PDMS. The analyte flows from the PDMS surface (y = 0) to the NHA (y = d). δd corresponds to the maximum amplitude of the evanescent plasmonic wave. 150

Figure 9.2 FDTD simulations showing the electric field intensity distribution around the rim of the NHA since these regions are the most sensitive to changes in RIs. The response was mapped at λ = 680 nm (a) cross-section. (b) x-y plane. 153

Figure 9.3 Schematic representation (not to scale) of the experimental setup for VOC sorption measurements. Xylene vapours were generated in a glass bubbler by flowing nitrogen gas to generate saturated solvent vapours. Saturated vapours and pure nitrogen were directed to the chamber containing the NHA (inset) for absorption and desorption experiments, respectively. Inset: photograph and schematic of the chamber containing the NHA.. 155

Figure 9.4 (a) Comparison between simulated (dotted red line) and experimental spectra (solid blue line). The transmission spectrum shift was performed by tracking the centroid of the signal, which lies within the simulation maxima range. Inset: characterization curve of the sensor utilized to calculate the RI changes of the xylene sorption into the PDMS. (b) Centroid wavelength change over time for xylene sorption experiments. 156

Figure 9.5 (a). Comparison between the experiment mole fraction values (black dots), and the mathematical fitting under a free-standing membrane model (red stars), supported membrane model (blue triangles), and the linear combination of both models (green squares) (b) Residuals corresponding to the mathematical model approximation and the experimental data. (c) Comparison of the mathematical model fitting corresponding to three different experiments performed under the same conditions. 159

Figure A.1 Dot blot anti-E. coli Ab affinity immunoassay results for the Gram-negative bacteria uropathogenic *E. coli* (UPEC), *Klebisella pneumonia*, *Pseudomonas aeruginosa*, and *Proteus mirabilis* (red dashed circles facilitate the view of the dots of the last three).. 166

Figure B.1 Relative shift in SPR peak recorded for water from t = 0 min to t = 20 minutes, with 30-seconds interval between signal acquisition. 169

Figure B.2 Relative shift in SPR peak recorded for PBS solution from t = 0 min to t = 20 minutes, with 30-seconds interval between signal acquisition. 169

Figure B.3 Relative shift in SPR peak recorded for bound streptavidin on immobilized biotin-cysteamine complex on CSRGs surface from t = 0 min to t = 20 minutes, with 1-minute interval between signal acquisition.. 170

Figure C.1 Images taken during contact angle measurements of a DI water droplet atop the surface of a) a piece of wing from a cicada Neotibicen canicularis (inset: cicada used as sample source); and b) an Ag TS-CSRG (inset: TS-CSRG, left; AFM scan, right)... 171

Figure C.2 CSRGs template stripping process. a) Silver-coated CSRG structure. b) Glass slide and CSRG structure after spin coating and UV exposure. c) TS-CSRG structures. 172

Figure C.3 SEM images of the Ag TS-CSRGs with pitches of a) 450 nm, b) 500 nm, c) 550 nm and d) 600 nm. 173

List of Tables

Table 3.1 Calibration of the custom-made nanometric positioning stage (N=3). 48
Table A.1 Relative intensity-based quantification of dot blot immunoassay using ImageJ software....... 167

To my beloved family

A mi amada familia

Chapter 1

Introduction

1.1 Motivation

The need for rapid, accurate, and accessible healthcare and environmental monitoring, as well as *in situ* medical diagnoses, has led to the growing impetus in the global scientific community to develop portable and cost-effective biosensing technologies. Current laboratory methods such as enzyme-linked immunoassay (ELISA) offer a low detection limit and high sensitivity. Yet, high qualified personnel and specialized facilities are necessary to perform the diagnoses.[1] Innovative solutions for accurate, sensitive and more accessible health care monitoring, such as point-of-care (POC) diagnostics platforms, are taking advantage of recent advances in nanotechnology, microfluidics, electronics, and imaging systems to assist the evolution of sensing devices.[2,3] POC platforms have already shown their potential in medical diagnosis by providing fast and accurate results in a nanolaboratory setting, reducing costs associated with facilities, trained personnel and sample volumes.[1] The rapid evolution of POC devices is supported by a remarkable growth of the demand, a market valued at US$19 billion in 2019 and predicted to reach US$ 24 billion by 2027.[3,4]

Progress in the field of nanoplasmonics has motivated the development of (bio)sensing technologies based on metallic nanostructures supporting surface plasmon resonances (SPRs), that can be easily tracked using spectroscopic means. Nanohole arrays (NHAs) and cross surface relief gratings (CSRGs) in metallic films, particularly, offer several advantages compared to the traditional prism-based SPR techniques,[5] including portable detection due to their inherent compact size, compatibility with collinear optics, and ease of integration with other microtechnologies, such as microfluidics. Additionally, NHAs and CSRGs enable monitoring of near-surface adsorption events (e.g., analyte detection) via SPR imaging (SPRi) by quantifying the intensity variation from transmitted monochromatic beams.[6–8] Most SPRi-based sensing demonstrations dedicated to real-world applications up until now, including the detection of infectious diseases, have employed bulky and costly setups involving microscope-based assemblies and charge-couple device (CCD) modules.[9–11] Smart devices can be considered among the best-suited candidates for the development of the next generation of POC platforms, with their current advanced multicore processing capability, sophisticated user interfaces, and powerful imaging processing.[12,13] However, smartphones are not configured for chemical sensing or (bio)sensing, which typically involves the transport and detection of specific analytes, providing a timely opportunity to develop sensing platforms compatible with smart devices.[13]

The motivation of this thesis is to design and develop handheld, consumer-ready, cost-effective, and smartphone-based POC diagnostic platforms through the study of plasmonic nanostructures such as flow-through metallic NHAs and CSRGs using theoretical, computational and experimental approaches. The following sections provide the necessary information to dive into the applications shown in the next chapter.

1.2 Maxwell equations

The way that metallic nanostructes interact with electromagnetic (EM) fields, can be described using the same classical EM theory employed for macroscopic metals, the Maxwell's equations. The high density of free electron of nanostructures results in minute spacings of the electron energy levels compared to thermal excitations of energy at room temperature.[14] In a region of space with no free charge or current, these equations take the following form:

$$\nabla \cdot \mathbf{D} = \rho_{ext} \tag{1.1}$$

$$\nabla \cdot \mathbf{B} = 0 \tag{1.2}$$

$$\nabla \times \mathbf{E} = -\frac{\partial \mathbf{B}}{\partial t} \tag{1.3}$$

$$\nabla \times \mathbf{H} = \frac{\partial \mathbf{D}}{\partial t} \tag{1.4}$$

where **E** and **H** are the electric and magnetic intensities of the electromagnetic field, respectively. The magnetic flux density, **B,** and the dielectric displacement, **D**, are parameters related to the material response. For a linear, isotropic, and nonmagnetic medium, two constitutive equations can be defined:

$$\mathbf{D} = \varepsilon_r \varepsilon_0 \mathbf{E} \tag{1.5}$$

$$\mathbf{B} = \mu_r \mu_0 \mathbf{H} \tag{1.6}$$

were $\mu_0 = 4\pi \times 10^{-7}\ \mathrm{H/m}$ and $\varepsilon_0 = 8.854 \times 10^{-12}\ \mathrm{F/m}$ correspond to the magnetic permeability and electric permittivity of free space, respectively, and μ_r and ε_r are the relative magnetic permeability and electrical permittivity of the material, respectively. For non-magnetic materials, operated at optical frequencies — such as the materials investigated in this dissertation — it can be considered that $\mu_r = 1$ so that $\mathbf{B} = \mu_0\mathbf{H}$. Equation (1.5) shows that electrons within a material will respond under the influence of an electric field, **E**. This external field will induce an electric polarization density, **P**. If the material has a linear behavior respect to **E** and **D**:

$$\mathbf{D} = \varepsilon_r \varepsilon_0 \mathbf{E} = \varepsilon_0 \mathbf{E} + \mathbf{P} \tag{1.7}$$

Metallic materials are dispersive, meaning that light travels at different speeds as a function of frequency. To understand this dispersive nature, the wave equation of the EM field must be considered. Combining equations (1.3) and (1.4), and assuming a time-harmonic behavior, a general solution for the wave equation is:

$$\mathbf{E}(\mathbf{r},t) = E_0 e^{\mathrm{k}\cdot\mathrm{r}-i\omega t} \tag{1.8}$$

where **K** is the wavevector of the plane wave and ω is the frequency of the wave. Knowing that the divergence and curl of the electric field can be expressed in terms of the wavevector:

$$\nabla \cdot \mathbf{E} = i\mathrm{k} \cdot \mathbf{E} \tag{1.9}$$

$$\nabla \times \mathbf{E} = i\mathrm{k} \times \mathbf{E} \tag{1.10}$$

The Fourier domain wave equation results:

$$k(k \cdot E) - k^2 E = -\varepsilon(k,\omega)\frac{\omega^2}{c^2}E \tag{1.11}$$

where $c = \frac{1}{\sqrt{\varepsilon_0 \mu_0}}$ is the speed of light in a vacuum. For transverse waves, $K \cdot E = 0$, the dispersion relation can be expressed as: [14]

$$k^2 = -\varepsilon(\mathrm{k},\omega)\frac{\omega^2}{c^2} \tag{1.12}$$

Additionally, for longitudinal waves, $k(k \cdot E) - k^2 E = 0$, equation (1.11) implies that:

$$\varepsilon(k,\omega) = 0 \tag{1.13}$$

The dispersion relation describes the effects of the dispersion that an EM wave experiences when propagating within a medium by relating the wave vector and the frequency of the wave. The wavenumber can also be related to the wavelength via $\lambda = \frac{2\pi}{k}$.

1.3 Optical properties of metals

The optical properties of metals are commonly described by their index of refraction, n, and the extinction coefficient, κ. The refractive index (RI) describes the ratio between the phase velocity of light traveling in a vacuum, and the phase velocity of light traveling in the material. Likewise, the extinction coefficient corresponds to the exponential decay of the EM wave as it passes through the material.[15,16] However, this is for the specific case when the materials interact with wavelengths corresponding to the optical part of the electromagnetic spectrum — generally encompassed from 10 nm to 10^3 nm.[17] To better understand the optical properties of metals, we need to understand a more general classification of materials which is conductors and insulators, depending on their permittivity and conductivity. Materials with a large amount of loss inhibit the propagation of EM waves and are considered conductors. Contrarily, materials with low loss that allow the propagation of EM waves are considered dielectrics. Metals fall into the category of good conductors.[18]

1.3.1 Drude model

In 1900, Paul Drude proposed a model to explain the kinetics properties of electrons in metals. He described metals as an arrangement of immovable positive ions, surrounded by a dense layer of delocalized free electrons — also called a free electron cloud.[15,18] In this model, the electrons, with a mass m and charge e, are treated from a harmonic oscillator model perspective. Thus, under the influence of an external time-varying electric field, $\mathbf{E}(t)$, the electron position, $\mathbf{x}(t)$ can be described as:

$$m\ddot{\mathbf{x}}(t) + m\gamma\dot{\mathbf{x}}(t) = -e\mathbf{E}(t) \tag{1.14}$$

where γ is a damping parameter defined as the inverse of the average time between electron collisions ($\gamma = 1/\tau$).[19–21] For an incident time-varying electric field — such as a light wave — $\mathbf{E}(t) = \mathbf{E}_0 e^{-i\omega t}$, the electrons will also respond to the harmonic time dependence $\mathbf{x}(t) = \mathbf{x}_0 e^{-i\omega t}$,[14] and the solution for the equation (1.1) becomes:

$$\mathbf{x}(t) = \frac{e\mathrm{E}(t)}{m(\omega^2 + i\gamma\omega)} \tag{1.15}$$

The macroscopic electric polarization, $\mathbf{P}(t)$, that depends on the displacement of electrons, becomes:

$$\mathbf{P}(t) = -n_e e\mathbf{x}(t) = \frac{n_e e^2 \mathbf{E}(t)}{m(\omega^2 + i\gamma\omega)} \tag{1.16}$$

where n_e is the electron density. Using equation (1.16) in equation (1.7), the dielectric displacement, **D,** can be given by:

$$\mathbf{D} = \varepsilon_0 \mathbf{E} + \mathbf{P} = \varepsilon_0 \left(1 - \frac{{\omega_p}^2}{\omega^2 + i\gamma\omega}\right)\mathbf{E} \tag{1.17}$$

where ω_p corresponds to the plasma frequency of the free electron gas, defined as:

$$\omega_p = \sqrt{\frac{n_e e^2}{\varepsilon_0 m}} \tag{1.18}$$

ω_p describes the transition frequency of a material between its dielectric and metallic behaviour.[19,20] Finally, using equation (1.4), the dielectric function of the free electron gas in metals, also called "Drude model" is:

$$\varepsilon_r(\omega) = 1 - \frac{{\omega_p}^2}{\omega^2 + i\gamma\omega} \tag{1.19}$$

where the real and imaginary components of the dielectric function, $\varepsilon_r(\omega) = \varepsilon_{r1}(\omega) + i\varepsilon_{r2}(\omega)$, are:

$$\varepsilon_{r1}(\omega) = 1 - \frac{{\omega_p}^2\tau^2}{1 + \omega^2\tau^2} \tag{1.20}$$

$$\varepsilon_{r2}(\omega) = \frac{{\omega_p}^2\tau}{\omega(1 + \omega^2\tau^2)} \tag{1.21}$$

1.3 Surface plasmon resonance (SPR)

Plasma is a state of matter with equal amounts of positive and negative charges in which at least one charge type is mobile. In the specific case of metals, the plasma is comprised of the free electrons populating the surface (i.e., mobile charges), which are balanced by the positive metal ion cores (i.e., immobile charges). A plasmon is the quantization of the plasma, defined as the collective oscillation of those free electrons, at the surface of the material.[22]

1.3.1 Surface plasmon polaritons (SPP)

As observed in equation (1.19), the dielectric function depends on the excitation frequency, ω. The analysis of this thesis will be limited to optical frequencies, $\omega \gg \gamma$, where $\varepsilon_r(\omega)$ is predominantly real, and the region $\omega < \omega_p$ allows metals to retain their metallic properties:

$$\varepsilon_r(\omega) \approx 1 - \frac{{\omega_p}^2}{\omega^2} \tag{1.22}$$

From equation (1.22), three cases can arise: 1) When $\omega > \omega_p$, $\varepsilon_r(\omega) > 0$, and thus k yields a real value, meaning that the metal will behave as a dielectric, allowing the propagation of electromagnetic waves through it. 2) If $\omega = \omega_p$, then $\varepsilon_r(\omega) = 0$ and $k = 0$; in this case, longitudinal oscillations, called "volume plasmons", are promoted in the material. This means that the electrons in the material oscillate in phase with the plasma frequency.[20] 3) Finally, the condition when $\omega < \omega_p$, $\varepsilon_r(\omega) < 0$, causes k to be complex. This means that transverse electromagnetic waves will not be able to propagate through the metal, but decay exponentially away from the surface, known as an evanescent field, resulting in surface plasmons (SPs). SPs are free electron density fluctuations that, collectively and coherently, oscillate at the interface of a metal and a dielectric. Surface plasmon polaritons (SPPs), are surface plasmons that are excited and coupled by an incident photon (electromagnetic wave), traveling at the metal-dielectric interface.

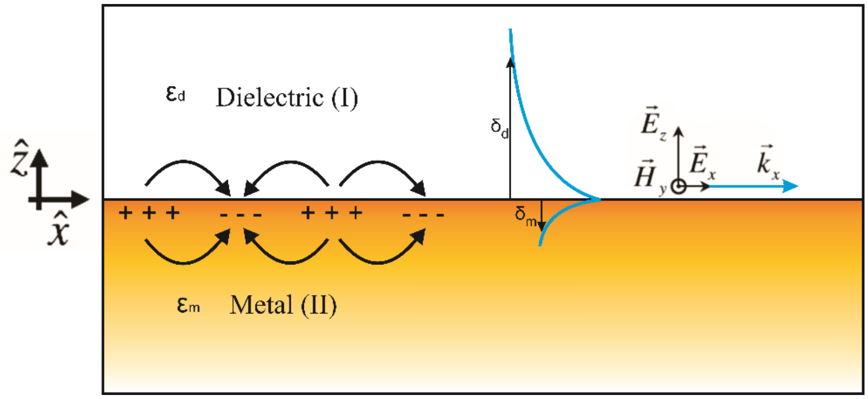

Figure 1.1 Surface plasmons polaritons (SPPs). SPPs are electromagnetic waves, confined along the metal-dielectric interface. The energy in both the metal and the dielectric medium, decay exponentially with length $\boldsymbol{\delta_m}$ and $\boldsymbol{\delta_d}$, respectively.

The magnetic and electric fields of an electromagnetic wave — which are solutions to the wave equation —, that propagates in a transverse magnetic (TM) polarization at the interface between two media along the *x*-direction, can be defined into two regions (Figure 1.1):

Region I

$$\mathbf{H}_I = (0, A, 0)e^{-ik_x x}e^{-ik_z{}^I z}e^{-i\omega t} \tag{1.23}$$

$$\mathbf{E}_I = \frac{-A}{\varepsilon_0 \varepsilon_I \omega}(k_z{}^I, 0, k_x)e^{-ik_x x}e^{-ik_z{}^I z}e^{-i\omega t} \tag{1.24}$$

Region II

$$\mathbf{H}_{II} = (0, B, 0)e^{-ik_x x}e^{-ik_z{}^{II} z}e^{-i\omega t} \tag{1.25}$$

$$\mathbf{E}_{II} = \frac{-A}{\varepsilon_0 \varepsilon_I \omega}(k_z{}^{II}, 0, k_x)e^{-ik_x x}e^{-ik_z{}^{II} z}e^{-i\omega t} \tag{1.26}$$

At the metal-dielectric interface, z=0, the boundary conditions establish that $(\mathrm{H}_x)_I = (\mathrm{H}_x)_{II}$, and $(\mathrm{E}_x)_I = (\mathrm{E}_x)_{II}$, hence:

$$\frac{{k_z}^I}{\varepsilon_I} = \frac{{k_z}^{II}}{\varepsilon_{II}} \tag{1.27}$$

$${k_x}^{\boldsymbol{I}} = {k_x}^{\boldsymbol{II}} = k_x \tag{1.28}$$

and taking into consideration the dispersion relation in each medium:

$$(k_x)^2 + ({k_z}^I)^2 = \frac{\omega^2}{c^2}\varepsilon_I \tag{1.29}$$

$$(k_x)^2 + ({k_z}^{II})^2 = \frac{\omega^2}{c^2}\varepsilon_{II} \tag{1.30}$$

Therefore, the dispersion relation of our system can be defined:

$${k_z}^I = \sqrt{\varepsilon_I \frac{\omega^2}{c^2} - (k_x)^2} \tag{1.31}$$

$${k_z}^{II} = \sqrt{\varepsilon_{II} \frac{\omega^2}{c^2} - (k_x)^2} \tag{1.32}$$

$$k_x = k_{SPP} = \frac{\omega}{c}\sqrt{\frac{\varepsilon_I \varepsilon_{II}}{\varepsilon_I + \varepsilon_{II}}} \tag{1.33}$$

where $\varepsilon_I = \varepsilon_d$, $\varepsilon_{II} = \varepsilon_m$.The subscripts, *d* and *m*, are assigned for the dielectric and metallic media, respectively. $k_0 = \frac{\omega}{c}$ is the wave number in vacuum. For the existence of a confined and propagating wave decaying within both media, the real part of k_x, equation (1.33), must be non-zero and the imaginary part of both ${k_z}^I$ and ${k_z}^{II}$, equations (1.31) and (1.32), must be also different from zero. That implies that for the two materials $\varepsilon_m = \varepsilon'_m + i\varepsilon''_m$, where $|\varepsilon'_m| \gg \varepsilon''_m$ and $|\varepsilon'_m| > \varepsilon_d$. Thus, the wave vector, equation (1.33) becomes $k_{spp} = k'_{spp} + ik''_{spp}$: [21,23]

$$k'_{spp} = \frac{\omega}{c}\sqrt{\frac{\varepsilon_d \varepsilon'_m}{\varepsilon_d + \varepsilon'_m}} \tag{1.34}$$

$$k''_{spp} = \frac{\omega}{c}\left(\frac{\varepsilon_d \varepsilon'_m}{\varepsilon_d + \varepsilon'_m}\right)^{3/2} * \left(\frac{\varepsilon''_m}{2(\varepsilon'_m)^2}\right) \tag{1.35}$$

Different parameters that describe the characteristics of a plasmonic structure can be calculated from equations (1.34) and (1.35). The surface plasmon polariton wavelength (λ_{SPP}), for instance, is a parameter that predicts the resonance frequency or wavelength of the plasmonic response and can be calculated as follows:

$$\lambda_{spp} = \frac{2\pi}{k'_{spp}} \tag{1.36}$$

Substituting equation (1.34) into (1.36), the SPP wavelength can be approximated to:

$$\lambda_{spp} \approx \lambda_0 \sqrt{\frac{\varepsilon_d + \varepsilon'_m}{\varepsilon_d * \varepsilon'_m}} \tag{1.37}$$

where $\lambda_0 = \frac{\omega}{c}$, and ε'_m and ε_d correspond to the real part of the dielectric function of the metal, and the permittivity of the dielectric material, respectively.

On the other hand, the length at which the energy carried by the SPP decays by a factor of 1/e is called absorption length and is defined as $L_{spp} = [2k''_{spp}]^{-1}$, leading to the following expression:

$$L_{spp} = \lambda_0 \frac{(\varepsilon'_m)^2}{2\pi * \varepsilon''_m} \tag{1.38}$$

From equation (1.38), it can be concluded that a metal with a large (negative) real part of the relative permittivity is “better” for guiding resonant waves. Finally, the electromagnetic field decay length in the dielectric and metal are defined by $\delta_d = [{k_z}^I]^{-1}$ and $\delta_m = [{k_z}^{II}]^{-1}$, respectively. These parameters provide the quantities for the length scale over which the SPP is sensitive to the presence of changes in refractive index and the penetration depth into the metal.

As seen before, SPPs are collective electronic oscillation travelling along the metal-dielectric interface occurring when the momentum of incident light matches the momentum of the free electrons of the metallic surface — a condition also known as surface plasmon resonance (SPR). Incident light travelling in vacuum cannot directly couple the SPPs of a flat semi-infinite metallic surface. This can be observed in Figure 1.2, where the dispersion curve of the light in vacuum does not touch the dispersion curve of the surface plasmons in the metal. However, there are methods to provide additional momentum to couple the surface plasmons to the incident light.[24] Traditionally, this has been achieved using prism-based coupling (e.g., Kretschmann and Otto configurations) where the attenuated total internal reflection (TIR) at the prism-metal interface creates an electric field that matches the SPP momentum, Figure 1.2. Another way to promote this momentum matching is using nanostructured materials such as gratings, Figure 1.2— a technology that falls in the field of nanoplasmonics.[25] This method provides multiple advantages such as high-sensitivity, miniaturization and reduction of optical components. Nanoplasmonics is a field that is constantly improving along with the nanofabrication techniques. This work was limited to the study and application of nanostructured materials such as nanohole arrays (NHAs) and cross surface relief gratings (CSRGs).

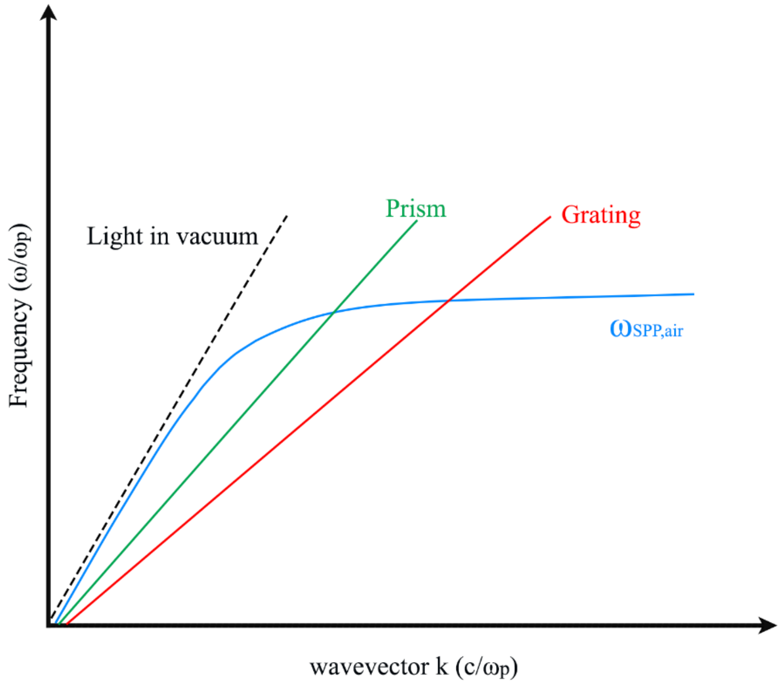

Figure 1.2 A plot of the dispersion relation as a function of frequency. It can be seen from the dispersion curves that the momentum of the light traveling in a vacuum (black-dotted line) does not match the momentum of the surface plasmons in a flat semi-infinite metal surface (blue line). However, by using elements such as prisms (green line) or nanostructures such as gratings (red line), the momentum of the incident light can be modified so that the surface plasmons are excited, creating evanescent waves at the metal-dielectric interface.

1.4 SPR in metallic nanostructures

1.4.1 Metallic nanohole arrays

Recent advances in nanofabrication methods have facilitated the creation of different types of nanostructures with unusual properties. Nanostructured metals are of particular interest because they can be resonantly excited by visible light to produce surface plasmon (SP) oscillations. These nanostructures allow the manipulation of the properties of SPs by tailoring their geometric parameters. Specifically, nanohole arrays, which support extraordinary optical transmission (EOT), can be modified in pitch (distance between nanoholes) and hole diameter to modify their resonance wavelength.[26,27]

1.4.1.1 Extraordinary optical transmission

Classical theory for metallic nanoapertures in thin metallic films, developed by Beth,[28] was able to describe the diffraction of light at a given wavelength (λ) through a circular hole of radius (r). Beth showed that when the radius is much smaller than the wavelength (r<< λ) the transmission efficiency T(λ) scales by: [29]

$$T(\lambda) = \frac{64}{27\pi^2}(kr)^4 \tag{1.39}$$

where $k = \frac{2\pi}{\lambda}$, which indicates that the transmission is proportional to the fourth power of r/λ. Thus, for hole size smaller than the wavelength of the incident light, the transmission is extremely weak.

In the late 1990s, Ebbesen et al. discovered an unusual optical transmission effect while working with periodic arrays of subwavelength apertures fabricated in metal films. They reported a remarkable intensity enhancement of the transmitted light at certain wavelengths, which exceeded the intensity predicted by Beth's diffraction theory. This phenomenon was called extraordinary optical transmission (EOT). [23,28,30–32]

EOT is directly related to the excitation of SPPs. In this context, periodic metallic NHAs, increase the momentum of the incident photons, Figure 1.3, allowing the excitation of SPPs at the metal-dielectric interface:[20,28]

$$k_{ssp} = k_x + iG_x + jG_y \tag{1.40}$$

where k_{ssp} is the SPP wavevector, $k_x = k_0 sin\theta$ is the *x* component of the wavevector of the incident light, as seen in section 1.3.1. $G_x = G_y = \frac{2\pi}{a}$ are the grating momentum wavevectors for a square array, where a is the periodicity of the grating, and *i* and *j* are the diffraction orders of the grating. If the incidence of light is normal with respect to the surface, the spectral position of the transmission maxima can be predicted using equation (1.40):[23,28]

$$\lambda_{SSP} = \frac{a}{\sqrt{i^2 + j^2}} * \sqrt{\frac{\varepsilon_d \varepsilon_m'}{\varepsilon_d + \varepsilon_m'}} \tag{1.41}$$

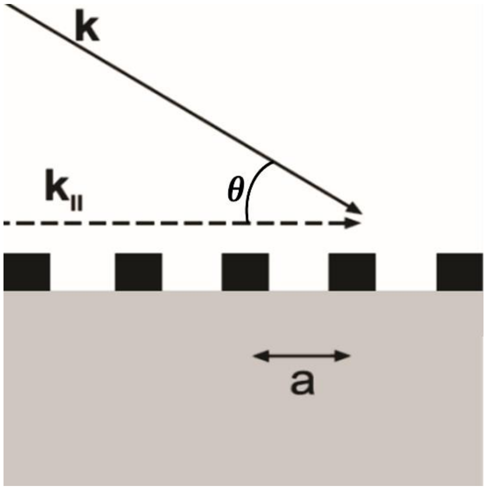

Figure 1.3 Momentum matching of light to SPPs in NHAs.

1.4.2 Cross surface relief gratings

Similar to nanohole arrays, cross surface relief grating (CSRGs), are nanostructures that help to modify the momentum of the incident light to match with the momentum of the SPPs at the metal-dielectric interface. The grating equation, written in terms of the wavenumber, is:

$$k\sin(\theta_m) = k\sin(\theta_i) \pm \frac{2\pi m}{\Lambda} \tag{1.42}$$

where $k\sin(\theta_i)$ and $k\sin(\theta_m)$ correspond to vector components of the incident and diffracted light respectively, m is the diffraction order, and the term $\frac{2\pi}{\Lambda}$ is the magnitude of the grating vector. If at normal incidence, equation (1.34) and (1.42) can be equated, and by solving for the light wavelength where the surface plasmon occurs (λ_{SPP}), the approximation yields:[33]

$$\lambda_{spp} = n_d \Lambda \left(\sqrt{\frac{\varepsilon_d + \varepsilon_m'}{\varepsilon_d * \varepsilon_m'}} \pm \sin(\theta_i) \right) \tag{1.43}$$

SPR propagation on perpendicular bi-gratings has shown that a polarization conversion of the incident light occurs.[34] When linearly polarized light incides on a bi-grating, an SPR will be excited by the grating having a vector aligned with the initial light polarization. Due to the transparency of the metal layer caused by the resonant electrons, this SPR resonant light will be re-radiated by the crossed grating in its orthogonal polarization, seen as a sharp positive wavelength peak at the transmitted light. When placed in between crossed polarizers, the light transmitted through a CSRG will be zero except in the narrow bandwidth where the SPR conversion has occurred.

1.4.3 SPR sensing

Optical sensors are devices that measure, transduce and track the interaction of light with matter through changes in properties of a light wave, such as intensity or phase shifting.[35] In SPR sensors, a change in RI at the metal-dielectric interface, results in a change of the coupling conditions of the incident light and the SPPs, modifying the characteristic resonance of the system. Depending on the light source used, SPR-based sensors can be classified into four types: angle shifting, wavelength shifting, intensity change, or polarization change. SPR sensors can provide a quantitative measurement by means of near-surface RI changes. Combined with selective functionalization chemistry for analyte detection[36] and microfluidic systems these sensors can perform innumerable tests such as affinity and kinetics analyses, solute or analyte concentration interrogation, and the study of binding mechanisms.[37–39]

As sensing elements, NHAs and CSRGs present unique advantages, including a high level of reproducibility, small footprint, multiplexing capabilities and collinear optical integration, which makes them well-suited for integration into microfluidic platforms.[32] From section 1.3.1, it can be observed that electromagnetic field decay length into the dielectric media is around 100 – 500 nm for wavelengths within the visible range. This particularity makes SPR nanostructures highly sensitive to changes in RI at the near-surface, allowing for surface chemistry modifications for the recognition of specific biomolecules. In order to change the local RI to study molecular binding interactions, a ligand is generally fixed at the surface of the metal. The subsequent recognition of the analyte by the functionalized surface produces a change in local RI (Figure 1.3), resulting in a peak-shift of the resonance wavelength, which is related to a proportional change in the concentration of analytes bound on the surface.[21]

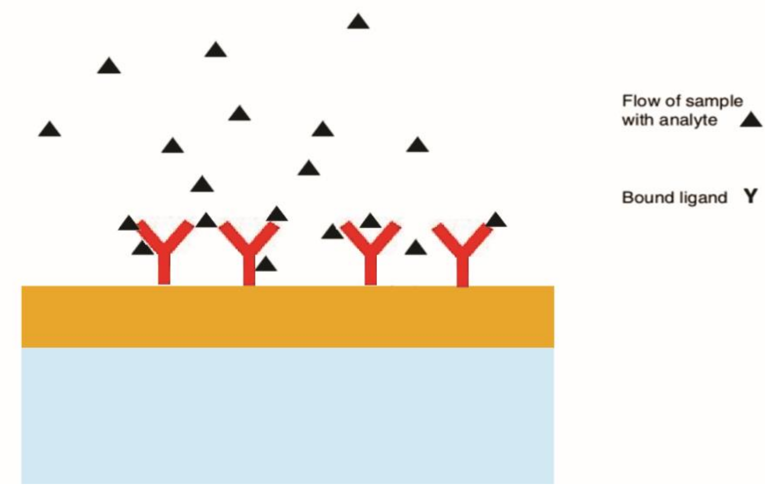

Figure 1.4 Schematic representation of direct detection: the analyte is captured by the ligands immobilized on the sensor surface [40].

1.4.4 Surface plasmon resonance imaging

In section 1.4.1.1, the use of equation (1.41) to predict the resonance behavior of a square lattice of metallic NHAs was explained, showing the sensitivity dependence on RI changes. The resonance region is strongly governed by several parameters that can be used to optimize the signal, including the periodicity of the nanostructure, the thickness of the metallic film, as well as the hole size and shape. Figure 1.4 shows the transmission spectrum of NHAs of 200 nm in diameter and 500 nm in periodicity, fabricated in a film of Au with 200 nm thickness. The minimum and maximum of the peaks depend either on the destructive or constructive interference of the SPPs excited on the surface of the nanostructure.[21,41]

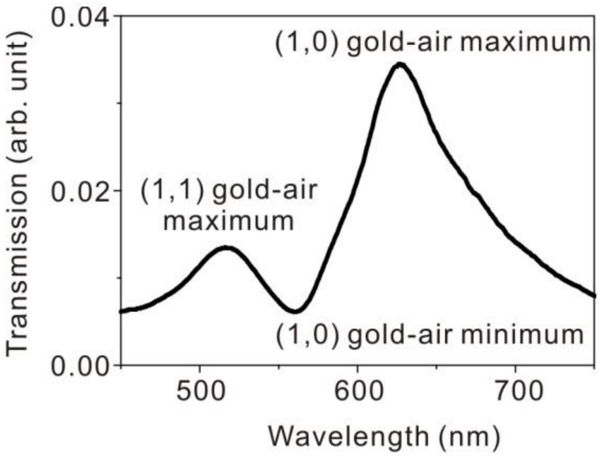

Figure 1.5 EOT spectrum of a periodic nanohole array. The nanohole array is made of Au with a thickness of 200 nm, with hole size and the periodicity of 200 and 500 nm, respectively. Maximum and minimum peaks correspond to (1,0) and (1,1) resonance orders at the gold-air interface.[21]

One of the advantages of using NHAs as sensors in transmission mode is the ability to excite and acquire a response of the plasmonic surface with a collinear optical system normal to the incidence plane. When the properties of the dielectric in contact with the metallic surface change, either as a change in bulk or local RI, a spectroscopic measurement can be obtained by tracking the position of the resonance peak. This spectral shifting, which usually occurs to the right of the electromagnetic spectrum for increments in the RI, Figure 1.5, enables observation of near-surface events in real-time. However, when the surface is illuminated with a monochromatic source, instead of a broadband light source, the spectral shifting can be interrogated by the change in intensity of the transmitted light. This method is known as surface plasmon resonance imaging (SPRi). The light intensity change can be effectively monitored using a CCD or a complementary metal-oxide-semiconductor (CMOS) detector. Figure 1.5 shows the SPR and SPRi response of gold-coated NHAs with a hole size of 200 nm and periodicity of 400 nm. Under quasi-monochromatic light excitation, the transmission intensity of the nanoholes will be reduced with an increase in the solution RI as a consequence of the right-shift spectral response.

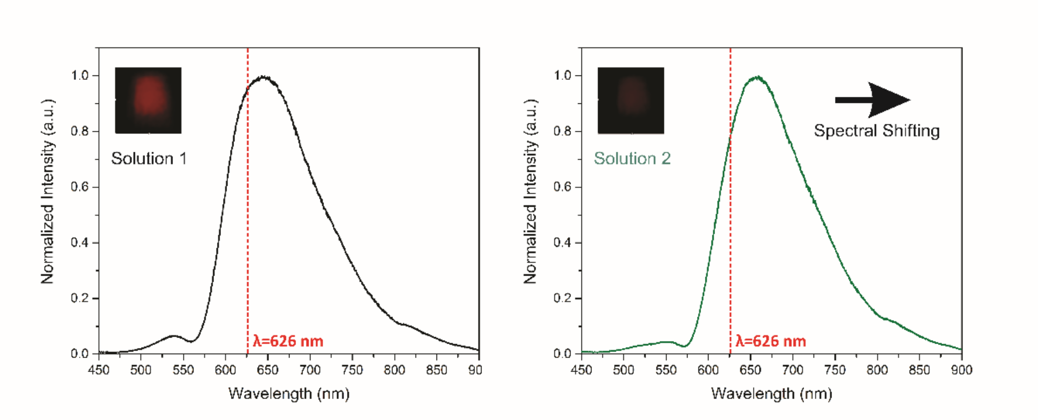

Figure 1.6 SPR imaging principle. When a monochromatic light illuminates the NHAs, the spectral shifting causes a decrease in the intensity of the transmitted light.

1.5 Finite-difference time-domain (FDTD)

It is critical to examine different parameters in computational simulations when designing nanostructured based plasmonic sensors. Analytical solutions to Maxwell's equations for simple and symmetric structures are well established. For complex geometries, Maxwell's equations are solved numerically. In 1966 Yee, proposed a "simple" method for obtaining numerical solutions to the time-dependent Maxwell's equations through a set of finite-difference equations. [42,43] This method, which was called finite-difference time-domain (FDTD), demonstrated to readily provide numerical solutions for electromagnetic problems involving propagation and scattering in complex media such as dispersive, anisotropic, and nonlinear media. FDTD belongs to a class of grid-based differential time-domain numerical method, focused on solving Maxwell´s equations (in a partial differential form) with no approximations but the discretization of the structures[23]. The FDTD method divides a three-dimensional problem structure into cells to form a grid. Each individual cell is called Yee cell, Figure 1.6, and allows the analysis of complicated systems into multiple simpler structures representing Maxwell's equations in discrete form, both in space and time.[44] The accuracy of the FDTD method relies on the size of the Yee cells, which in turn, depends on computational power capabilities.[43]

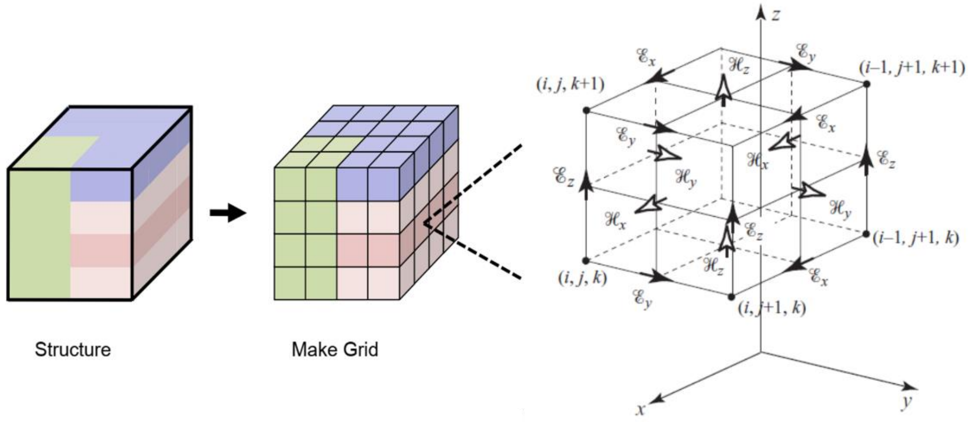

Figure 1.7 Finite-difference time-domain (FDTD) Yee cell discretization. Each unit cell owns specific RI ($\boldsymbol{n_{i,j,k}}$)[19,43]

Within the Yee cell, the electric field vector components are placed parallel to the edges at the center of the cell. The magnetic field vector components are placed orthogonally in the center of the cells' faces. Additionally, each cell (i, j, k) has a specific refractive index $n_{i,j,k}$ and the Yee cell accounts for the curl behavior of the electric and magnetic field components.[19] FDTD method considers the temporal change in the electric, **E**, related to the spatial change in the magnetic field, **M**, by combining equations (1.4) with (1.5) and (1.6). For an isotropic medium:[42,44]

$$\nabla \times \mathrm{E} = -\mu_r \mu_0 \frac{\partial \mathrm{H}}{\partial t} \tag{1.44}$$

$$\nabla \times \mathrm{H} = \varepsilon_r \varepsilon_0 \frac{\partial \mathrm{E}}{\partial t} \tag{1.45}$$

Therefore, for a three-dimensional cartesian coordinate system, there will be six scalar equations equivalent to Maxwell's equations. For E_x:

$$\frac{\partial \mathbf{E}_x}{\partial t} = \frac{1}{\varepsilon_0 \varepsilon_x}\left(\frac{\partial \mathbf{H}_z}{\partial y} - \frac{\partial \mathbf{H}_y}{\partial z}\right) \tag{1.46}$$

following the same procedure for the five remaining field components, E_y, E_z, H_x, H_y, H_z. Finally, using the central difference discretization, equations of the following form are obtained (for E_x):[43,44]

$$\begin{aligned} &\frac{\mathbf{E}_x^{\,n+1}\left(i+\frac{1}{2}, j, k\right) - \mathbf{E}_x^{\,n}(i+\frac{1}{2}, j, k)}{\Delta t} \\ &= \frac{1}{\varepsilon_0 \varepsilon_{x(i+\frac{1}{2},j,k)}} \frac{H_z^{\,n+\frac{1}{2}}\left(i+\frac{1}{2}, j+\frac{1}{2}, k\right) - H_z^{\,n+\frac{1}{2}}(i+\frac{1}{2}, j-\frac{1}{2}, k)}{\Delta y} \\ &- \frac{1}{\varepsilon_0 \varepsilon_{x(i+\frac{1}{2},j,k)}} \frac{H_y^{\,n+\frac{1}{2}}\left(i+\frac{1}{2}, j, k+\frac{1}{2}\right) - H_y^{\,n+\frac{1}{2}}(i+\frac{1}{2}, j, k-\frac{1}{2})}{\Delta z} \end{aligned} \tag{1.47}$$

1.6 References

(1) Nayak, S.; Blumenfeld, N. R.; Laksanasopin, T.; Sia, S. K. Point-of-Care Diagnostics: Recent Developments in a Connected Age. Analytical Chemistry. American Chemical Society January 3, 2017, pp 102–123. https://doi.org/10.1021/acs.analchem.6b04630.

(2) Tokel, O.; Inci, F.; Demirci, U. Advances in Plasmonic Technologies for Point of Care Applications. Chem. Rev. 2014, 114 (11), 5728–5752. https://doi.org/10.1021/cr4000623.

(3) Vashist, S. Point-of-Care Diagnostics: Recent Advances and Trends. Biosensors 2017, 7 (4), 62. https://doi.org/10.3390/bios7040062.

(4) Point of Care Diagnostics Market, POC Testing Report, 2027 https://www.grandviewresearch.com/industry-analysis/point-of-care-poc-diagnostics-industry (accessed Jan 17, 2021).

(5) Homola, J.; Piliarik, M. Surface Plasmon Resonance (SPR) Sensors. In Springer Ser Chem Sens Biosens; Springer, Berlin, Heidelberg, 2006; Vol. 4, pp 45–67. https://doi.org/10.1007/5346_014.

(6) Kim, I. T.; Kihm, K. D. Label-Free Visualization of Microfluidic Mixture Concentration Fields Using a Surface Plasmon Resonance (Spr) Reflectance Imaging. Exp. Fluids 2006, 41 (6), 905–916. https://doi.org/10.1007/s00348-006-0210-1.

(7) Lesuffleur, A.; Im, H.; Lindquist, N. C.; Lim, K. S.; Oh, S.-H. Laser-Illuminated Nanohole Arrays for Multiplex Plasmonic Microarray Sensing. Opt. Express 2008, 16 (1), 219. https://doi.org/10.1364/OE.16.000219.

(8) Escobedo, C.; Vincent, S.; Choudhury, A. I. K.; Campbell, J.; Brolo, A. G.; Sinton, D.; Gordon, R. Integrated Nanohole Array Surface Plasmon Resonance Sensing Device Using a Dual-Wavelength Source. J. Micromechanics Microengineering 2011, 21 (11), 115001. https://doi.org/10.1088/0960-1317/21/11/115001.

(9) Peterson, A. W.; Halter, M.; Tona, A.; Plant, A. L. High Resolution Surface Plasmon Resonance Imaging for Single Cells. BMC Cell Biol. 2014, 15 (1), 35. https://doi.org/10.1186/1471-2121-15-35.

(10) Shpacovitch, V.; Temchura, V.; Matrosovich, M.; Hamacher, J.; Skolnik, J.; Libuschewski, P.; Siedhoff, D.; Weichert, F.; Marwedel, P.; Müller, H.; Überla, K.; Hergenröder, R.; Zybin, A. Application of Surface Plasmon Resonance Imaging Technique for the Detection of Single Spherical Biological Submicrometer Particles. Anal. Biochem. 2015, 486, 62–69. https://doi.org/10.1016/j.ab.2015.06.022.

(11) Soler, M.; Belushkin, A.; Cavallini, A.; Kebbi-Beghdadi, C.; Greub, G.; Altug, H. Multiplexed Nanoplasmonic Biosensor for One-Step Simultaneous Detection of Chlamydia Trachomatis and Neisseria Gonorrhoeae in Urine. Biosens. Bioelectron. 2017, 94, 560–567. https://doi.org/10.1016/j.bios.2017.03.047.

(12) Vashist, S. K.; Mudanyali, O.; Schneider, Em.; Zengerle, R.; Ozcan, A. Cellphone-Based Devices for Bioanalytical Sciences. Analytical and bioanalytical chemistry. May 2014, pp 3263–3277. https://doi.org/10.1007/s00216-013-7473-1.

(13) Preechaburana, P.; Suska, A.; Filippini, D. Biosensing with Cell Phones. Trends Biotechnol. 2014, 32 (7), 351–355. https://doi.org/10.1016/j.tibtech.2014.03.007.

(14) Maier, S. A. Plasmonics : Fundamentals and Applications, 1st ed.; Springer US, 2007. https://doi.org/10.1007/0-387-37825-1.

(15) Ehrenreich, H. The Optical Properties of Metals. IEEE Spectr. 1965, 2 (3), 162–170. https://doi.org/10.1109/MSPEC.1965.5531773.

(16) Hass, G.; Hadley, L. Optical Properties of Metals. In Optics; p 42.

(17) Stillman, G. E. 21 - Optoelectronics. In Reference Data for Engineers (Ninth Edition); Middleton, W. M., Van Valkenburg, M. E., Eds.; Newnes: Woburn, 2002; pp 21–31. https://doi.org/https://doi.org/10.1016/B978-075067291-7/50023-6.

(18) Sabat, R. G. PH503: Advanced Optics, Royal Military College of Canada, 2017.

(19) Lindquist, N. C. Engineering Metallic Nanostructures for Surface Plasmon Resonance Sensing. 2010.

(20) Lee, S. H. Large-Scale Engineered Metallic Nanstructures for High-Throughput Surface Plasmon Resonance Biosensing and Surface-Enhanced Raman Spectroscopy. 2012.

(21) Im, H. Metallic Nanostructures and Plasmonic Devices for Surface Plasmon Resonance Biosensing. 2011.

(22) Ritchie, R. H. Plasma Losses by Fast Electrons in Thin Films. Phys. Rev. 1957, 106 (5), 874–881. https://doi.org/10.1103/PhysRev.106.874.

(23) Rodrigo, S. G. Optical Properties of Nanostructured Metallic Systems: Studied with the Finite-Difference Time-Domain Method; Springer Theses; Springer Berlin Heidelberg, 2011.

(24) Aizpurua, J.; Hillenbrand, R. Localized Surface Plasmons: Basics and Applications in Field-Enhanced Spectroscopy. Springer Ser. Opt. Sci. 2012, 167, 151–176. https://doi.org/10.1007/978-3-642-28079-5_5.

(25) Homola, J.; Yee, S. S.; Gauglitz, G. Surface Plasmon Resonance Sensors: Review. Sensors Actuators B Chem. 1999, 54 (1–2), 3–15. https://doi.org/10.1016/S0925-4005(98)00321-9.

(26) Sinton, D.; Gordon, R.; Brolo, A. G. Nanohole Arrays in Metal Films as Optofluidic Elements: Progress and Potential. Microfluid. Nanofluidics 2008, 4 (1–2), 107–116. https://doi.org/10.1007/s10404-007-0221-0.

(27) Gordon, R.; Sinton, D.; Kavanagh, K. L.; Brolo, A. G. A New Generation of Sensors Based on Extraordinary Optical Transmission. Acc. Chem. Res. 2008, 41 (8), 1049–1057. https://doi.org/10.1021/ar800074d.

(28) Ebbesen, T. W.; Lezec, H. J.; Ghaemi, H. F.; Thio, T.; Wolff, P. A. Extraordinary Optical Transmission through Sub-Wavelength Hole Arrays. Nature 1998, 391 (6668), 667–669.

(29) Yue, W.; Wang, Z.; Yang, Y.; Li, J.; Wu, Y.; Chen, L.; Ooi, B.; Wang, X.; Zhang, X. Enhanced Extraordinary Optical Transmission (EOT) through Arrays of Bridged Nanohole Pairs and Their Sensing Applications. Nanoscale 2014, 6 (14), 7917–7923. https://doi.org/10.1039/C4NR01001A.

(30) Genet, C.; Ebbesen, T. W. Light in Tiny Holes. Nature 2007, 445 (7123), 39–46.

(31) Foudeh, A. M.; Fatanat Didar, T.; Veres, T.; Tabrizian, M. Microfluidic Designs and Techniques Using Lab-on-a-Chip Devices for Pathogen Detection for Point-of-Care Diagnostics. Lab Chip 2012, 12 (18), 3249–3266. https://doi.org/10.1039/C2LC40630F.

(32) Escobedo, C. On-Chip Nanohole Array Based Sensing: A Review. Lab on a Chip. Royal Society of Chemistry July 7, 2013, pp 2445–2463. https://doi.org/10.1039/c3lc50107h.

(33) Bailey, E. SURFACE PLASMON POLARITON BANDWIDTH INCREASE USING CHIRPED-PITCH LINEAR DIFFRACTION GRATINGS FABRICATED ON AZOBENZENE THIN FILMS, Division of Graduate Studies of the Royal Military College of Canada, 2017.

(34) Bryan-Brown, G. P.; Sambles, J. R.; Hutley, M. C. Polarisation Conversion through the Excitation of Surface Plasmons on a Metallic Grating. J. Mod. Opt. 1990, 37 (7), 1227–1232. https://doi.org/10.1080/09500349014551301.

(35) Iniewski, K. Optical, Acoustic, Magnetic, and Mechanical Sensor Technologies; Devices, Circuits, and Systems; Taylor & Francis, 2012.

(36) Oliverio, M.; Perotto, S.; Messina, G. C.; Lovato, L.; De Angelis, F. Chemical Functionalization of Plasmonic Surface Biosensors: A Tutorial Review on Issues, Strategies, and Costs. ACS Appl. Mater. Interfaces 2017, 9 (35), 29394–29411. https://doi.org/10.1021/acsami.7b01583.

(37) de Mol Marcel J. E. Fischer, N. J. Surface Plasmon Resonance; Methods in Molecular Biology; Humana Press, 2010.

(38) Singh, P. Surface Plasmon Resonance; Nanotechnology Science and Technology; Nova Science Publishers, Incorporated, 2014.

(39) Homola, J. Surface Plasmon Resonance Based Sensors; Springer Series on Chemical Sensors and Biosensors; Springer Berlin Heidelberg, 2006.

(40) Kooyman, R. P. H.; Corn, R. M.; Wark, A.; Lee, H. J.; Gedig, E.; Engbers, G.; Walstrom, L.; de Mol, N. J.; Hall, D. R.; Yager, P.; Chinowsky, T.; Fu, E.; Nelson, K.; McWhirter, A.; Fischer, M. J. E.; Lokate, A. M. C.; Beusink, J. B.; Pruijn, G. J. M.; Knoll, W.; Kasry, A.; Liu, J.; Neumann, T.; Niu, L.; Park, H.; Paulsen, H.; Robelek, R.; Yu, F.; Schuck, P.

Handbook of Surface Plasmon Resonance; Schasfoort, R. B. M., Tudos, A. J., Eds.; The Royal Society of Chemistry, 2008. https://doi.org/10.1039/9781847558220.

(41) Otte, M. A.; Sepúlveda, B.; Ni, W.; Juste, J. P.; Liz-Marzán, L. M.; Lechuga, L. M. Identification of the Optimal Spectral Region for Plasmonic and Nanoplasmonic Sensing. ACS Nano 2010, 4 (1), 349–357. https://doi.org/10.1021/nn901024e.

(42) Yee, K. S. Numerical Solution of Initial Boundary Value Problems Involving Maxwell's Equations in Isotropic Media. IEEE Transactions on Antennas and Propagation. 1966, pp 302–307. https://doi.org/10.1109/TAP.1966.1138693.

(43) Inan, U. S.; Marshall, R. A. Numerical Electromagnetics: The FDTD Method; Cambridge University Press, 2011.

(44) Elsherbeni, A.; Demir, V. The Finite Difference Time Domain for Electromagnetics: With Matlab Simulations; Aces Series on Computational Electromagnetics and Engineering; SciTech Publishing Incorporated, 2016.

Chapter 2

Flow-through nanohole array based sensor implemented on analogue smartphone components

With minor changes to fulfill formatting requirements, this chapter is as it appears in: Juan Gomez-Cruz, Srijit Nair, Gabriel Ascanio, Carlos Escobedo. SPIE digital library, 2017, 10346, 1034624-1 – 1034624-7.

Abstract: Mobile communications have massively populated the consumer electronics market over the past few years and it is now ubiquitous, providing a timeless opportunity for the development of smartphone-based technologies as point-of-care (POC) diagnosis tools.[1] The expectation for a fully integrated smartphone-based sensor that enables applications such as environmental monitoring, explosive detection and biomedical analysis has increased among the scientific community in the past few years.[2,3] The commercialization forecast for smartphone-based sensing technologies is very promising, but reliable, miniature and cost-effective sensing platforms that can adapt to portable electronics in still under development. In this work, we present an integrated sensing platform based on flow-through metallic nanohole arrays. The nanohole arrays are 260 nm in diameter and 520 nm in pitch, fabricated using Focused Ion Beam (FIB) lithography. A white LED resembling a smartphone flash LED serves as light source to excite surface plasmons and the signal is recorded via a Complementary Metal-Oxide-Semiconductor (CMOS) module. The sensing abilities of the integrated sensing platform is demonstrated for the detection of (i) changes in bulk refractive index (RI), (ii) real-time monitoring of surface modification by receptor-analyte system of streptavidin-biotin.

2.1 Introduction

The high demand for the development of simple, cost-effective and time-saving devices for applications related to health care, clinical diagnosis and environmental monitoring represents a challenge for the scientific community and it still needs to be approached.[4] Innovative solutions, predominantly for point-of-care (POC) diagnostics platforms, are taking advantage of recent advances in mobile technologies, nanotechnology, imaging systems, and microfluidic technologies to assist this transformation[1]. In this context, mobile devices such as smartphones, which have massively populated the consumer electronics market with sales to end users close to 1.5 billion units, just in 2016,[5] can be considered among the best-suited candidates for the development of next-generation POC platforms. Advantages of mobile devices include advanced multicore processing capability, sophisticated user interfaces, and powerful imaging capabilities.[6,7]

At the same time, the progress in the field of nanoplasmonics propelled by the development of metallic nanostructures that support surface plasmon resonance (SPR), has led the development of (bio)sensing technologies. Metallic nanostructures, such as nanohole arrays in metallic films, offer several advantages to (bio)sensing applications requiring portable detection, due to their inherit compact footprint, compatibility with collinear optics, and easiness of integration with other microtechnologies, such as microfluidics.

Although smartphones are not configured for chemical sensing or biosensing, the rapid development of this field of research has demonstrated the use of this devices in sensing platforms such as microscopic imaging, immunodiagnostic assays, colorimetric detection and SPR-based biosensing. Of these optical-based technologies, SPR-based biosensing employs surface plasmons (SPs) for label-free, high sensitivity and real-time detection of binding events.[8,9] SPs are evanescent electromagnetic waves (charge-density oscillations) propagating along the interface of a metal and a dielectric. This metal/dielectric boundary confinement makes SPR extremely sensitive to near-surface refractive index (RI) changes. This property is utilised by metallic nanostructures such as surface relief gratings, nanohole arrays for sensing by tailoring their fabrication parameters.[10] Nanohole arrays in metallic films, specifically, take advantage of plasmonic modes excited on these nanostructure due to the matching between the momentum of the incident light photon and the momentum of plasmon wave at the metal/dielectric interface, promoting the light transmitted through the nanoholes. This phenomenon, called extraordinary optical transmission (EOT), is perfectly suited for imaging sensing techniques such as surface plasmon resonance imaging (SPRi).[8,11,12]

In this work, we present an inexpensive and compact sensing platform built with analogue smartphone-like components: a LED, and a CMOS camera and processing unit, which serves as a step towards smartphone-based point-of-care diagnosis platform. Recent research in the field of sensing via flow-through metallic nanohole arrays have demonstrated high sensing capabilities with a potential for miniaturization.[13,14] In this context, we present a fully-integrated sensing platform employing flow-through nanohole arrays as sensing element. The total size of the platform is 5 cm x 3 cm. Finite-difference time-domain (FDTD) simulations and bulk refractive index changes test were carried out to verify both, electric field (e-field) intensity enhancement of the nanostructures and the wavelength shifting due to RI changes in transmission mode. In addition, we demonstrated the ability of the platform to perform real-time monitoring of near-surface biomolecular interaction. The resulting easy-to-build, handheld and cost-effective device has demonstrated great potential similar to SPRi-based sensors reported in previous works.[2,15]

2.2 Results and Discussion

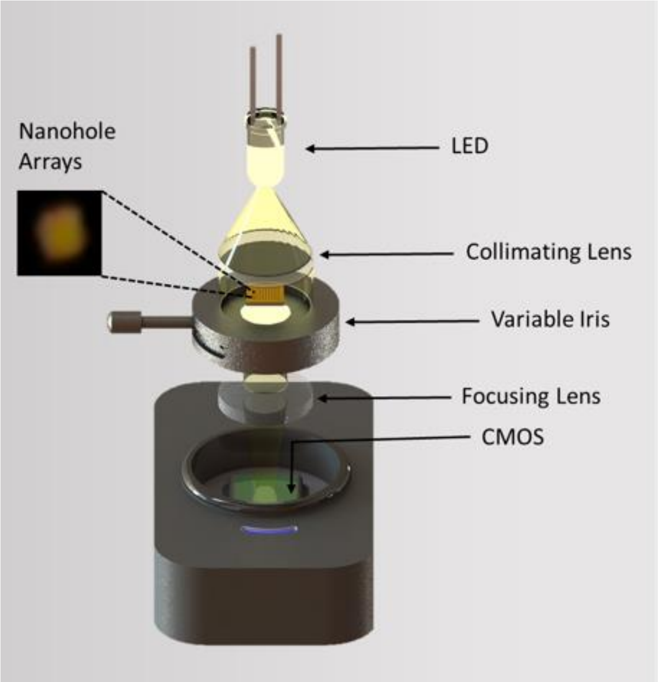

Figure 2.1 Schematic of the SPR imaging experimental setup, displaying the experimental configuration for measuring light transmission through nine arrays of sub-wavelength holes. Magnified image shows the visualised image of nanohole arrays using white LED.

Figure 2.1 shows a schematic representation of the experimental setup used for the optical characterization of the nanohole arrays. The sensor consists of 3 x 3 nanohole arrays, with an effective sensing surface of 22 µm x 22 µm, nanohole diameter of 260 nm and pitch of 520 nm. A 3.5 V, 20 mA, white LED was used as a light source, held in a vertical position by a custom-made mount. A plano-convex lens (diameter = 7.9 mm, focal length = 8 mm) was placed directly underneath the light source to collimate the light. A custom-made holder was used to orient the nanohole arrays orthogonally to the incident LED light beam and a separate holder was used to position the focusing lens on top of CMOS module for maximum signal capture. All the components were positioned in a linear arrangement atop a vertical optical rail. The white light from the LED was directed through the collimating lens and then onto the metallic nanohole arrays.

At this stage, SPs are generated at particular wavelengths, propagating parallel to the plane. SPs scatter into the apertures and couple to the other side of the metal film, where they are converted back to transmitted light. The result of this effect is enhanced transmission through the nanohole array at certain wavelengths, resulting in increased e-field intensities.[11,16] This enhanced transmission can be studied using the equation (1.38), obtained by equating the wave vector of the incident light to the surface plasmon wave vector. For a square nanohole array with circular nanoholes, the excitation wavelength or the SPR wavelength (λ_{SP}) can be approximated by the following equation:

$$\lambda_{SP\ (i,j)} = \left[\sqrt{\varepsilon_d \varepsilon_m/(\varepsilon_d + \varepsilon_m)}\right]\ .P/\sqrt{(i^2 + j^2)} \qquad (1)$$

where P is the periodicity of the array, the integers (i, j) represent the Bragg resonance orders, and ε_m and ε_d are the real part of the permittivity of the metal and surrounding, respectively. This enhanced transmitted light then passes through a lens, which focusses the light onto the CMOS module. Images are captured and saved from the CMOS via Python script running on a Raspberry Pi unit. The script allows control and optimization of image visualization and acquisition parameters such as brightness, contrast, saturation, and white balance, among others.

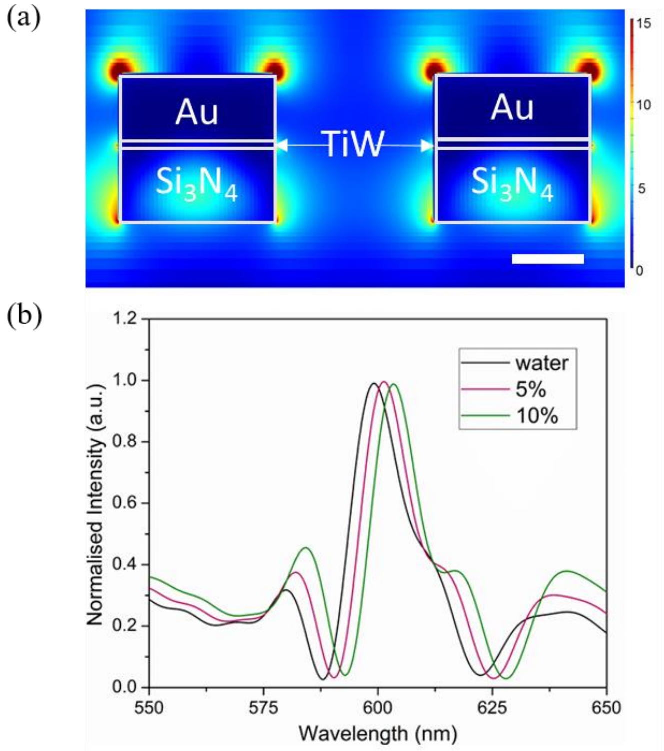

Figure 2.2 FDTD simulation results. (a) Electric ($|E|^2$) field intensity distributions calculated at the transmission peak (λ = 588 nm for air) for the nanohole arrays with periodicity = 520 nm and diameter = 260 nm (Scale bar = 100 nm). (b) Simulated transmission spectra for nanohole arrays when exposed to water and aqueous sucrose solutions of different concentrations (5% and 10%).

As explained in the earlier section, equation (1.38) gives an approximation of the λ_{SP} at which surface plasmon waves are excited on the nanohole arrays surface. The nanohole arrays used in this work have a pitch of 520 nm with hole diameter of 260 nm. Based on these values, the theoretical λ_{SP} at the air/Au interface for the nanohole arrays was calculated to be 576 nm. Simulations were performed using FDTD to study the transmission spectra and e-field distribution for the nanohole arrays. A model replicating the nanohole arrays, consisting of 100 nm silicon nitride as base layer coated with first, 5 nm layer of chromium and second, 100 nm layer of gold was made. This model was then irradiated with a plane wave light source in the wavelength range of 400 – 700 nm. For air/Au interface, the simulations showed a resonance wavelength peak at 583 nm (data not shown), which is close to the calculated theoretical λ_{SP}. Figure 2.2a shows the simulated e-field intensity distribution, at resonance peak wavelength of 583 nm. The e-field intensity mentioned here considers the summation of e-field components in the *x*, *y* and *z* directions along the nanostructure. It is evident from the simulation that the e-field distribution is confined at the edges of individual nanohole. Additionally, transmission spectra were acquired for different dielectric/Au interfaces as shown in figure 2.2b. Bulk refractive index (RI) changes were conducted using aqueous solutions of sucrose (0%, 5%, 10% w/v) having refractive index value of 1.33, 1.337 and 1.344 respectively. Red shift is observed as the refractive index of the solution is increased.

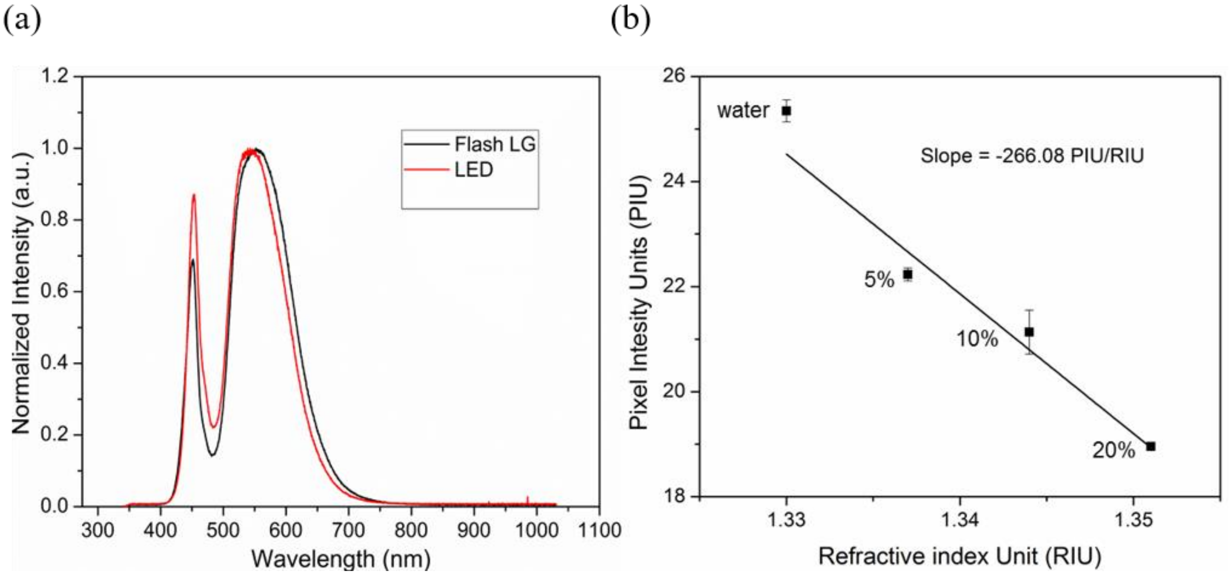

Figure 2.3 (a) Normalised spectra for smartphone (LG G3 STYLUS) flash LED and the white LED used in this work. (b) Line of best fit for a series of mean pixel intensities and bulk refractive index points, where the error bars represent the standard deviations for sample measurements. A linear fit of the pixel intensity units (PIU) vs. refractive index unit (RIU) of each solution characterizes the sensitivity of the sensor (266.08 PIU/RIU).

For this experiment, as explained earlier, a white LED was used as a light source. As the system is intended to be a smartphone-based platform, we performed spectral comparison between the smartphone flash LED and the white LED used in our work. From Figure 2.3a, it is evident that the spectra for both LEDs is very similar, if not identical. Thus, the plasmonic signal generated by the white LED should be analogous, for sensing purposes, to the signal obtained when using the smartphone flash LED. The developed platform was first tested for the detection of changes in bulk RIs. The nanohole arrays were mounted on a custom-made 3D printed holder. The holder consisted of a conical hole in which the sample sits, providing a ~10 µl of head volume which can be used to exposing the nanoholes to solutions with different RIUs. The test solutions used in these experiments were deionized water, and aqueous sucrose solutions of 5%, 10%, and 20% in concentration (w/v) with respective RIs of 1.330, 1.337, 1.344, and 1.357. A volume of 10 µl of the solutions were dispersed on the samples and covered with glass coverslip to avoid possible lensing effect form the free surface of the liquid or evaporation. Light from the white LED was incident orthogonally on the sample and the transmitted images were acquired for each test solution using the experimental setup described previously. The acquired images were processed via ImageJ and an intensity-based study was performed to determine the sensitivity of the system. The sensitivity of the nanohole arrays system, obtained from linear fit shown in Figure 2.3b, is 266.08 PIU/RIU, which is comparable to previously reported SPRi platform.[2,15] Of note is that the platform presented here utilizes components that cost a minimal fraction compared to those used in previous demonstrations. The resolution of the system was estimated to be in the order of 10^{-6} RIU, based on system repeatability of 10^{-3} nm, and the calculated sensitivity.[17] Since resolution takes into account the system noise, this value is typically used as a measure of efficacy of the optical sensing platform.

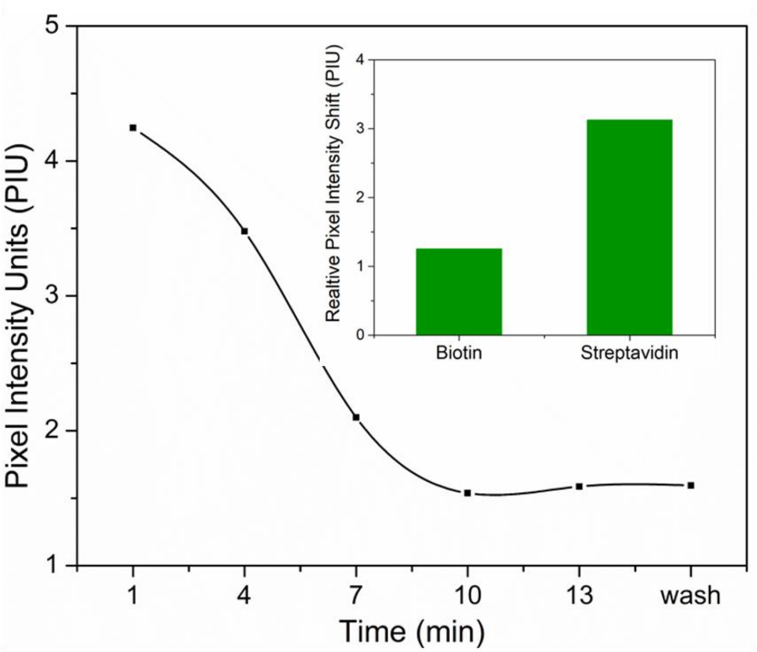

Figure 2.4 Time dependent streptavidin detection assay. (a) Observed real-time PIU shift versus streptavidin incubation time at 830 nM concentration. (b) Total shift in PIU observed after the addition of biotin and streptavidin to the cysteamine-SAM system, taking observed PIU after cysteamine-SAM formation as baseline.

To determine the ability of the platform to detect surface modification, we investigated the utility of nanohole arrays as biosensing platform for the detection of near-surface bio-molecular interactions. A receptor-analyte system of biotin-streptavidin was used for proof-of-concept biosensing test as the binding kinetics of the complex is well established and studied abundantly in the literature. Additionally, this bio-molecular system is suitable for characterizing biosensing testing as it has low dissociation constant, in the order of 10^{-14} M, and the time required to reach a quasi-steady binding state can be estimated based on first-order Langmuir kinetics[2,18]. For the biosensing experiment, the nanohole arrays sensor was washed with 10% acetone and ultrapure water and plasma-cleaned for 15 minutes prior to the experiments. A cysteamine self-assembled monolayer (SAM) was then built on the surface of the sensor by incubating the sensor in 18 mM cysteamine solution (Sigma-Aldrich, Canada) overnight at room temperature. Cysteamine (SAM) acts as an anchoring molecule for biotin-streptavidin complex. The surface-modified sensor was washed with 10% ethanol and phosphate buffer saline (PBS) after incubation to remove any unbound cysteamine remnants. 10 µl of PBS was added to the sensor surface and transmitted light intensity was recorded. The intensity of the transmitted image was used as baseline for measuring the pixel intensity shifts in the subsequent binding experiments. An amine-terminated biotin residue solution (NHS-biotin, Sigma-Aldrich, Canada) with a concentration of 24.56 mM in PBS was then poured on top of the sensor and incubated for 15 minutes. The sample was then washed with PBS and the resulting transmitted image was recorded to verify the PIU shift due to biotin adsorption. The biotin-modified sensor was then incubated in a streptavidin PBS solution (Sigma-Aldrich, Canada) at 0.83 µM in concentration for 14 minutes. The transmission images from the sensors were collected in real time, every 3 minutes, during this incubation stage. Figure 2.4a shows the measured PIU shift as a result from streptavidin binding to biotin on the surface of the nanohole arrays during incubation. The nearly linear PIU-shift increase between times t = 1 min. and t = 10 min. correspond to the streptavidin binding to the surface, dominated by the on-kinetics. After t=14 mins, sensor was washed with PBS and resulting transmitted image was acquired. The total PIU shift at the end of the biotin-streptavidin binding process was 3.13 PIU, using transmitted image acquired after surface modification with cysteamine as baseline intensity image. The PIU shifts observed in this experiment are consistent with previously reported studies in literature.[2,19–21] Most importantly, these results validate the utility of the cost-effective, fully-integrated nanohole array based biosensing platform.

2.3 Conclusion

In this work, we have presented an integrated, compact nanohole arrays-based SPRi sensing platform. The platform is a transmission-based optical assembly comprised of elements found in a standard smartphone, making it feasible for smartphone integration. The platform consists of white LED as light source, having similar spectrum as compared to standard smartphone flash LED, coupled with optical lens array for collimation and focusing of the light as it travels through the sensors. A CMOS module at the base of the assembly is used to acquire transmitted images through the sensors, which is employed for sensing any surface modification on the sensor. Theoretical calculation for SPR spectral response was verified via FDTD simulation. Spectral response of the sensors for different dielectric/Au media and e-field intensity distribution was studied and reported. We presented the ability of our platform to detect and quantify bulk refractive index changes with a sensitivity of 266.08 PIU/RIU (LOD ~ 10^{-6}), which is comparable to existing nanoplasmonic sensing assemblies. We also verified the platform's ability to detect and track real-time changes in local refractive index with a surface modification study using streptavidin-biotin assay and we were successfully able to detect 0.83 µM of streptavidin. In the future, we plan to develop a "true" smartphone based sensing assembly, incorporating only the smartphone components in union with the nanohole arrays, making it self-sufficient in terms of light source, data acquisition and processing (i.e., sensing).

2.4 References

(1) Tokel, O.; Inci, F.; Demirci, U. Advances in Plasmonic Technologies for Point of Care Applications. Chem. Rev. 2014, 114 (11), 5728–5752. https://doi.org/10.1021/cr4000623.

(2) Escobedo, C.; Vincent, S.; Choudhury, A. I. K.; Campbell, J.; Brolo, A. G.; Sinton, D.; Gordon, R. Integrated Nanohole Array Surface Plasmon Resonance Sensing Device Using a Dual-Wavelength Source. J. Micromechanics Microengineering 2011, 21 (11), 115001. https://doi.org/10.1088/0960-1317/21/11/115001.

(3) Foudeh, A. M.; Fatanat Didar, T.; Veres, T.; Tabrizian, M. Microfluidic Designs and Techniques Using Lab-on-a-Chip Devices for Pathogen Detection for Point-of-Care Diagnostics. Lab Chip 2012, 12 (18), 3249–3266. https://doi.org/10.1039/C2LC40630F.

(4) Liu, Y.; Liu, Q.; Chen, S.; Cheng, F.; Wang, H.; Peng, W. Surface Plasmon Resonance Biosensor Based on Smart Phone Platforms. Sci. Rep. 2015, 5 (1), 12864. https://doi.org/10.1038/srep12864.

(5) Gartner. Gartner Says Worldwide Sales of Smartphones Grew 7 Percent in the Fourth Quarter of 2016.

(6) Vashist, S. K.; Mudanyali, O.; Schneider, Em.; Zengerle, R.; Ozcan, A. Cellphone-Based Devices for Bioanalytical Sciences. Analytical and bioanalytical chemistry. May 2014, pp 3263–3277. https://doi.org/10.1007/s00216-013-7473-1.

(7) Preechaburana, P.; Suska, A.; Filippini, D. Biosensing with Cell Phones. Trends Biotechnol. 2014, 32 (7), 351–355. https://doi.org/10.1016/j.tibtech.2014.03.007.

(8) Cetin, A. E.; Coskun, A. F.; Galarreta, B. C.; Huang, M.; Herman, D.; Ozcan, A.; Altug, H. Handheld High-Throughput Plasmonic Biosensor Using Computational on-Chip Imaging. Light Sci. Appl. 2014, 3 (1), e122. https://doi.org/10.1038/lsa.2014.3.

(9) Guner, H.; Ozgur, E.; Kokturk, G.; Celik, M.; Esen, E.; Topal, A. E.; Ayas, S.; Uludag, Y.; Elbuken, C.; Dana, A. A Smartphone Based Surface Plasmon Resonance Imaging (SPRi) Platform for on-Site Biodetection. Sensors Actuators, B Chem. 2017, 239, 571–577. https://doi.org/10.1016/j.snb.2016.08.061.

(10) Homola, J.; Yee, S. S.; Gauglitz, G. Surface Plasmon Resonance Sensors: Review. Sensors Actuators B Chem. 1999, 54 (1–2), 3–15. https://doi.org/10.1016/S0925-4005(98)00321-9.

(11) Ebbesen, T. W.; Lezec, H. J.; Ghaemi, H. F.; Thio, T.; Wolff, P. A. Extraordinary Optical Transmission through Sub-Wavelength Hole Arrays. Nature 1998, 391 (6668), 667–669.

(12) Escobedo, C. On-Chip Nanohole Array Based Sensing: A Review. Lab on a Chip. Royal Society of Chemistry July 7, 2013, pp 2445–2463. https://doi.org/10.1039/c3lc50107h.

(13) Escobedo, C.; Brolo, A. G.; Gordon, R.; Sinton, D. Flow-Through vs Flow-Over: Analysis of Transport and Binding in Nanohole Array Plasmonic Biosensors. Anal. Chem. 2010, 82 (24), 10015–10020. https://doi.org/10.1021/ac101654f.

(14) Eftekhari, F.; Escobedo, C.; Ferreira, J.; Duan, X.; Girotto, E. M.; Brolo, A. G.; Gordon, R.; Sinton, D. Nanoholes As Nanochannels: Flow-through Plasmonic Sensing. Anal. Chem. 2009, 81 (11), 4308–4311. https://doi.org/10.1021/ac900221y.

(15) Escobedo, C.; Chou, Y.-W.; Rahman, M.; Duan, X.; Gordon, R.; Sinton, D.; Brolo, A. G.; Ferreira, J. Quantification of Ovarian Cancer Markers with Integrated Microfluidic Concentration Gradient and Imaging Nanohole Surface Plasmon Resonance. Analyst 2013, 138 (5), 1450. https://doi.org/10.1039/c3an36616b.

(16) Barnes, W. L.; Dereux, A.; Ebbesen, T. W. Surface Plasmon Subwavelength Optics. Nature 2003, 424 (6950), 824–830. https://doi.org/10.1038/nature01937.

(17) Hwang, G. M.; Pang, L.; Mullen, E. H.; Fainman, Y. Plasmonic Sensing of Biological Analytes Through Nanoholes. IEEE Sens. J. 2008, 8 (12), 2074–2079. https://doi.org/10.1109/JSEN.2008.2007663.

(18) Squires, T. M.; Messinger, R. J.; Manalis, S. R. Making It Stick: Convection, Reaction and Diffusion in Surface-Based Biosensors. Nat. Biotechnol. 2008, 26 (4), 417–426. https://doi.org/10.1038/nbt1388.

(19) Lindquist, N. C.; Lesuffleur, A.; Im, H.; Oh, S.-H.; Ebbesen, T. W.; Girard, C.; Gonzalez, M. U.; Baudrion, A. L. Sub-Micron Resolution Surface Plasmon Resonance Imaging Enabled by Nanohole Arrays with Surrounding Bragg Mirrors for Enhanced Sensitivity and Isolation. Lab Chip 2009, 9 (3), 382–387. https://doi.org/10.1039/B816735D.

(20) Im, H.; Lesuffleur, A.; Lindquist, N. C.; Oh, S.-H. Plasmonic Nanoholes in a Multichannel Microarray Format for Parallel Kinetic Assays and Differential Sensing. Anal. Chem. 2009, 81 (8), 2854–2859. https://doi.org/10.1021/ac802276x.

(21) Nair, S.; Escobedo, C.; Sabat, R. G. Crossed Surface Relief Gratings as Nanoplasmonic Biosensors. ACS Sensors 2017, 2 (3), 379–385. https://doi.org/10.1021/acssensors.6b00696.

Chapter 3

Cost-effective flow-through nanohole array-based biosensing platform for the label-free detection of uropathogenic E. coli in real time

With minor changes to fulfill formatting requirements, this chapter is as it appears in:

Juan Gomez-Cruz, Srijit Nair, Angel Manjarrez-Hernandez, Sandra Gavilanes Parra, Gabriel Ascanio and Carlos Escobedo. Biosensors and Bioelectronics, 2018, 106, 105-110.

Abstract: Rapid, inexpensive and sensitive detection of uropathogenic *Escherichia coli* (UPEC), a common cause of ascending urinary tract infections (UTIs) including cystitis and pyelonephritis, is critical given the increasing number of cases and its recurrence worldwide. In this paper, we present a label-free nanoplasmonic sensing platform, built with off-the-shelf optical and electronic components, which can detect intact UPEC at concentrations lower than the physiological limit for UTI diagnosis, in real time. The sensing platform consists of a red LED light source, lens assembly, CMOS detector, Raspberry Pi interface in conjugation with a metallic flow-through nanohole array-based sensor. Detection is achieved exploiting nanoplasmonic phenomena from the nanohole arrays through surface plasmon resonance imaging (SPRi) technique. The platform has a bulk sensitivity of 212 pixel intensity unit (PIU)/refractive index unit (RIU), and a resolution in the order of 10^{-6} RIU. We demonstrate capture and detection of UPEC with a detection limit of ~100 CFU/ml – a concentration well below the threshold limit for UTI diagnosis in clinical samples. We also demonstrate detection of UPEC in spiked human urine samples, for two different concentration of bacteria. This work is particularly relevant for point-of-care applications, especially for regions around the world where accessibility to medical facilities is heavily dependent upon economy, and availability.

3.1 Introduction

Urinary tract infections (UTIs) are among the most prevailing infectious diseases on a global scale. Every year, an estimated of 150 million people are affected by UTIs worldwide, and the majority of those infections (~ 80%) are caused by uropathogenic *Escherichia coli* (UPEC).[1–3] UPEC invade the urothelial cell lining and live within the urinary tract by evading the host's immune response. Conventionally, detection of UPEC is achieved by biochemical and serological methods, culturing bacteria in selective media. Although these techniques are well-established, highly selective and reliable for detecting and measuring the level of UPEC bacterial infections, the timeline for detection requires 3 to 7 days to complete.[4] With recent advances in polymerase chain reaction (PCR) and immunology-based enzyme-linked immunosorbent assays (ELISA), the detection timeline has come down to several hours.[4] However, these procedures require tedious pre-treatment methods such as cell lysis, nucleic acid extraction, and signal amplification accompanied by specialized lab technicians, which inherently increase costs, limiting their widespread applicability. These limitations are particularly important from a world-wide perspective, since 56% of the global rural population has no access to essential medical facilities and, therefore, to effective disease diagnosis.[5] In recent years, researchers have explored several fields to develop new biosensing technologies that enable point-of-care (POC) testing for infectious diseases on-site.[6–8] In this sense, nanoplasmonic biosensors provide a unique prospect to develop fully-integrated, portable POC biosensing devices enabling real-time and cost-effective detection of target analytes.[9–14]

Ordered arrays of metallic sub-wavelength apertures, such as nanoholes, exhibit extraordinary optical transmission (EOT) as a result of surface plasmons (SPs).[15] At resonant wavelengths, nanohole arrays couple the incident light to SPs, resulting in charge density oscillations at the metal-dielectric interface.[16–18] These electromagnetic standing waves, known as surface plasmon resonance (SPR), are highly sensitive to changes in the refractive index (RI) at the metal-dielectric interface, which can be utilized to detect and study near-surface events in label-free fashion.[19–21] Compared to other optical arrangements that support SPR, such as Kretschmann configuration, nanohole arrays support SPs at normal light incidence, which enables sensing using straightforward collinear optics. This convenient optical arrangement, in addition to the small footprint and sensitivity of nanohole arrays, has facilitated their application in biomedical diagnostics for the detection of cancer biomarkers,[18] bacteria,[22] and viruses.[23] Additionally, nanohole arrays also enable monitoring of near-surface adsorption events (i.e. analyte detection) via SPR imaging (SPRi) by quantifying the intensity variation from transmitted monochromatic beams.[24–26] Most SPRi-based sensing demonstrations dedicated to real-world applications up till now, including the detection of infectious diseases, have employed bulky and costly setups involving microscope-based assemblies and CCD modules,[22,27,28] averting their use as effective POC sensing platforms. In addition, demonstrations of nanohole array based sensing, in the context of POC UPEC detection, are virtually inexistent.

In this work, we present a SPRi-based sensing platform with a cost-effective, POC-compatible arrangement with off-the-shelf components that enables detection of UPEC. We demonstrate a fully integrated label-free sensing platform based on flow-through nanohole arrays with a footprint of 22 μm × 22 μm as sensing element. The total platform envelope, containing all optical elements and light source is 45 cm^3 (3 cm × 3 cm × 5 cm). The platform comprises an optical array made from inexpensive commercial components, and an economical CMOS sensor. The response of the platform is tested via FDTD simulations and SPRi tests for the detection of bulk RI changes. The platform is ultimately tested for the label-free SPRi-based detection of UPEC in real time, demonstrating its potential for real-world POC-compatible diagnosis applications.

3.2 Experimental section

3.2.1 Overview of the integrated sensing platform

Figure 3.1 shows a schematic representation of the biosensing SPRi platform for UPEC detection. The platform assembly contained all the optical components such as LED, lenses and sensing nanostructure in a customized holder with a total volume of 45 cm^3 (3 cm × 3 cm × 5 cm).

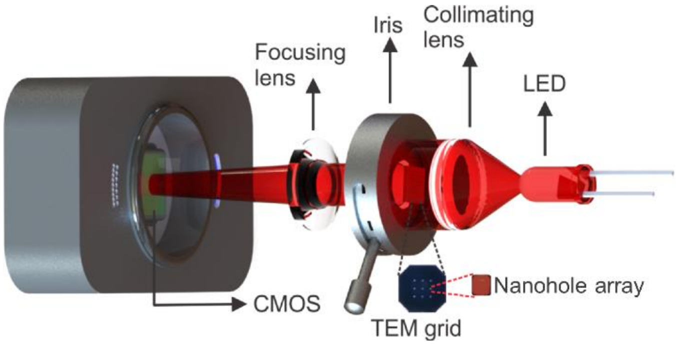

Figure 3.1 Schematic representation (not to scale) of the biosensing SPRi platform, consisting of a CMOS detector, light source (LED, peak wavelength = 626 nm), flow-through nanohole array sensor and off-the-shelf optical elements. The optics, light source and nanohole array are contained in a customized holder of 45 cm3. The magnified images of an actual 9-window TEM grid and transmitted light through a nanohole array are shown.

The nanohole arraystructure was attached to a custom-made nanometric positioning stage, which allowed an accurate mapping of the sample surface. The light source comprised of a red LED (forward voltage = 2 V, forward current = 20 mA), with a peak intensity at a wavelength ~ 626 nm. A plano-convex lens (diameter = 7.9 mm, focal length = 8 mm) was placed after the LED to collimate the light incident on the sensing element. The sensing element consisted of a TEM grid (Norcada, Edmonton, AB, Canada) containing an array of 3 x 3 free-standing gold-on-nitride window membranes of 500 µm x 500 µm in surface (Figure 3.1). Each window membrane contained one array of through nanoholes, with an effective sensing area of 22 µm x 22 µm, nanohole diameter of 280 nm, and uniform pitch of 560 nm. The nanohole array sensor was placed in the customized holder in normal position with respect to the plane of incidence of the light from the LED. A bi-convex lens (diameter = 12.7 mm, focal length = 50 mm) was placed between the sensor and the CMOS detector, in order to acquire the transmitted light from each nanohole array.

Materials and fabrication costs are crucial factors for the market viability and successful implementation of a sensor for POC diagnosis. For the platform presented here, the cost of the gold-on-nitride TEM grids are around US$7 per unit, and the cost associated with the fabrication of the nanoholes via focused ion beam (FIB) lithography (more details in Section 3.2.2) is about US$140 (at US$70 per hour, including clean room fees). However, the fabrication of the nanohole arrays can be dramatically reduced by using more modern nanofabrication methods, such as template-stripping,[29] instead of FIB milling. The cost for the rest of the components in the integrated platform comes to ~ US$95, including the two lenses (Edmund Optics Inc., NJ, USA), a Raspberry Pi 3 board and CMOS detector (Raspberry Pi Foundation, UK), and the red LED. In comparison, a traditional SPRi setting involves a He-Ne laser that can cost, for instance, between US$1,500 (R-30991 HeNe, 633 nm, 5 mW laser, Newport Corp., USA) and US$7,500 (R-14309 HeNe, 633 nm, 35 mW laser, Newport Corp., USA), and a CCD camera with costing around US$6,000 (based on a 1.4 Megapixel monochrome CCD Camera, standard Package, Thorlabs, Inc., USA), or even more if microscopy is involved. The platform presented here reduces, drastically, the cost of SPRi sensing by two or three orders of magnitude.

3.2.2 Fabrication of flow-through nanohole arrays

The through nanohole arrays were fabricated by focused ion beam (FIB) milling using 100 nm thick Si_3N_4 free-standing membranes (Norcada, Edmonton, AB, Canada) coated with a thermally evaporated 100 nm layer of gold via a 5 nm Ti/W adhesion layer. For milling, the gallium ion beam was set to 40 keV with a beam current of 30 pA, the typical beam spot size was 10 nm, and the dwell time of the beam at one pixel was set to 10 μs.

3.2.3 Custom-made nanometric positioning system

A custom-made 2-axis nanometric positioning system was built to support and to position the sensing assembly along the focal plane. This system allowed the precise and controlled motion of the sensor on a plane perpendicular to the incident light direction, and illumination of a single, preselected nanohole array. The nanometric positioning system consisted of two orthogonal stages (x and y-axes), that were each actuated by a stepper motor (NEMA 17, Pololu robotics and electronics, NV, USA). The connection between the micrometre head of the stage and the shaft of the motor was achieved using a homemade 3D printed clamp-type flexible coupler, which dampened the effects of misalignment at this connection junction. The stepper motors had a minimum step angle of 1.8° (200 steps/revolution), which corresponds to a translational resolution of ~ 3 µm. Since this resolution is insufficient for addressing each nanohole array independently, a microstep-resolution motor driver (DRV8825, Pololu robotics and electronics, NV, USA) was connected to the stepper motors, in order to reduce the step size by 1/32. The system was controlled via an Arduino nanoboard that was connected to the nanometric positioning system.

3.2.4 Bacterial culture

Bacteria *E. coli* O6:H1 (strain CFT073 / ATCC 700928 / UPEC) were routinely grown at 37°C in Luria-Bertani (LB) medium. Overnight culture resulted in bacterial concentration of 10^9 colony-forming units (CFU)/ml. The bacteria sample was then suspended and diluted in PBS (pH 7.4) to obtain 10^9,10^8, 10^6, 10^5, and 10^3 CFU/ml in concentration, for UPEC detection experiments.

3.2.5 Production of antibodies

Polyclonal rabbit antiserum to *E. coli* was prepared by immunization with cell envelopes. Strain CFT073 was grown overnight at 37°C in M9 defined culture medium (42 mM Na_2HPO_4, 22 mM KH_2PO_4, 9 mM NaCl, 18 mM NH_4Cl, 1 mM $MgSO_4$, 0.1 mM $CaCl_2$ and 0.2% (w/v) glucose),[30] supplemented with 0.5 g/L of Peptone. The bacterial pellet was resuspended in 50 mM Tris-HCl, 5 mM EDTA (pH 7.5) containing protease inhibitor cocktail (Roche, Switzerland) and disrupted by ultrasonication with two 40 s pulses at low power output, each followed by a 2-min pause, using a high-intensity ultrasonic processor (50-Watt Model, Sonics Materials Inc. Danbury, CT), unbroken cells were removed by centrifugation (12,000 x g for 10 min, 4°C). Cell envelopes were collected by ultracentrifugation (50,000 x g for 30 min, 4°C) and dissolved in PBS (pH 7.4). The envelope solution was injected subcutaneously (in multiple sites, 0.5 mg without any adjuvant) into rabbits. The animals were boosted 3 and 6 weeks later with the same membrane solution. Blood was collected from the central auricular vein of each ear 15 days later.

3.2.6 Human urine preparation

Human urine was collected from healthy individuals who had no history of UTI. The fresh urine was pooled and filtered with a 0.22-μm-pore-size, stored at 4°C and used within the next 1 to 3 days.

3.3 Results and discussion

3.3.1 Nanohole arrays

A total of 9 (3 x 3) nanohole arrays, each having a footprint of 22 μm × 22 μm, were fabricated via FIB lithography. Figure 3.2a shows an actual image of a fabricated flow-through nanohole array. The EOT associated with nanohole arrays on metallic films is attributed to SPs, oscillations of free metal electrons upon interaction and trapping of incident electromagnetic waves at the metal surface. EOT depends on the fabrication parameters, namely: hole diameter, *d*, and pitch, *p*, and the propagation media characteristics such as dielectric constants of the metallic film, ε_m, and the surrounding medium, ε_d. For a square array of circular nanoholes, the SPR transmission peak position (λ_{SP}) at normal incidence can be approximated by the following equation:

$$\lambda_{SP\,(i,j)} = \left[\sqrt{\varepsilon_d \varepsilon_m/(\varepsilon_d + \varepsilon_m)}\right] .\, p \,/ \sqrt{(i^2 + j^2)} \tag{1}$$

where i and j represent the resonance grating order.[9,31–33] The nanohole arrays fabricated for this study had a periodicity of 560 nm and a nanohole diameter of 280 nm, and an expected SPR peak at ~ 680 nm in the transmitted spectrum. Figure 3.2b shows the raw data transmission spectrum from a single nanohole array, acquired by a linear optical arrangement consisting of a halogen lamp, collimating lenses and a UV-Visible USB spectrometer (USB 2000+, Ocean Optics Inc., USA).

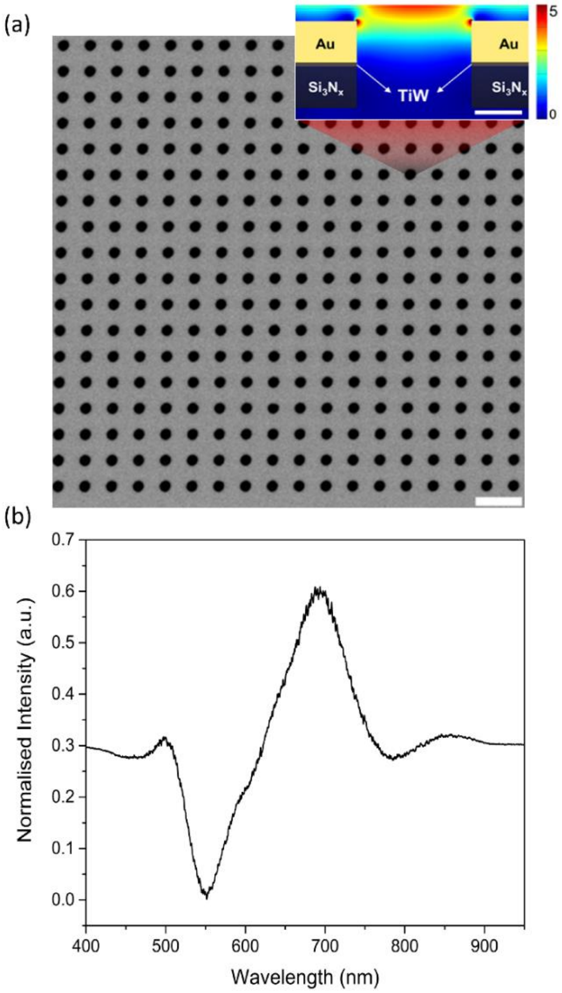

Figure 3.2 (a) SEM image of the fabricated nanohole arrays with a periodicity of 560 nm and diameter of 280 nm. Scale bar indicates 1 µm. The inset shows the electric field intensity distribution obtained from FDTD simulations,

using light source peak wavelength at λ = 626 nm. Scale bar indicates 100 nm. (b) White light transmission spectrum (raw data) from the nanohole arrays.

The acquired spectrum, which was normalized to isolate the contribution from the SPs, shows the resonance peak at 690 nm, in agreement with the predicted value from equation (1.36). Variation in the transmitted light intensity at a fixed wavelength was employed to achieve sensing via SPRi. The LED used in the platform was selected to have a peak intensity at a wavelength between 600 and 650 nm, which is a quasi-linear region in the transmission spectrum of the nanohole arrays when using a halogen lamp. From equation (1.36), it can be observed that an increase in RI due to, for instance, binding events at the surface of the nanohole arrays, will result in a red spectral shift that will be reflected as a decrease in the transmitted light intensity. In addition to the transmitted spectrum, a mapping of the electric field (e-field) intensity distribution was simulated using 3D finite-difference time-domain (FDTD) method, in order to confirm the electric field enhancement due to SPR, considering the fabrication parameters. For the simulation, periodic and anti-periodic boundary conditions were defined in the *x*- and *y*- axes, and a perfect match layer boundary along the *z*-axis. The e-field response was recorded at λ = 626 nm, which corresponds to the peak intensity wavelength of the red LED employed for this work. The inset in Figure 3.2a shows the confined e-field enhancement in the vicinity of the nanoholes at the metal-dielectric interface from the FDTD simulations.

Table 3.1 Calibration of the custom-made nanometric positioning stage (N=3).

S. No.	Number of steps	Traveled distance (μm) ±5 μm	Step size (nm)
1	400	30	75
2	600	50	83.3
3	800	60	75
4	1000	80	80

5	2000	160	80
6	4000	310	77.5
7	6000	470	78.3
8	8000	630	78.8
9	10000	780	78
10	12000	940	78.3
Average step size			78.4
Standard deviation			±2.4

3.3.2 Characterization of the custom-made nanometric positioning stage

The computer user interface that controls the nanometric stages was developed in C# language. The interface allowed automated mapping of the sensing element by controlling the rotational direction of each motor, the total travel distance, number of stops and the waiting time at each stop before reaching the final travel distance. The resolution of the system was calculated using a stage (MS1S/M, Thorlabs, Inc., NJ, USA) which bears a micrometre screw gauge (148-205, Mitutoyo, Japan) with an accuracy of ± 5 µm. Several tests relating a number of steps *vs.* travelled distance were carried out (Table 3.1), yielding an average resolution of 78 ± 2 nm.

3.3.3 Sensing test

The performance of the integrated platform was first evaluated for the detection of bulk RI changes, using the setup described in Section 3.2.1 (also see Figure 3.1). The spectral shift resulting from the bulk RI changes was monitored through SPRi, using the transmitted light images acquired with the CMOS. The customized holder allowed positioning the nanohole arrays sensing element, and provided a headspace sufficient to house ~ 10 µl of liquid on top, so solutions with different RI could be tested. The test solutions used in these experiments consisted of deionized water, and 10%, 15% and 20% (w/v) aqueous sucrose solutions, with respective RIs of 1.330, 1.344, 1.351and 1.357. The transmitted images for each solution were acquired, and processed using ImageJ software. Figure 3.3 shows the mean intensity values of the acquired images for each solution. The negative slope of the linear fit of the transmitted light intensity as a function of RIs confirmed the anticipated red spectral shift of the nanoplasmonic resonance peak. The sensitivity of the platform, obtained from linear fit, is 212 PIU/RIU, which is comparable to the sensitivity of SPRi platforms reported in the past.[18,26]

It is worth mentioning that the platform presented here utilizes off-the-shelf and low-cost components, which brings the cost of the platform considerably down as compared to similar systems previously reported. The resolution of the system, which is typically used as a measure of efficacy as it takes into account the system noise, is in the order of 10^{-6} RIU, based on system repeatability of 10^{-3} nm and the calculated sensitivity.[34]

3.3.4 Detection of uropathogenic E. coli

The main objective of the presented platform is to be deployed in situ, in order to enable POC testing. UTI detection, specifically, requires real-time detection of bacteria directly from bodily fluid. For this reason, the biological tests were focused on the detection of whole bacteria rather than genome sequence-based methods, which are accurate, but also time-consuming. The surface of the flow-through nanohole array sensor was functionalized with UPEC-specific antibodies to achieve whole-bacterium detection, as the antibodies may bind to the membrane of the bacteria by anchoring to proteins, phospholipids, and oligosaccharides on the cell’s surface, as reported earlier in the literature.[35] Figure 3.4a shows the intensity change of transmitted light over time for both the surface modification with antibodies ($t = 0$ to $t = 15$ minutes), and for the detection of UPEC ($t > 15$ minutes).

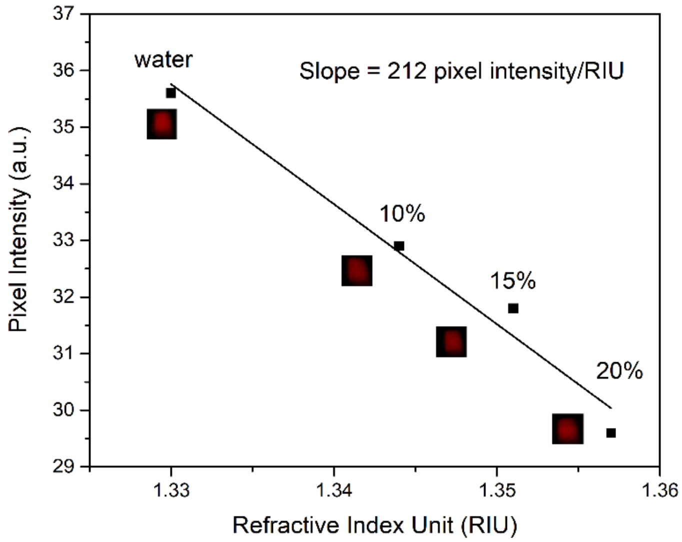

Figure 3.3 Bulk sensitivity test. Average pixel intensity (a.u.) values of the transmitted light from the nanohole arrays as a function of RI for water and sucrose solutions (10%, 15% and 20% in concentration). Actual images of the light intensity, corresponding to each RI, are shown as insets. The line of best fit yields a slope (i.e. sensitivity) of 212 pixel intensity/RIU. Standard deviations (N = 3) are smaller than the symbols representing data points.

For this experiment, the transmitted light intensity having PBS solution on the sensor was assumed as baseline (*t* = 0 minutes). The UPEC-specific antibodies were incubated for 15 minutes on the metallic surface of the nanohole arrays, and images were acquired at 5-minute intervals. The surface modification, which produces an increase in local RI, resulted in a red shift in the spectrum that was reflected as a decrease in the light transmitted intensity, as shown in Figure 3.4a. After incubation, 10 µl of 10^9 CFU/ml UPEC were added to the surface of the nanohole arrays, and images were acquired for 15 minutes, at 5-minute intervals. Finally, the surface of the nanoholes was rinsed with PBS at the end of the experiment to remove non-captured and floating remnant UPEC. The relative intensity difference corresponding to the addition of antibody and bacteria compared to the PBS baseline intensity was 7.237 and 9.067 a.u., respectively, as shown in the inset in Figure 3.4a. As the sensing efficacy of SPR based sensors is limited by the availability of analyte on the sensing surface, we performed a dose-based binding study to determine the limit of detection (LOD) of the sensing platform. UPEC suspensions in PBS with concentrations of 10^3,

10^5, 10^6, 10^8 and 10^9 CFU/ml were used in this experiment. Figure 3.4b shows the relative intensity difference of the plasmonic signal associated with the UPEC capture on the functionalized surface (i.e. detection). The intensity of the signal varies linearly with the logarithmic concentration of bacteria. Based on this fit, the calculated LOD of the sensing platform was ~ 100 CFU/ml, determined by the concentration corresponding to the only-antibody signal (w/o addition of bacteria) plus 3 times the standard deviation of the acquired signal.[36] Notably, this LOD is well below the physiological concentration range found in reported UTI cases and medical standards.[1,37] Typically, the concentration of UPEC for diagnosing UTI in clinical samples is ~ 10^5 CFU/ml, which is well above the LOD of the platform presented in this work and lays within the range of concentrations that the presented platform can detect (Figure 3.4b). Moreover, the platform enables the detection of UPEC with a sensitivity that is competitive, compared to established technologies currently in practice. For the experiment using human urine, UPEC-specific antibodies were incubated for 15 minutes on a clean nanohole array, and images were acquired at 5-minute intervals, similar to the previously described experiments with PBS solution. Then, 10 µl of urine samples spiked with UPEC were added to the surface of the nanohole arrays, followed by a urine rinse step to remove non-captured UPEC. The concentrations of UPEC in the urine used in this experiment were 10^5 and 10^8 CFU/ml, and images were acquired for 15 minutes, at 5-minute intervals. Figure 3.4b shows the two data points (red stars) corresponding to the relative intensity associated with the detection of the bacteria at the two different concentrations, demonstrating the potential of the biosensing platform to detect UPEC in complex matrices, including bodily fluids.

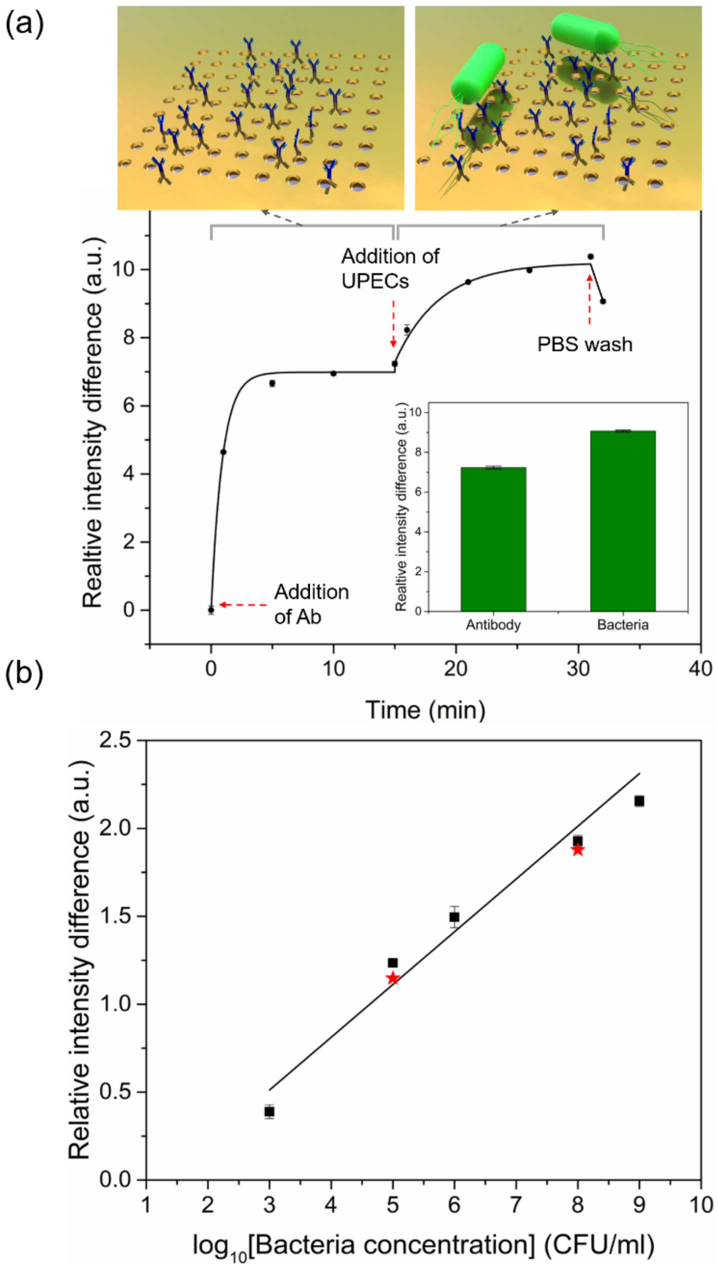

Figure 3.4 Time-dependent uropathogenic *E. coli* detection assay. (a) Real-time relative intensity shift corresponding to detection of bacteria at a concentration of 109 CFU/ml. Three-dimensional renderings (not to scale) illustrate the scheme employed for bacteria detection. The inset shows the cumulative intensity shift observed after addition of anti-UPEC antibody and UPEC. (b) Relative intensity shift corresponding to different concentrations of UPEC in PBS buffer (103, 105, 106, 108, 109 CFU/ml; black squares; R2=0.947) and in human urine (105, 108 CFU/ml; red stars). Error bars indicate the standard deviation observed for each bacterial measurement for N = 3.

3.4 Conclusions

Here we demonstrated a fully integrated, compact, and low-cost SPRi platform that enables the label-free detection of UPEC. The miniaturized sensing assembly has a volume envelope of 3 cm × 3 cm × 5 cm, and consists of a nanohole array based nanoplasmonic sensor, an inexpensive commercial CMOS detector, and off-the-shelf optical components. The sensing platform detects bulk RI changes with a sensitivity of 212 pixel intensity/RIU and has a resolution of 10^{-6} RIU. The platform facilitated the effective detection of UPEC in both PBS and human urine, at concentrations spanning from 10^3 to 10^9 CFU/ml, which demonstrates its potential for real-world POC biosensing applications. The calculated LOD of the platform for the detection of UPEC is ~ 100 CFU/ml, which is well below the threshold limit for UTI diagnosis. Furthermore, the platform allowed detection of UPEC within 35 minutes, taking into consideration the time required to incubate and detect both the antibodies and the bacteria. In addition to the rapid detection process, the overall cost of the platform is exceptionally low compared to established SPRi systems, due to the off-the-shelf optical components, and the inexpensive LED and CMOS involved. Another benefit of the system presented here is that samples require minimal pre-treatment, enabling the detection of intact bacteria, which significantly reduces the time-consuming preprocessing steps, in contrast to traditional DNA extraction and amplification approaches. The sensitivity of the platform, along with the cost and deployment easiness, demonstrates its potential as POC diagnostic device for the *in situ*, label-free detection of UTI using raw samples, such as bodily fluids. Future directions on the platform may include integration of intricate microfluidics as part of the assembly for multiplexed sensing. The results presented here demonstrate that the platform has the potential to advance the telemedicine field, including POC diagnostics, as the optics, light source and detector of the assembly are fully compatible with and can be adapted to smartphones.

3.5 References

(1) Grabe, M.; Bjerklund-Johansen, T. E.; Botto, H.; Cai, T.; Çek, M.; Köves, B.; Naber, K. G.; Pickard, R. S.; Tenke, P.; Wagenlehner, F. Guidelines on Urological Infections. Eur. Assoc. Urol. 2015, 14.

(2) Foxman, B. The Epidemiology of Urinary Tract Infection. Nat. Rev. Urol. 2010, 7 (12), 653–660. https://doi.org/10.1038/nrurol.2010.190.

(3) Stamm, W. E.; Norrby, S. R. Urinary Tract Infections: Disease Panorama and Challenges. J. Infect. Dis. 2001, 183 (s1), S1–S4. https://doi.org/10.1086/318850.

(4) Alocilja, E. C.; Radke, S. M. Market Analysis of Biosensors for Food Safety. Biosens. Bioelectron. 2003, 18 (5–6), 841–846. https://doi.org/10.1016/S0956-5663(03)00009-5.

(5) Scheil-Adlung, X. Global Evidence on Inequities in Rural Health Protection. New Data on Rural Deficits in Health Coverage for 174 Countries; Geneva, 2015.

(6) Wang, Y.; Ye, Z.; Si, C.; Ying, Y. Monitoring of Escherichia Coli O157:H7 in Food Samples Using Lectin Based Surface Plasmon Resonance Biosensor. Food Chem. 2013, 136 (3–4), 1303–1308. https://doi.org/10.1016/j.foodchem.2012.09.069.

(7) Laksanasopin, T.; Guo, T. W.; Nayak, S.; Sridhara, A. A.; Xie, S.; Olowookere, O. O.; Cadinu, P.; Meng, F.; Chee, N. H.; Kim, J.; Chin, C. D.; Munyazesa, E.; Mugwaneza, P.; Rai, A. J.; Mugisha, V.; Castro, A. R.; Steinmiller, D.; Linder, V.; Justman, J. E.; Nsanzimana, S.; Sia, S. K. A Smartphone Dongle for Diagnosis of Infectious Diseases at the Point of Care. Sci. Transl. Med. 2015, 7 (273), 273. https://doi.org/10.1126/scitranslmed.aaa0056.

(8) Chin, C. D.; Laksanasopin, T.; Cheung, Y. K.; Steinmiller, D.; Linder, V.; Parsa, H.; Wang, J.; Moore, H.; Rouse, R.; Umviligihozo, G.; Karita, E.; Mwambarangwe, L.; Braunstein, S. L.; van de Wijgert, J.; Sahabo, R.; Justman, J. E.; El-Sadr, W.; Sia, S. K. Microfluidics-Based Diagnostics of Infectious Diseases in the Developing World. Nat. Med. 2011, 17 (8), 1015–1019. https://doi.org/10.1038/nm.2408.

(9) Homola, J. Surface Plasmon Resonance Sensors for Detection of Chemical and Biological Species. Chem. Rev. 2008, 108 (2), 462–493. https://doi.org/10.1021/cr068107d.

(10) Escobedo, C. On-Chip Nanohole Array Based Sensing: A Review. Lab on a Chip. Royal Society of Chemistry July 7, 2013, pp 2445–2463. https://doi.org/10.1039/c3lc50107h.

(11) Lazcka, O.; Campo, F. J. Del; Muñoz, F. X. Pathogen Detection: A Perspective of Traditional Methods and Biosensors. Biosens. Bioelectron. 2007, 22 (7), 1205–1217. https://doi.org/10.1016/j.bios.2006.06.036.

(12) Barreiros dos Santos, M.; Agusil, J. P.; Prieto-Simón, B.; Sporer, C.; Teixeira, V.; Samitier, J. Highly Sensitive Detection of Pathogen Escherichia Coli O157:H7 by Electrochemical Impedance Spectroscopy. Biosens. Bioelectron. 2013, 45, 174–180. https://doi.org/10.1016/j.bios.2013.01.009.

(13) Preechaburana, P.; Gonzalez, M. C.; Suska, A.; Filippini, D. Surface Plasmon Resonance Chemical Sensing on Cell Phones. Angew. Chemie - Int. Ed. 2012, 51 (46), 11585–11588. https://doi.org/10.1002/anie.201206804.

(14) Nair, S.; Escobedo, C.; Sabat, R. G. Crossed Surface Relief Gratings as Nanoplasmonic Biosensors. ACS Sensors 2017, 2 (3), 379–385. https://doi.org/10.1021/acssensors.6b00696.

(15) Ebbesen, T. W.; Lezec, H. J.; Ghaemi, H. F.; T. Thio; A.Wolff, P.; Thio, T.; A.Wolff, P. Extraordinary Optical Transmission through Sub-Wavelength Hole Arrays. Nature 1998, 86 (6), 1114–1117. https://doi.org/10.1038/35570.

(16) Lindquist, N. C.; Lesuffleur, A.; Im, H.; Oh, S.-H.; Ebbesen, T. W.; Girard, C.; Gonzalez, M. U.; Baudrion, A. L. Sub-Micron Resolution Surface Plasmon Resonance Imaging Enabled by Nanohole Arrays with Surrounding Bragg Mirrors for Enhanced Sensitivity and Isolation. Lab Chip 2009, 9 (3), 382–387. https://doi.org/10.1039/B816735D.

(17) Cetin, A. E.; Etezadi, D.; Galarreta, B. C.; Busson, M. P.; Eksioglu, Y.; Altug, H. Plasmonic Nanohole Arrays on a Robust Hybrid Substrate for Highly Sensitive Label-Free Biosensing. ACS Photonics 2015, 2 (8), 1167–1174. https://doi.org/10.1021/acsphotonics.5b00242.

(18) Escobedo, C.; Chou, Y.-W.; Rahman, M.; Duan, X.; Gordon, R.; Sinton, D.; Brolo, A. G.; Ferreira, J. Quantification of Ovarian Cancer Markers with Integrated Microfluidic Concentration Gradient and Imaging Nanohole Surface Plasmon Resonance. Analyst 2013, 138 (5), 1450. https://doi.org/10.1039/c3an36616b.

(19) Eftekhari, F.; Escobedo, C.; Ferreira, J.; Duan, X.; Girotto, E. M.; Brolo, A. G.; Gordon, R.; Sinton, D. Nanoholes As Nanochannels: Flow-through Plasmonic Sensing. Anal. Chem. 2009, 81 (11), 4308–4311. https://doi.org/10.1021/ac900221y.

(20) Escobedo, C.; Brolo, A. G.; Gordon, R.; Sinton, D. Flow-Through vs Flow-Over: Analysis of Transport and Binding in Nanohole Array Plasmonic Biosensors. Anal. Chem. 2010, 82 (24), 10015–10020. https://doi.org/10.1021/ac101654f.

(21) Escobedo, C.; Brolo, A. G.; Gordon, R.; Sinton, D. Optofluidic Concentration: Plasmonic Nanostructure as Concentrator and Sensor. Nano Lett. 2012, 12 (3), 1592–1596. https://doi.org/10.1021/nl204504s.

(22) Soler, M.; Belushkin, A.; Cavallini, A.; Kebbi-Beghdadi, C.; Greub, G.; Altug, H. Multiplexed Nanoplasmonic Biosensor for One-Step Simultaneous Detection of Chlamydia Trachomatis and Neisseria Gonorrhoeae in Urine. Biosens. Bioelectron. 2017, 94, 560–567. https://doi.org/10.1016/j.bios.2017.03.047.

(23) Yanik, A. A.; Huang, M.; Kamohara, O.; Artar, A.; Geisbert, T. W.; Connor, J. H.; Altug, H. An Optofluidic Nanoplasmonic Biosensor for Direct Detection of Live Viruses from Biological Media. Nano Lett. 2010, 10 (12), 4962–4969. https://doi.org/10.1021/nl103025u.

(24) Kim, I. T.; Kihm, K. D. Label-Free Visualization of Microfluidic Mixture Concentration Fields Using a Surface Plasmon Resonance (Spr) Reflectance Imaging. Exp. Fluids 2006, 41 (6), 905–916. https://doi.org/10.1007/s00348-006-0210-1.

(25) Lesuffleur, A.; Im, H.; Lindquist, N. C.; Lim, K. S.; Oh, S.-H. Laser-Illuminated Nanohole Arrays for Multiplex Plasmonic Microarray Sensing. Opt. Express 2008, 16 (1), 219. https://doi.org/10.1364/OE.16.000219.

(26) Escobedo, C.; Vincent, S.; Choudhury, A. I. K.; Campbell, J.; Brolo, A. G.; Sinton, D.; Gordon, R. Integrated Nanohole Array Surface Plasmon Resonance Sensing Device Using a Dual-Wavelength Source. J. Micromechanics Microengineering 2011, 21 (11), 115001. https://doi.org/10.1088/0960-1317/21/11/115001.

(27) Peterson, A. W.; Halter, M.; Tona, A.; Plant, A. L. High Resolution Surface Plasmon Resonance Imaging for Single Cells. BMC Cell Biol. 2014, 15 (1), 35. https://doi.org/10.1186/1471-2121-15-35.

(28) Shpacovitch, V.; Temchura, V.; Matrosovich, M.; Hamacher, J.; Skolnik, J.; Libuschewski, P.; Siedhoff, D.; Weichert, F.; Marwedel, P.; Müller, H.; Überla, K.; Hergenröder, R.; Zybin, A. Application of Surface Plasmon Resonance Imaging Technique for the Detection of Single Spherical Biological Submicrometer Particles. Anal. Biochem. 2015, 486, 62–69. https://doi.org/10.1016/j.ab.2015.06.022.

(29) Im, H.; Lee, S. H.; Wittenberg, N. J.; Johnson, T. W.; Lindquist, N. C.; Nagpal, P.; Norris, D. J.; Oh, S.-H. Template-Stripped Smooth Ag Nanohole Arrays with Silica Shells for Surface Plasmon Resonance Biosensing. ACS Nano 2011, 5 (8), 6244–6253. https://doi.org/10.1021/nn202013v.

(30) Miller, J. H. Experiments in Molecular Genetics; Cold Spring Harbor Laboratory: New york, 1972.

(31) Barnes, W. L.; Dereux, A.; Ebbesen, T. W. Surface Plasmon Subwavelength Optics. Nature 2003, 424 (6950), 824–830. https://doi.org/10.1038/nature01937.

(32) Brolo, A. G.; Gordon, R.; Leathem, B.; Kavanagh, K. L. Surface Plasmon Sensor Based on the Enhanced Light Transmission through Arrays of Nanoholes in Gold Films. Langmuir 2004, 20 (12), 4813–4815. https://doi.org/10.1021/la0493621.

(33) Lee, M. H.; Gao, H.; Henzie, J.; Odom, T. W. Microscale Arrays of Nanoscale Holes. Small 2007, 3 (12), 2029–2033. https://doi.org/10.1002/smll.200700499.

(34) Hwang, G. M.; Pang, L.; Mullen, E. H.; Fainman, Y. Plasmonic Sensing of Biological Analytes Through Nanoholes. IEEE Sens. J. 2008, 8 (12), 2074–2079. https://doi.org/10.1109/JSEN.2008.2007663.

(35) Nikaido, H.; Vaara, M. Molecular Basis of Bacterial Outer Membrane Permeability. Microbiol. Rev. 1985, 49 (1), 1–32. https://doi.org/10.1128/MMBR.67.4.593-656.2003.

(36) Horwitz, W.; Lauwaars, M.; Sp, L.; Prof, S.; Vrije, M.; Brussel, U.; Prof, B.; Miller, J.; Nyeland, M. B.; Empa, R.; Gallen, S.; Prof, S.; Smeyers-Verbeke, J.; Suchanek, M.;

Verplaetse, H.; Walsh, M.; Wegscheider, P. W.; Westwood, D.; Agency, E.; Mr, U.; Van De Wiel, H. J. The Fitness for Purpose of Analytical Methods; 1998; Vol. 1.

(37) Kass, E. H.; Finland, M. Asymptomatic Infections of the Urinary Tract*. J. Urol. 2002, 168 (2), 420–424. https://doi.org/10.1016/S0022-5347(05)64650-2.

Chapter 4

Selective Uropathogenic *E. coli* Detection Using Crossed Surface-Relief Gratings

With minor changes to fulfill formatting requirements, this chapter is as it appears in: Srijit Nair, Juan Gomez-Cruz, Ángel Manjarrez-Hernandez, Gabriel Ascanio, Ribal Georges Sabat and Carlos Escobedo. *Sensors* **2018**, *18*(11), 3634.

Abstract: Urinary tract infections (UTIs) are one of the major burdens on public healthcare worldwide. One of the primary causes of UTIs is the invasion of the urinary tract by uropathogenic *Escherichia coli* (UPEC). Improper treatment of bacterial infections like UTIs with broad-spectrum antibiotics has contributed to the rise of antimicrobial resistance, necessitating the development of an inexpensive, rapid and accurate detection of UPEC. Here, we present real-time, selective and label-free detection of UPEC using crossed surface-relief gratings (CSRGs) as nanometallic sensors incorporated into an optical sensing platform. CSRGs enable real-time sensing due to their unique surface plasmon resonance (SPR)-based light energy exchange, resulting in detection of a very-narrow-bandwidth SPR signal after the elimination of residual incident light. The platform's sensing ability is experimentally demonstrated by the detection of bulk refractive index (RI) changes, with a bulk sensitivity of 382.2 nm/RIU and a resolution in the order of 10^{-6} RIU. We also demonstrate, for the first time, CSRG-based real-time selective capture and detection of UPEC in phosphate-buffered saline (PBS), in clinically relevant concentrations, as opposed to other UTI-causing Gram-negative bacteria. The platform's detection limit is calculated to be 10^5 CFU/mL (concentration on par with the clinical threshold for UTI diagnosis), with a dynamic range spanning four orders of magnitude. This work paves the way for the development of inexpensive point-of-

care diagnosis devices focusing on effective treatment of UTIs, which are a burden on public healthcare due to the rise in the number of cases and their recurrences in the recent past.

4.1 Introduction

Urinary tract infections (UTIs) are one of the most common bacterial infections worldwide. These infections are associated with escalating healthcare costs, with an estimated 10.5 million hospital visits in the United States alone in 2007, resulting in a direct and nondirect healthcare expenditure of over $2 billion.[1,2] In over 80% of cases of UTIs, the primary culprit is uropathogenic *Escherichia coli* (UPEC), which is also a major cause of many community- and healthcare-associated diseases.[3,4] The immune system controls the susceptibility of UTIs in humans and, depending on the individual's immunity, UPECs may invade the epithelial cell lining along the urinary tract, where they grow and multiply, invading eventually other sites via the bloodstream.[5,6] UPEC detection in laboratories usually involves biochemical assays like nitrite and/or esterase tests using serological techniques, which suffer from a high probability of false-positive results.[7] At the same time, improper drug administration increases the risk of developing antibiotic-resistant bacteria.[4] Other detection techniques involve established urine culture analysis, which is time consuming (3 to 7 days), laborious and requires specialized laboratory technicians to perform.[8] Recently, genome-based detection techniques employing polymerase chain reaction (PCR) have brought the timeline of detection to a few hours.[8] These techniques, however, require highly specialized personnel to extract the genomic material for signal amplification, through tedious pretreatment methods such as cell lysis[9] and electrophoresis,[10] increasing the overall cost dramatically, and thus limiting their applicability. For these reasons, the development of simple, cost-effective and time-saving devices for healthcare applications is highly sought after by the scientific community.[11] In this context, there is a timely opportunity for new healthcare diagnosis technologies to be paired with or integrated into portable electronics, which have flooded the consumer electronics market over the past few years.[12] Personal devices, such as smartphones, which have become omnipresent in recent times, provide a powerful tool for development of fully integrated point-of-care (POC) devices as diagnostic platforms.[13–15] With the advancement in fields of microfluidics, immunology, colorimetry, electrochemistry, light scattering-based approaches, surface plasmon resonance (SPR) and so on, researchers have developed on-site POC devices utilizing smartphone-based diagnostic platforms.[16–19]

Nanoplasmonic sensors supporting SPR have been employed in various biosensing applications in the past.[20–26] In terms of the design of POC devices, metallic nanostructures such as surface-relief gratings (SRGs) offer several key advantages including very small footprint, portability and compatibility with collinear optics, providing easiness of integration with other microsystems.[27,28] Since surface plasmons (SPs) in SRGs can be precisely tuned by controlling the grating fabrication parameters, such as the depth and pitch, this provides a unique avenue for the development of biomedical devices at low operational and fabrication cost.[29,30]

Recently, crossed surface-relief gratings (CSRGs) have been proven to be low-cost nanoplasmonic biosensors with much-improved sensing abilities compared to traditional SRGs.[23] SPs in SRGs are excited when incident light beam polarization is oriented along the grating vector, leading to the excitation of a wavelength-specific SP on a metal-coated grating.[31] This SP is normally observed as an enhanced transmission at the SPR-specific wavelength for polychromatic incident light depending not only on the light polarization, but also on the light incidence angle, the grating pitch and the refractive indices of the dielectric and the metal. CSRGs provide a different approach in SPR-based biosensing since they consist of orthogonally superimposed SRGs, allowing SPR excitation in two perpendicular light polarizations. When an incident light is polarized along the grating vector of one SRG, plasmons are excited at the metal–dielectric interface and an energy exchange takes place where the SPR resonant light is then re-radiated by the second grating in the orthogonal light polarization compared to the incident light.[32] Due to this unique phenomenon, when a broadband polychromatic light is incident on a CSRG placed between two crossed polarizers, only a narrow bandwidth corresponding to the SPR signal is transmitted, thus eliminating the rest of the incident light. Compared to other metallic nanostructures, sensing with this technique requires virtually no post-acquisition data processing, since the SPR signal is measured directly.

In this work, we present a fully integrated UPEC detection platform developed from off-the-shelf, low-cost optical components, employing CSRGs as optical sensors, with an envelope of 62.5 cm^3 (2.5 cm × 2.5 cm × 10 cm). The platform consists of inexpensive smartphone-analogous white LED, dichroic polarizers and a portable USB spectrometer, making it suitable for point-of-care and other applications requiring portability. The sensitivity of the platform is 382.2 nm/RIU, based on bulk refractive index change tests. The platform was tested for the label-free detection of UPEC in real time, and the selectivity of the platform for UPEC was further demonstrated by performing the same experimental assays with other Gram-negative, UTI-causing bacteria. This demonstrates the potential of the platform for real-world applications and represents the first demonstration of CSRG-based UPEC detection.

4.2 Materials and methods

4.2.1 Azo-glass film

Azo-glass (DR1-glass (3 wt %) solution in dichloromethane) was prepared according to the steps described elsewhere.[33] The solution was mechanically shaken for 1 h, then filtered via a 0.45 µm syringe filter (EMD Millipore, Merck KGaA, Darmstadt, Germany). Approximately 500 µL of the azo-glass solution was spin-coated on a soda lime glass slide with dimensions of 2.5 cm × 2.5 cm. Spin-coating was performed utilizing a Headway Research spin-coater (1000 rpm, 20 s), resulting in ~200-nm-thick films. The thickness of the azo-glass was measured with a Sloan Dektak II surface profiler (Veeco Instruments Inc., Plainview, NY, USA). Spin-coated substrates were later dried in a Yamato ADP-21 oven at 95 °C for 1 h, to evaporate any remaining solvent.

4.2.2 CSRG Fabrication

Orthogonally superimposed SRGs were fabricated as per the steps mentioned in.[23,32] A solid-state diode-pumped laser (Coherent Inc., Santa Clara, CA, USA, Verdi V5, $\lambda = 532$ nm) with an irradiance of 382 mW/cm^2 in conjugation with a Lloyd mirror setup was used to generate a sinusoidal interference pattern on the azo-glass-coated substrates. This holographic exposure was achieved by two interfering beams, one inciting directly from the laser, and one reflected upon the 3×3 cm^2 Lloyd mirror placed orthogonally to the sample. The resulting sinusoidal pattern, which was set to achieve 450 nm periodicity, was imprinted on the azo-glass substrate as SRGs and the area of the SRGs was controlled by a variable iris placed before the sample. With an opening of 1 cm in diameter, a grating area of 0.39 cm^2 was achieved. After the first inscription to generate the SRG structure, the substrate was rotated by 90° and exposed to the laser interference pattern again, to generate two superimposed CSRGs with an identical pitch of 450. Subsequently, a 60-nm-thick Au film was deposited using a Bal-Tec SCD 050 sputter coater ($I = 50$ mA, $t = 150$ s), resulting in Au–CSRGs used in this work.

4.2.3 Experimental Setup

A 3D-printed custom-made assembly consisting of a 3.5 V, 20 mA, white LED (LED-w5h-ac-h110, SiLed, Mexico) used in conjugation with a plano-convex lens (7.9 mm diameter, 8 mm focal length, Edmund Optics Inc., NJ, USA) functioned as the light source. A holder was 3D-printed, using a Miicraft+ (Miicraft, Hsinchu, Taiwan) 3D printer, in order to position and collimate the LED light vertically on the sensing substrate. A horizontal polarizer (TECHSPEC® Wire Grid Polarizing Film, Edmund Optics Inc., Barrington, NJ, USA) was placed directly underneath the

3D-printed assembly, accompanied by a variable iris to control the spot size of the light incident on the CSRGs. A custom sample holder, mounting the CSRGs, was positioned directly beneath the iris and a second polarizer in vertical orientation was placed after the sample to eliminate residual light after the SPR conversion. The fiber optic probe from a UV-vis spectrometer (USB 2000+, Ocean Optics, Largo, FL, USA) was positioned underneath the horizontal polarizer for maximum signal capture. All the components were arranged in a collinear arrangement atop a vertical optical rail.

4.2.4 Bacteria Culture

Bacteria *E. coli* O6:H1 (strain CFT073/ATCC 700928/UPEC), *Klebsiella pneumonia*, *Pseudomonas aeruginosa*, and *Proteus mirabilis* were routinely grown at 37 °C in Luria-Bertani (LB) medium. Overnight cultures resulted in bacterial concentration of 10^9 colony-forming units (CFU)/mL.

4.2.5 Antibody Production

Polyclonal rabbit antiserum to *E. coli* was prepared by immunization with cell envelopes. Strain CFT073 was grown overnight at 37 °C in M9 defined culture medium (42 mM Na_2HPO_4, 22 mM KH_2PO_4, 9 mM NaCl, 18 mM NH_4Cl, 1 mM $MgSO_4$, 0.1 mM $CaCl_2$ and 0.2% (w/v) glucose),[34] supplemented with 0.5 g/L of Peptone. The bacterial pellet was resuspended in 50 mM Tris-HCl, 5 mM EDTA (pH 7.5) containing protease inhibitor cocktail (Roche, Basel-City, Basel, Switzerland) and disrupted by ultrasonication with two 40 s pulses at low-power output, each followed by a 2-min pause, using a high-intensity ultrasonic processor (50-Watt Model, Sonics Materials Inc. Danbury, CT, USA); unbroken cells were removed by centrifugation (12,000× *g* for 10 min, 4 °C). Cell envelopes were collected by ultracentrifugation (50,000× *g* for 30 min, 4 °C) and dissolved in PBS (pH 7.4). The envelope solution was injected subcutaneously (in multiple sites, 0.5 mg without any adjuvant) into rabbits. The animals were boosted 3 and 6 weeks later with the same membrane solution. Blood was collected from the central auricular vein of each ear 15 days later.

4.2.6 Bulk RI Sensing Experiments

A thin polydimethylsiloxane-siloxane (PDMS, Sylgard 184, Dow Corning, Midland, MI, USA) layer, of approximately 2 mm in thickness, was prepared by methods described elsewhere.[35] An 8 mm × 8 mm hole was cut onto a 2 cm × 2 cm piece of the prepared thin PDMS layer, and it was placed on top of the crossed pattern region of the CSRGs. Sucrose solutions in deionized water with different weight percentages (5%, 10%, 15% and 20%) were prepared to be used as test solutions for bulk refractive index sensing. The refractive indices of the solutions were measured utilizing an Abbe refractometer (Shanghai Optical Instruments Co. Ltd., Shanghai, China).

4.2.7 Bacterial Detection

The surface of the CSRGs was cleaned and prepared by rinsing with 10% acetone and deionized water before the bacterial immobilization. Subsequently, the test solution was dispensed in the PDMS well to be hosted over the CSRG surface. Next, a baseline signal was acquired after introducing phosphate-buffered saline (PBS) solution into the PDMS well. The SPR peak acquired corresponding to the PBS transmission signal was used to calibrate the SPR peak-shift observed in the later part of the experiment. Next, UPEC-specific antibody solution was introduced onto the surface of CSRGs, and the corresponding SPR signal was recorded for 15 min. Thereafter, the sample was rinsed with PBS solution to discard any antibody not attached to the surface. The bacterial suspensions in PBS were inserted, recording the corresponding SPR peak shifts for 15 min. For UPEC, the transmission spectra from the CSRGs were acquired in real time, every 2 min. For other bacteria, the transmission spectra were obtained every 4 min.

4.3 Results and discussion

4.3.1 Crossed Surface-Relief Gratings

Figure 4.1a shows the CSRG nanofabrication procedure. The nanostructures were fabricated on substrates coated with azo-glass through a laser inscription technique. The SPR signal associated with CSRGs is attributed to the SPR energy conversion occurring between the individual SRGs. For normally incident light, the SPR excitation wavelength (λ_{SPR}) depends on the pitch (Λ) of the gratings, and the propagation characteristics of the media such as the dielectric permittivities of the metallic film, ε_m, and the surrounding dielectric medium, ε_d. The intensity or signal strength of the standing-wave surface plasmon is dependent on the depth of the gratings. For CSRGs, the SPR energy conversion occurs at λ_{SPR} when the light momentum is phase-matched between the diffracted incident light and the surface plasmon. Thus, for normal light incidence, λ_{SPR} can be represented as:

$$\lambda_{SPR} = \eta\Lambda\ [\varepsilon_m/ (\eta^2 + \varepsilon_m)]^{1/2}, \tag{4.1}$$

where η is the refractive index of the surrounding dielectric medium, and $\eta = (\varepsilon_d)^{1/2}$. From equation (4.1), it can be inferred that an increase in η would result in an increase in λ_{SPR}. The thickness of the azo-glass layer also plays an important role in transmission spectroscopy since an azo-glass film absorbs light below 550 nm. Thus, a thick azo-glass film may result in a decreased surface plasmon signal in transmission. On the other hand, a very thin coating of azo-glass may result in shallow gratings, greatly reducing the intensity of the transmitted SPR signal. Accordingly, the thickness of azo-glass film was optimised to approximately 200 nm for all the fabricated sensors. Also, to avoid the absorbance by azo-glass, the pitch of the gratings was chosen to excite plasmons above 600 nm. Another factor that influenced the choice of pitch of the gratings was the light source. Since the system is intended for smartphone-based platforms, the white LED used in this work is analogous to a smartphone flash LED. As evident from Figure 4.1b, the spectra of the white

LED used for this work has a maximum around 550 nm, eventually tailing-off until there is no light above 700 nm. Lastly, it must be considered that the optical platform is to be employed for water-based samples: sucrose solutions, PBS and bacterial solutions. Taking all the aforementioned factors into account, it was desirable to achieve the SPR signal in the range of 600–700 nm for the test solutions. From equation (4.1), based on 450-nm pitch gratings, a theoretical λ_{SPR} of 648 nm can be calculated for water as the surrounding dielectric medium. Using this input parameter, 450-nm-pitch CSRGs were fabricated by orthogonal superimposition of individual SRGs with identical 450-nm pitch. First, a 450-nm-pitch SRG was laser-inscribed on the azo-glass substrates using a solid-state diode-pumped laser (irradiance = 382 mW/cm^2) by direct holographic exposure for 300 s. Next, the substrate was rotated 90°, and a second SRG, superimposed on the initial grating, was laser-inscribed for 60 s. This resulted in orthogonally superimposed SRGs (i.e., CSRGs) of similar depth and diffraction efficiencies. Surface topography analysis using atomic force microscopy (AFM) shows the generation of CSRGs with a depth of c.a. 75 nm and desired pitch of 450 nm, as shown in Figure 4.1c. Subsequently, sputter deposition was performed to coat the fabricated CSRGs with 60-nm-thick Au film. Figure 4.1d shows the actual CSRG sensors, with the grating region showing the multi-colored diffractions. It is worth mentioning that the nanofabrication protocol, involving the azo-glass, provides a cheaper alternative to the clean-room-based techniques, and at the same time, allows nanometer precision in fabrication of gratings by controlling the fabrication parameters such as laser power, laser angle of incidence on the substrate, and time of exposure. This permits precise control over the depth and pitch of the gratings, allowing the freedom to design CSRGs based on the desired SPR signal wavelength.

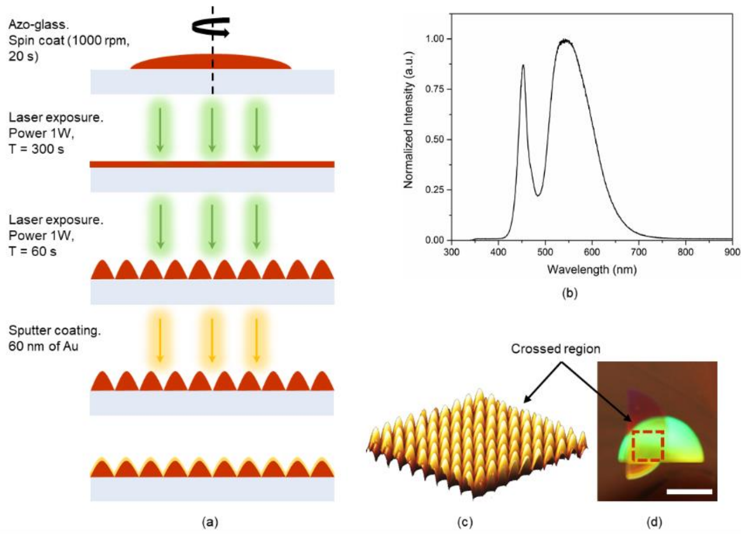

Figure 4.1 (a) Schematics of the fabrication procedure for CSRGs. (b) Normalized spectra for white LED used in this work. (c) AFM scan of 4 µm × 4 µm crossed region showing the orthogonally superimposed SRGs. (d) Actual image of the fabricated CSRGs with the crossed region marked with red box. White scale bar corresponds to 1 cm.

4.3.2 Optical Characterization

As the system is intended to be used, ultimately, as a smartphone-based platform, one of the critical goals was to reduce the footprint of the optical platform. Figure 4.2 shows the schematic representation of the experimental setup developed for this work. Collimated white light from the 3D-printed assembly was first directed towards the horizontally aligned polarizer. The horizontally polarized light was then incident on the metallic CSRGs. At this juncture, surface plasmons are excited at the metal–dielectric interface of the CSRGs, by the first grating having a horizontal grating vector. An SPR energy exchange then occurs between the first grating and its orthogonal component, having a vertical grating vector. This SPR energy is then re-radiated by the second grating, as explained elsewhere.[23,32] This resulting out-coupled light has a polarization orthogonal to the incident horizontally polarized light. Therefore, placing a vertical polarizer downstream from the CSRGs eliminates the entire incident light, except for the re-radiated SPR signal from the

CSRGs. This unique feature allows acquisition of SPR signals without any further normalization of the transmitted light (with the transmission spectra of gold or source light).

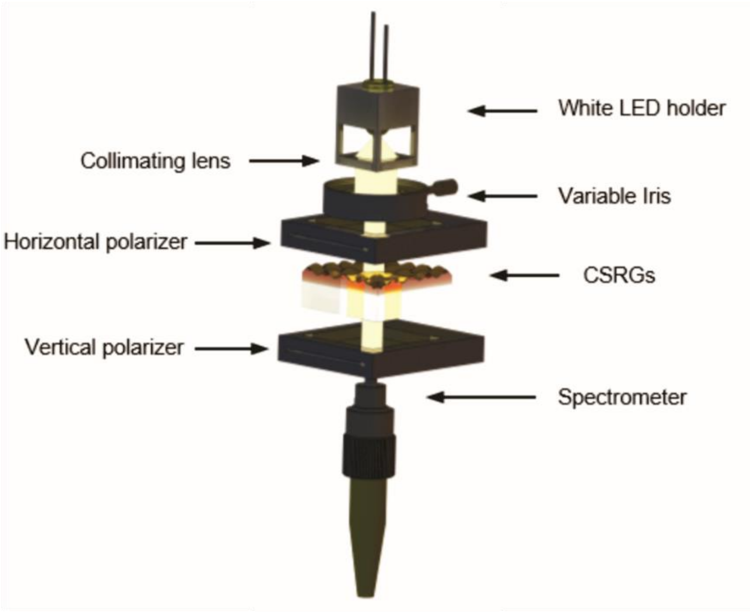

Figure 4.2 Schematic of the optical platform for transmission-based spectroscopy using CSRGs. All the elements are arranged in a collinear arrangement on a vertical rail. The light from the white LED passes through a variable iris, to control the spot diameter upon the horizontal polarizer, which is then incident on the CSRGs exciting the plasmons. The resulting out-coupled light then traverses the vertical polarizer, annulling all residual light from the white LED source, except the plasmonic signal detected by the spectrometer.

4.3.3 Bulk Refractive Index Sensing

Figure 4.3a shows the SPR signal acquired for deionised water using two different CSRGs, illuminated by a broadband halogen lamp, with the first CSRG having equal pitches of $\Lambda = 450$ nm and the second CSRG having equal pitches of $\Lambda = 550$ nm. From equation (4.1), the theoretically calculated λ_{SPR} for deionised water is 648 nm and 765 nm for $\Lambda = 450$ nm and 550 nm, respectively. Experimentally, λ_{SPR} for deionised water, calculated from the acquired spectra, was found to be 637 nm and 761 nm. The difference between the theoretical and observed λ_{SPR} is mainly due to the flat interface approximation considered when deriving equation (4.1). Nonetheless, these values are sufficiently close to display the precision of the nanofabrication method in tailoring the SPR response with respect to the end-application. Next, the performance of the miniaturized setup was evaluated to detect changes in the bulk refractive index by using aqueous sucrose solutions of 5%, 10%, 15% and 20% concentration (w/v), with respective RIs of 1.337, 1.344, 1.351 and 1.357, measured using the Abbe refractometer. A thin PDMS slab (2 cm × 2 cm) with an 8 mm × 8 mm chamber was placed on the CSRGs, in order to allow liquid–metal contact. The liquid in the chamber, ~140 µL, was covered with a cover slip to eliminate any potential lensing effect. The transmitted spectrum was acquired for each solution, as per the setup described previously. Figure 4.3b shows the spectra, and corresponding SPR peaks, of the sucrose test solutions. The SPR spectrum shows a characteristic red-shifting, corresponding to the increase in RI, as explained earlier and as prescribed by equation (4.1). The SPR signals were normalized and the total peak-shift at 80% maximum intensity was recorded. Figure 4.3c shows the recorded linear peak-shift associated with the increments in the refractive indices of the test solutions. The sensitivity of the platform, obtained from the linear fit of the peak-shift, was 382.2 nm/RIU, which is comparable to previously reported values of SRG-based sensors operating in transmission mode.[36] It should also be noted that the platform presented here employs off-the-shelf and inexpensive optical components, lowering the device fabrication cost considerably as compared to similar systems reported previously.[23] The resolution of our system, based on calculated sensitivity and system repeatability of 10^{-3} nm, is 10^{-6} RIU.[37] This value is particularly important since it gives information about the efficacy of our device by taking the system noise into account.

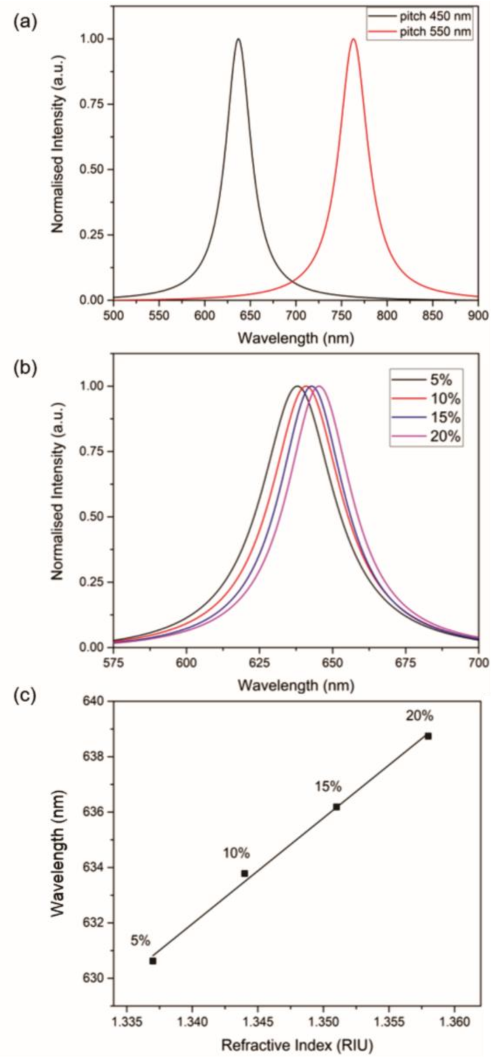

Figure 4.3 Bulk sensitivity test. (a) Normalized SPR peaks for water acquired using two different pitch CSRGs (450 nm and 550 nm). (b) Normalized SPR peaks for aqueous sucrose solutions of different concentrations (5%, 10%, 15% and 20%). The SPR spectrum shifts toward red as the refractive index increases. (c) Wavelength (nm) vs refractive index (RIU) for each solution. The sensitivity of the platform is 382.2 nm/RIU, based on the slope of the linear fit. No error bars are indicated since the standard deviation for $N = 3$ is smaller than the size of the symbol representing the mean in the graph.

4.3.3 Bacterial Detection

The utility of the sensing platform to detect UPEC was investigated. The employed schema focused on detection of intact bacteria, as opposed to genome-based sequencing techniques, which involve time-consuming steps such as DNA extraction, PCR and subsequent processing. Also, clinical UTI detection involving urine culture is laborious and involves qualified technicians and specialized facilities, resulting in delayed detection timelines. The platform presented here overcomes the drawbacks of such methods, reducing the UPEC detection time from days to minutes. UPEC-specific antibodies, prepared as described in the Methods section, immobilize the bacteria by binding to their outer membrane. Binding is facilitated by anchoring of proteins, phospholipids and oligosaccharides to the cells' surface.[38] The surface of the CSRGs was functionalized with UPEC-specific antibodies to enable whole-bacterium detection. Figure 4.4a shows the relative SPR peak shift observed in real time for both antibodies ($t = 0$ to $t = 15$ min) and for detection of bacteria ($t > 15$ min) taking the signal for PBS as baseline ($t = 0$ min). The UPEC-specific antibodies were incubated on the CSRG surface for 15 min, and the transmission spectra were acquired every 2 min. The immobilization of the antibodies on the surface of CSRGs promoted an increase in the local refractive index at the metal–dielectric interface. This increase was reflected as a red-shift in the transmission spectra (i.e., SPR peak) as theorized by equation (4.1). Next, UPEC solution in PBS (10^9 CFU/mL) was added to the antibody-modified CSRG surface, and the transmission spectra were acquired every 2 min for another 15 min. The real-time displacement in the SPR spectra, due to the antibody and bacteria immobilization, is presented in Figure 4.4a as a function of time (black square). As evidenced by the inset in Figure 4.4a, the addition of antibody and bacteria resulted in a respective 0.9 nm and 2.13 nm shift, compared to the PBS baseline. Another goal of this work was to demonstrate the platform's specificity in detection of UPEC. The selectivity of the platform was validated by performing the same experiment with other UTI-causing, Gram-negative bacteria, namely: *Klebsiella pneumonia*, *Pseudomonas aeruginosa* and *Proteus mirabilis*. After initial incubation of UPEC-specific antibody for 15 min, 140 µL of the bacterial solution in PBS (10^9 CFU/mL) was added, and the transmission spectra were recorded for 15 min, at five-min intervals. Colored symbols (other than black) after $t = 15$ min represent other nonspecific bacteria. The platform was highly specific for the detection of UPEC, evident from the very small shift observed with the other Gram-negative bacteria, as shown in Figure 4.4a. The platform was also tested for any potential drifting by monitoring the signal over time using DI water, PBS solution, and bound streptavidin to a cysteamine–biotin complex immobilized atop the CSRG surface, under quasi-steady-state conditions as reported elsewhere[23] (details available in the Supplementary Materials). The limit of detection (LOD) of the CSRG-based platform was determined by a dose-based binding study. UPEC solutions in PBS with concentrations of 10^5, 10^7 and 10^9 CFU/mL were used in this experiment. Figure 4.4b shows the relative shift of the plasmonic signal, detected from the antibody-functionalized CSRG surface upon addition of different concentrations of UPEC solution. Based on this study and taking into consideration the resolution of the spectrometer, we calculated the LOD of the platform to be approximately 10^5 CFU/mL, with a dynamic range of four orders of magnitude (10^5–10^9 (CFU/mL)).[39,40] This value is on par with the clinical threshold for UPEC concentrations (10^5 CFU/mL) in UTI diagnosis.[3] The SPR peak-shifts observed in this experiment are accordant with the bacterial detection studies previously reported in the literature.[41–43] This experiment, notably, represents the first demonstration of CSRG-based bacterial detection.

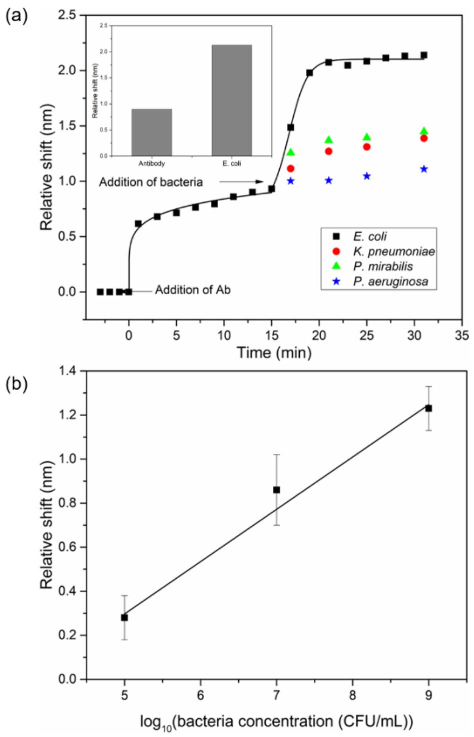

Figure 4.4 Selective uropathogenic *E. coli* (UPEC) detection assay. (a) Real-time relative shift corresponding to capture of UPEC bacteria, and other UTI-causing Gram-negative bacteria at concentration 10^9 CFU/mL. Inset shows the relative cumulative shift in SPR signal observed after binding of UPEC-specific antibody and UPEC. (b) Relative shift corresponding to different concentrations of UPEC in PBS buffer (10^5, 10^7, 10^9 CFU/mL). Error bars indicate the standard deviation observed for each bacterial measurement for $N = 3$.

4.4 Conclusions

This work presents the first demonstration of label-free detection of bacteria by CSRGs as a nanoplasmonic sensor. A fully integrated, miniaturized (2.5 cm × 2.5 cm × 10 cm) platform consisting of smartphone-compatible, inexpensive optical and electronic components in conjugation with CSRGs is employed for SPR-based sensing. The platform demonstrates a sensitivity of 382.2 nm/RIU, with a resolution of 10^{-6} RIU, for bulk refractive index changes. The sensitivity of the platform depends not only on the integrity and characteristics of the metallic nanostructure, but also on the optical assembly, including the quality of its components, employed for sensing. Despite the low-cost optical components used in this work, the sensitivity is still on par with similar nanoplasmonic assemblies in the literature. We employed the platform for selective detection of UPEC suspended in PBS solution, demonstrating its potential in real-world applications. The platform was able to detect UPEC capture by immobilized antibodies on the CSRG surface, at concentrations from 10^5 to 10^9 CFU/mL, with the whole detection being performed in 35 min as opposed to clinical detection timelines of days. The platform has a dynamic range spanning four orders of magnitude, with an experimental LOD for UPEC detection in PBS to be ~10^5 CFU/mL, which is on par with the physiological limit for UTI diagnosis. Along with the low cost of the platform and sensor, the detection was carried out with minimal sample pretreatment as opposed to established genomic techniques, which require time-consuming assays to extract and amplify bacterial genome. In the future, detection of UPEC in complex biological matrices, like human urine, would further advance and solidify the platform's applicability as a point-of-care device. The platform, however, had limitations in terms of detection of lower concentrations of bacteria due to the resolution of the USB spectrometer. However, this drawback can be overcome by using SPR imaging (SPRi) techniques. Imaging components such as complementary metal-oxide semiconductor (CMOS) may improve the resolution of the platform considerably. Furthermore, incorporation of microfluidic components could improve upon the functionality of the detection platform for complex applications including multiplexed sensing. Overall, the platform presented here has great potential to advance the field of smartphone-based sensing and telemedicine, with a wide range of applications.

4.5 References

(1) Foxman, B. Urinary Tract Infection Syndromes: Occurrence, Recurrence, Bacteriology, Risk Factors, and Disease Burden. Infect. Dis. Clin. North Am. 2014, 28 (1), 1–13. https://doi.org/10.1016/J.IDC.2013.09.003.

(2) Schappert, S. M.; Rechtsteiner, E. A. Ambulatory Medical Care Utilization Estimates for 2007. Vital Health Stat. 13. 2011, No. 169, 1–38. https://doi.org/10.1037/e587152010-001.

(3) Grabe, M.; Bjerklund-Johansen, T. E.; Botto, H.; Cai, T.; Çek, M.; Köves, B.; Naber, K. G.; Pickard, R. S.; Tenke, P.; Wagenlehner, F. Guidelines on Urological Infections. Eur. Assoc. Urol. 2015, 14.

(4) Weiner, L. M.; Webb, A. K.; Limbago, B.; Dudeck, M. A.; Patel, J.; Kallen, A. J.; Edwards, J. R.; Sievert, D. M. Antimicrobial-Resistant Pathogens Associated With Healthcare-Associated Infections: Summary of Data Reported to the National Healthcare Safety Network at the Centers for Disease Control and Prevention, 2011–2014. Infect. Control Hosp. Epidemiol. 2016, 37 (11), 1288–1301. https://doi.org/10.1017/ice.2016.174.

(5) Lewis, A. J.; Richards, A. C.; Mulvey, M. A. Invasion of Host Cells and Tissues by Uropathogenic Bacteria. Microbiol. Spectr. 2016, 4 (6). https://doi.org/10.1128/microbiolspec.UTI-0026-2016.

(6) Foxman, B. The Epidemiology of Urinary Tract Infection. Nat. Rev. Urol. 2010, 7 (12), 653–660. https://doi.org/10.1038/nrurol.2010.190.

(7) Wilson, M. L.; Gaido, L. Laboratory Diagnosis of Urinary Tract Infections in Adult Patients. Clin. Infect. Dis. 2004, 38 (8), 1150–1158. https://doi.org/10.1086/383029.

(8) Alocilja, E. C.; Radke, S. M. Market Analysis of Biosensors for Food Safety. Biosens. Bioelectron. 2003, 18 (5–6), 841–846. https://doi.org/10.1016/S0956-5663(03)00009-5.

(9) Escobedo, C.; Bürgel, S. C.; Kemmerling, S.; Sauter, N.; Braun, T.; Hierlemann, A. On-Chip Lysis of Mammalian Cells through a Handheld Corona Device. Lab Chip 2015, 15 (14), 2990–2997. https://doi.org/10.1039/C5LC00552C.

(10) Bürgel, S. C.; Escobedo, C.; Haandbæk, N.; Hierlemann, A. On-Chip Electroporation and Impedance Spectroscopy of Single-Cells. Sensors Actuators B Chem. 2015, 210, 82–90. https://doi.org/10.1016/J.SNB.2014.12.016.

(11) Liu, Y.; Liu, Q.; Chen, S.; Cheng, F.; Wang, H.; Peng, W. Surface Plasmon Resonance Biosensor Based on Smart Phone Platforms. Sci. Rep. 2015, 5 (1), 12864. https://doi.org/10.1038/srep12864.

(12) Darwish, A.; Hassanien, A. E. Wearable and Implantable Wireless Sensor Network Solutions for Healthcare Monitoring. Sensors 2011, 11 (6), 5561–5595. https://doi.org/10.3390/s110605561.

(13) Escobedo, C.; Vincent, S.; Choudhury, A. I. K.; Campbell, J.; Brolo, A. G.; Sinton, D.; Gordon, R. Integrated Nanohole Array Surface Plasmon Resonance Sensing Device Using a Dual-Wavelength Source. J. Micromechanics Microengineering 2011, 21 (11), 115001. https://doi.org/10.1088/0960-1317/21/11/115001.

(14) Dies, H.; Raveendran, J.; Escobedo, C.; Docoslis, A. Rapid Identification and Quantification of Illicit Drugs on Nanodendritic Surface-Enhanced Raman Scattering Substrates. Sensors Actuators B Chem. 2018, 257, 382–388. https://doi.org/10.1016/J.SNB.2017.10.181.

(15) Puiu, M.; Bala, C. SPR and SPR Imaging: Recent Trends in Developing Nanodevices for Detection and Real-Time Monitoring of Biomolecular Events. Sensors 2016, 16 (6), 870. https://doi.org/10.3390/s16060870.

(16) Laksanasopin, T.; Guo, T. W.; Nayak, S.; Sridhara, A. A.; Xie, S.; Olowookere, O. O.; Cadinu, P.; Meng, F.; Chee, N. H.; Kim, J.; Chin, C. D.; Munyazesa, E.; Mugwaneza, P.; Rai, A. J.; Mugisha, V.; Castro, A. R.; Steinmiller, D.; Linder, V.; Justman, J. E.; Nsanzimana, S.; Sia, S. K. A Smartphone Dongle for Diagnosis of Infectious Diseases at the Point of Care. Sci. Transl. Med. 2015, 7 (273), 273. https://doi.org/10.1126/scitranslmed.aaa0056.

(17) Chin, C. D.; Laksanasopin, T.; Cheung, Y. K.; Steinmiller, D.; Linder, V.; Parsa, H.; Wang, J.; Moore, H.; Rouse, R.; Umviligihozo, G.; Karita, E.; Mwambarangwe, L.; Braunstein, S. L.; van de Wijgert, J.; Sahabo, R.; Justman, J. E.; El-Sadr, W.; Sia, S. K. Microfluidics-Based Diagnostics of Infectious Diseases in the Developing World. Nat. Med. 2011, 17 (8), 1015–1019. https://doi.org/10.1038/nm.2408.

(18) Rateni, G.; Dario, P.; Cavallo, F. Smartphone-Based Food Diagnostic Technologies: A Review. Sensors 2017, 17 (6), 1453. https://doi.org/10.3390/s17061453.

(19) Liang, P.-S.; Park, T. S.; Yoon, J.-Y. Rapid and Reagentless Detection of Microbial Contamination within Meat Utilizing a Smartphone-Based Biosensor. Sci. Rep. 2014, 4. https://doi.org/10.1038/SREP05953.

(20) Homola, J. Surface Plasmon Resonance Sensors for Detection of Chemical and Biological Species. Chem. Rev. 2008, 108 (2), 462–493. https://doi.org/10.1021/cr068107d.

(21) Escobedo, C. On-Chip Nanohole Array Based Sensing: A Review. Lab on a Chip. Royal Society of Chemistry July 7, 2013, pp 2445–2463. https://doi.org/10.1039/c3lc50107h.

(22) Gomez-Cruz, J.; Nair, S.; Ascanio, G.; Escobedo, C. Flow-through Nanohole Array Based Sensor Implemented on Analogue Smartphone Components. In Proceedings of SPIE - The International Society for Optical Engineering; 2017; Vol. 10346. https://doi.org/10.1117/12.2272433.

(23) Nair, S.; Escobedo, C.; Sabat, R. G. Crossed Surface Relief Gratings as Nanoplasmonic Biosensors. ACS Sensors 2017, 2 (3), 379–385. https://doi.org/10.1021/acssensors.6b00696.

(24) Eftekhari, F.; Escobedo, C.; Ferreira, J.; Duan, X.; Girotto, E. M.; Brolo, A. G.; Gordon, R.; Sinton, D. Nanoholes As Nanochannels: Flow-through Plasmonic Sensing. Anal. Chem. 2009, 81 (11), 4308–4311. https://doi.org/10.1021/ac900221y.

(25) Urraca, J. L.; Barrios, C. A.; Canalejas-Tejero, V.; Orellana, G.; Moreno-Bondi, M. C. Molecular Recognition with Nanostructures Fabricated by Photopolymerization within Metallic Subwavelength Apertures. Nanoscale 2014, 6 (15), 8656–8663. https://doi.org/10.1039/c4nr01129e.

(26) Canalejas-Tejero, V.; Herranz, S.; Bellingham, A.; Moreno-Bondi, M. C.; Barrios, C. A. Passivated Aluminum Nanohole Arrays for Label-Free Biosensing Applications. ACS Appl. Mater. Interfaces 2014, 6 (2), 1005–1010. https://doi.org/10.1021/am404509f.

(27) Xu, B.-B.; Ma, Z.-C.; Wang, H.; Liu, X.-Q.; Zhang, Y.-L.; Zhang, X.-L.; Zhang, R.; Jiang, H.-B.; Sun, H.-B. A SERS-Active Microfluidic Device with Tunable Surface Plasmon Resonances. Electrophoresis 2011, 32 (23), 3378–3384. https://doi.org/10.1002/elps.201100309.

(28) Vala, M.; Chadt, K.; Piliarik, M.; Homola, J. High-Performance Compact SPR Sensor for Multi-Analyte Sensing. Sensors Actuators B Chem. 2010, 148 (2), 544–549. https://doi.org/10.1016/j.snb.2010.05.067.

(29) Yeh, W.-H.; Kleingartner, J.; Hillier, A. C. Wavelength Tunable Surface Plasmon Resonance-Enhanced Optical Transmission Through a Chirped Diffraction Grating. Anal. Chem. 2010, 82 (12), 4988–4993. https://doi.org/10.1021/ac100497w.

(30) Bhatta, D.; Stadden, E.; Hashem, E.; Sparrow, I. J. G.; Emmerson, G. D. Multi-Purpose Optical Biosensors for Real-Time Detection of Bacteria, Viruses and Toxins. Sensors Actuators B Chem. 2010, 149 (1), 233–238. https://doi.org/10.1016/j.snb.2010.05.040.

(31) Homola, J. Surface Plasmon Resonance Based Sensors; Springer Series on Chemical Sensors and Biosensors; Springer Berlin Heidelberg, 2006.

(32) Sabat, R. G.; Rochon, N.; Rochon, P. Dependence of Surface Plasmon Polarization Conversion on the Grating Pitch. J. Opt. Soc. Am. A 2010, 27 (3), 518. https://doi.org/10.1364/JOSAA.27.000518.

(33) Kirby, R.; Sabat, R. G.; Nunzi, J.-M.; Lebel, O. Disperse and Disordered: A Mexylaminotriazine-Substituted Azobenzene Derivative with Superior Glass and Surface Relief Grating Formation. J. Mater. Chem. C 2014, 2 (5), 841–847. https://doi.org/10.1039/C3TC32034K.

(34) Miller, J. H. Experiments in Molecular Genetics; Cold Spring Harbor Laboratory: New york, 1972.

(35) Duffy, D. C.; McDonald, J. C.; Schueller, O. J. A.; Whitesides, G. M. Rapid Prototyping of Microfluidic Systems in Poly(Dimethylsiloxane). Anal. Chem. 1998, 70 (23), 4974–4984. https://doi.org/10.1021/ac980656z.

(36) Monteiro, J. P.; Ferreira, J.; Sabat, R. G.; Rochon, P.; Santos, M. J. L.; Girotto, E. M. SPR Based Biosensor Using Surface Relief Grating in Transmission Mode. Sensors Actuators, B Chem. 2012, 174 (July 2015), 270–273. https://doi.org/10.1016/j.snb.2012.08.026.

(37) Hwang, G. M.; Pang, L.; Mullen, E. H.; Fainman, Y. Plasmonic Sensing of Biological Analytes Through Nanoholes. IEEE Sens. J. 2008, 8 (12), 2074–2079. https://doi.org/10.1109/JSEN.2008.2007663.

(38) Nikaido, H.; Vaara, M. Molecular Basis of Bacterial Outer Membrane Permeability. Microbiol. Rev. 1985, 49 (1), 1–32. https://doi.org/10.1128/MMBR.67.4.593-656.2003.

(39) Shrivastava, A.; Gupta, V. Methods for the Determination of Limit of Detection and Limit of Quantitation of the Analytical Methods. Chronicles Young Sci. 2011, 2 (1), 21. https://doi.org/10.4103/2229-5186.79345.

(40) Marusov, G.; Sweatt, A.; Pietrosimone, K.; Benson, D.; Geary, S. J.; Silbart, L. K.; Challa, S.; Lagoy, J.; Lawrence, D. A.; Lynes, M. A. A Microarray Biosensor for Multiplexed Detection of Microbes Using Grating-Coupled Surface Plasmon Resonance Imaging. Environ. Sci. Technol. 2012, 46 (1), 348–359. https://doi.org/10.1021/es201239f.

(41) Soler, M.; Belushkin, A.; Cavallini, A.; Kebbi-Beghdadi, C.; Greub, G.; Altug, H. Multiplexed Nanoplasmonic Biosensor for One-Step Simultaneous Detection of Chlamydia Trachomatis and Neisseria Gonorrhoeae in Urine. Biosens. Bioelectron. 2017, 94, 560–567. https://doi.org/10.1016/j.bios.2017.03.047.

(42) Gomez-Cruz, J.; Nair, S.; Manjarrez-Hernandez, A.; Gavilanes-Parra, S.; Ascanio, G.; Escobedo, C. Cost-Effective Flow-through Nanohole Array-Based Biosensing Platform for the Label-Free Detection of Uropathogenic E. Coli in Real Time. Biosens. Bioelectron. 2018, 106 (January), 105–110. https://doi.org/10.1016/j.bios.2018.01.055.

(43) Wang, Y.; Ye, Z.; Si, C.; Ying, Y. Subtractive Inhibition Assay for the Detection of E. Coli O157:H7 Using Surface Plasmon Resonance. Sensors 2011, 11 (3), 2728–2739. https://doi.org/10.3390/s110302728.

Chapter 5

Rapid label-free detection of intact pathogenic bacteria in situ via surface plasmon resonance imaging enabled by crossed surface relief gratings

With minor changes to fulfill formatting requirements, this chapter is as it appears in: Srijit Nair, Juan Gomez-Cruz, Ángel Manjarrez-Hernandez, Gabriel Ascanio, Ribal Georges Sabat and Carlos Escobedo. Analyst 145 (6), 2133-2142.

Abstract: The unique plasmonic energy exchange occurring within metallic crossed surface relief gratings (CSRGs) has recently motivated their use as biosensors. However, CSRG-based biosensing has been limited to spectroscopic techniques, failing to harness their potential for integration with ubiquitous portable electronics. Here, we introduce biosensing via surface plasmon resonance imaging (SPRi) enabled by CSRGs. The SPRi platform is fully integrated including optics and electronics, has bulk sensitivity of 613 Pixel Intensity Unit (PIU)/Refractive Index Unit (RIU), a resolution of 10^{-6} RIU and a signal-to-noise ratio of ~33 dB. Finite-Difference Time-Domain (FDTD) simulations confirm that CSRG-enabled SPRi is supported by an electric field intensity enhancement of ~ 30 times, due to plasmon resonance at the metal-dielectric interface. In the context of real-world biosensing applications, we demonstrate the rapid (< 35 min) and label-free detection of uropathogenic *E. coli* (UPEC) in PBS and human urine samples for concentrations ranging from 10^3 to 10^9 CFU/mL. The detection limit of the platform is ~100 CFU/mL, three orders of magnitude lower than the clinical detection limit for diagnosis of urinary tract infection. This work presents a new avenue for CSRGs as SPRi-based biosensing platforms and their great potential for integration with portable electronics for applications requiring in situ detection.

5.1 Introduction

Nanostructured metallic substrates supporting surface plasmon resonance (SPR) have been widely employed for the development of biosensing platforms.[1–10] Surface relief gratings (SRGs), in particular, allow direct coupling of normally incident light into surface plasmons (SPs) upon phase-matching the diffracted light wave number to that of the plasmon.[11] In contrast to other optical arrangements, such as the Kretschmann and Otto configurations, SRGs allow excitation of SPs using collinear optics. The plasmonic excitation results in the enhancement of the local electromagnetic fields at the metal-dielectric interface upon coupling the incident light into a surface plasmon polariton (SPP). SRGs have an inherent small footprint, which offers additional benefits in terms of portability and compatibility with other microsystems.[12] By controlling the grating topology, SRGs allow for precise and tunable SPs excitations, enabling the detection of target analytes – an important asset in the development for application-specific biosensors.[13–15] In the case of pathogenic bacterial detection, biosensors must allow for a rapid and sensitive response as the presence of even a single microorganism could cause infections, which represents a major challenge for SPR-based sensors in general.[16] Therefore, label-free and real-time sensing of whole pathogenic bacteria at very low concentrations in complex matrices, such as bodily fluids, is the epitome of early diagnosis of infectious diseases detection.

Crossed surface relief gratings (CSRGs) have been recently demonstrated as nanoplasmonic sensors that enable detection of biomolecular interactions in real-time, with a high sensitivity, suitable for the detection of ultralow concentrations of analytes.[17] CSRGs consist of two orthogonally superimposed gratings that exhibit a unique plasmonic energy exchange. When incident light on the CSRG is polarized along one of the grating vectors, SPs are excited at the metal-dielectric interface by that grating having its vector aligned with the incident light polarization. Subsequently, the energy exchange between the orthogonal gratings takes place, resulting in the re-radiation of the SPR energy with a polarization direction orthogonal to that of the original incident light.[18,19] Therefore, when broadband light is incident on a CSRG placed between two crossed polarizers, only a narrow and pitch-dependent bandwidth of the SPR-polarization-converted light is transmitted across the system as a single resonance peak with a high signal-to-noise ratio. This occurs because the orthogonal polarizers cancel the remaining light that has not coupled to the SPR. This unique SPR energy transfer enables a 3-fold sensitivity enhancement over conventional SRGs.[17] Until now, biosensing with CSRGs has been achieved via spectral interrogation.[17,20] Spectral interrogation invariably involves the use of a spectrometer for the acquisition of the SPR signal. For applications involving the detection of bacteria at low enough concentrations for early clinical diagnosis (e.g. $< 10^5$ CFU/mL for urinary tract infections (UTI)), large footprint and expensive spectrometers with high resolution are required.

Conversely, metallic nanostructures can also be employed for the recognition of biologically-relevant analytes using SPR imaging (SPRi) technique.[21–23] Unlike SPR spectral or SPR microscopy techniques[24] where a spectrometer or a microscope is utilized to interrogate the plasmonic response, SPRi employs a photodetector,[25] enabling the detection of minute variations in the SPR signal strength. Although CSRGs have never been demonstrated for SPRi, other SPRi-enabled platforms, such as subwavelength nanoapertures, have been used for cancer marker,[5] protein [26,27] and bacteria [28] detection. SPRi has been recently demonstrated with SRGs, by quantifying the light intensity variation from transmitted monochromatic light at the SPR wavelength.[29] In this technique, the intensity modulation corresponds to a shift in the linear region of the SPR spectral curve. Until now, SPRi-based sensing demonstrations that can be translated into real-world applications have involved the use of expensive and bulky components including CCD modules and microscope-based platforms.[8,30,31] The high cost and large footprint of these SPRi platforms represent a serious limitation when contending in the competitive point-of-care (POC) sensing arena.[24]

Here, we demonstrate that the plasmonic energy transfer occurring between the individual gratings in a CSRG can be exploited to obtain higher sensitivity SPRi. This work represents the first demonstration of CSRG-based SPR imaging, achieved through the intensity modulation of monochromatic incident light as opposed to traditional spectral interrogation using a broad-spectrum light source. The platform utilizes inexpensive 3D printed components in conjugation with a low-cost red LED, wire grid polarizers, a CMOS photodetector for the optical array and a Raspberry Pi unit for signal acquisition. The platform has a total footprint of only 2.5 cm × 2.5 cm × 10 cm. CSRGs structures were computer-assessed via Finite-difference time-domain (FDTD) simulations to show the electric field intensity distribution on the gold-coated CSRG surface, and transmission spectrum, to obtain the best fabrication parameters suitable for the SPRi platform. The optical response of the platform is characterized through the detection of changes in the bulk refractive index of aqueous sucrose solutions. In the context of real-world applications, we demonstrate the selective detection of uropathogenic *E. coli* (UPEC) in real-time and label-free fashion for bacterial concentrations spanning 6-orders of magnitude in both PBS and human urine, with a Limit of Detection (LOD) of ~100 CFU/mL.

5.2 Materials and Methods

5.2.1 Fabrication of nanostructures

CSRGs, according to the simulation parameters, were fabricated using the rapid and high-throughput interferometric patterning technique as presented in previous works.[17,18,20] Azo-glass (DR1-glass, 2.99 mM, 94%) solution was prepared according to the methods described elsewhere.[32] The solution was then diluted in dichloromethane to 3 wt%, thoroughly vortexed for 1 h and filtered via a 0.45 µm syringe filter (EMD Millipore, Merck KGaA, Darmstadt, Germany). A volume of 500 µL of the diluted solution was spin-coated on a pre-cleaned 2.5 cm × 2.5 cm Corning 0215 soda lime microscope glass slide (TED PELLA, INC., California, USA) using a Headway Research spincoater (Headway Research Inc. Garland, TX, USA) at 1000 RPM for 20 s. The spin-coated samples were then dried and annealed for 1 h at 90 ºC in a Yamato ADP-21 oven (Santa Clara, CA, USA) to generate a uniform azo-glass film of approximately 200 nm thick, verified by a Sloan Dektak II surface profiler (Veeco Instruments Inc., Plainview, NY, USA). CSRGs were fabricated on these substrates via a solid-state diode-pumped laser (COHERENT, USA, Verdi V5, λ = 532 nm) with an irradiance of 382 mW/cm^2. The laser beam passed through a spatial filter and was subsequently collimated. A quarter-waveplate was used to generate circular polarization, and the beam size was regulated with a variable iris to obtain a circular spot size of 1 cm in diameter. The nanofabrication procedure for creating CSRGs takes advantage of the unique photomechanical properties of azobenzene chromophores. Under the illumination of a laser beam interference pattern, azobenzene molecules uniformly displace from high to low irradiance regions due to a repetitive photoisomerization.[33] The collimated laser beam was then directed onto a Lloyd mirror interferometer consisting of a mirror positioned orthogonally to the azo-glass substrate surface. This resulted in the generation of an interference pattern, with half of the circularly polarized beam directly incident on the azo-glass surface while the other half of the beam is reflected off the mirror and onto the sample surface. This holographic exposure resulted in mass transport of the azo-molecules leading to the generation of nanopatterned SRGs. The azo-glass coated substrate was positioned in a configuration to achieve a grating periodicity or pitch of 450 nm. After the initial inscription of the SRGs (time of exposure = 300 s), the sample was rotated by 90º, and a second exposure for 60 s was performed to fabricate orthogonally superimposed SRGs. The second exposure time was shorter than the first in order to obtain orthogonal SRGs with almost identical modulation depths, thus near-identical diffraction efficiencies. This nano-fabrication protocol enables nanometer-level accuracy in the grating depth and pitch, all with a total process time of only 6 min. The pitch of the CSRG was designed to provide plasmonic resonances at a wavelength within the visible light spectrum, to enable the use of commercial devices for image acquisition, such as CMOS-based cameras. The pitch has no influence in the sensitivity of the CSRG in a biosensing context. However, a metallic film is required to achieve plasmonic excitation. In previous studies, thicknesses of c.a. 60 nm have been demonstrated to provide optimal SPR peaks that are suitable for sensing.[34,35] Therefore, 60 nm layer of gold was subsequently deposited using a Bal-Tec SCD 050 sputter coater (I = 50 mA, t = 150 s), to make Au-CSRGs.

5.2.2 Experimental setup

A 2 V, 20 mA, red LED (LED-w5h-ac-h110, SiLed, Mexico) with a peak intensity at 626 nm and a FWHM of 16 nm was used as the light source for the imaging experiments. The red LED, along with a plano-convex lens (7.9 mm diameter, 8 mm focal length, Edmund Optics Inc., NJ, USA) was housed in a custom-made 3D-printed assembly unit (Miicraft, Hsinchu, Taiwan) to position and collimate the LED light vertically on the sensing substrate. A horizontal polarizer (TECHSPEC® Wire Grid Polarizing Film, Edmund Optics Inc., NJ, USA) was placed after the 3D printed assembly, accompanied by a variable iris to control the spot size of the light incident on the CSRG. The Au-CSRG was mounted underneath the iris on a custom-made holder followed by a second polarizer orthogonal with respect to the first. This configuration eliminates residual light transmitted after the SPR conversion. The transmitted image acquisition was performed by a CMOS photodetector (Raspberry Pi Camera V2, Raspberry Pi Foundation, UK) that was collinearly aligned to the optical setup and synchronized with a Raspberry Pi 3 Model B (Raspberry Pi Foundation, UK).

5.2.3CSRGs topography and optical characterization

The CSRG structure was imaged using a Dimension Edge atomic force microscope (AFM) (Bruker, Massachusetts, USA). The AFM tip scanned a 5 µm × 5 µm area, using the peak-force tapping mode, with a scan rate of 1 Hz per line. The collected scans were then fitted using a built-in 2D plane fit function and analyzed using the Bruker NanoScope Analysis software to validate the fabrication parameters such as the pitch, depth, and quality of the grating. The plasmon resonance peak of the CSRG was corroborated using the optical setup mentioned above but with a tungsten-halogen light source (HL-200, Ocean Optics, USA) instead of an LED and a UV-VIS spectrometer (USB 2000+, Ocean Optics, USA) instead of the CMOS sensor.

5.2.4 CSRGs FDTD simulations

The Au-CSRG response was modeled using FDTD method. The transmission of the SPR conversion and the near-field distribution were analyzed by changing the RI of the dielectric medium in contact with the metallic crossed gratings. The RIs used in the simulations for the azobenzene and gold were obtained from the literature.[36,37] The topography of a CSRG was modeled according to the following function:

$$f(x,y) = A\left\{\cos\left[\left(\frac{2\pi}{p}\right)\mathrm{x}\right] + \cos\left[\left(\frac{2\pi}{p}\right)\mathrm{y}\right]\right\} \tag{5.1}$$

where A and p correspond to the amplitude and period of the structure respectively, in accordance with the AFM characterization. The spectral transmission and the electric field intensity distribution, normalized with respect to the incident plane wave $|\mathrm{E}/E_0|^2$, were calculated for a single crest of the nanostructure equivalent to one period. Periodic boundary conditions in both x and y directions and a perfectly matched layer (PML) in the z-direction were used for the analysis region. A uniform mesh size of 3 nm was used for the envelope of the nanostructure, comprising the azobenzene layer, the gold film, and the dielectric medium, in all the directional axes. A plane wave polarized along the y-axis and orthogonal to the x-y plane was employed to induce an SPR in the structure.

5.2.5 Bulk RI sensing test

A 2 mm-thick, 2 cm x 2 cm polydimethylsiloxane (PDMS, Sylgard 184, Dow Corning, USA) chamber with an 8 mm x 8 mm center hole was fabricated by standard methods described in a previous work.[38] The square chamber containing the different RI solutions was positioned atop the gold substrate to maintain the solutions in contact with the CSRG. Aqueous sucrose solutions (0%, 5%, 10%, 15%, and 20% w/v) were used to test the response of the CSRG to bulk refractive index changes. The refractive indices of the solutions were measured using an Abbe refractometer (Shanghai Optical Instruments, China). The transmitted images for each solution were recorded with the CMOS detector and further analyzed via *Fiji* image processing software.

5.2.6 Bacterial detection

Before the bacterial immobilization, the surface of the CSRG was cleaned with consecutive rinses of aqueous acetone solution (10% v/v) and deionized water. Once the surface was dry, the test solution was dispensed and contained by a PDMS well atop the CSRG surface. Subsequently, phosphate-buffered saline (PBS) solution was introduced to the chamber. The transmission signal due to the PBS refractive index served as the baseline signal for the consecutive measurements. Next, a UPEC-specific antibody solution was introduced onto the surface of the CSRG. This step promoted non-specific physisorption of the Ab on the surface, which is a method commonly used for the detection of analytes in SPR-based sensing[39–41] The corresponding change in intensity, caused by the SPR red-shifting, was monitored for 15 min. The surface was gently rinsed with PBS solution to flush the unbound antibodies. Thereafter, the solution of bacteria in PBS was introduced to the chamber, and the intensity change was acquired in real-time for 15 min. LED was intensity-controlled and synchronized to the CMOS capture by the Raspberry Pi unit to avoid evaporation of the solution during the experiments.

5.2.7 Bacterial culture

Bacteria *E. coli* O6:H1 (strain CFT073 / ATCC 700928 / UPEC), Klebsiella pneumonia, Pseudomonas aeruginosa, and Proteus mirabilis were routinely grown at 37 °C in Luria-Bertani (LB) medium. Overnight cultures resulted in a bacterial concentration of 10^9 CFU/mL.

5.2.8 Antibody production

Polyclonal rabbit antiserum to *E. coli* was prepared by immunization with cell envelopes. Strain CFT073 was grown overnight at 37 °C in M9 defined culture medium (Na2HPO4 (42 mM), KH2PO4 (22 mM), NaCl (9 mM), NH4Cl (18 mM), MgSO4 (1 mM), CaCl2 (0.1 mM) and glucose (0.2% w/v)),[42] supplemented with Peptone (0.5 g/L). The bacterial pellet was resuspended in Tris-HCl (50 mM), EDTA (5 mM, pH 7.5) containing protease inhibitor cocktail (Roche, Switzerland) and disrupted by ultrasonication with two 40 s pulses at low-power output, each followed by a 2-min pause, using a high-intensity ultrasonic processor (50-Watt Model, Sonics Materials Inc. Danbury, CT), unbroken cells were removed by centrifugation (12,000 x g for 10 min, 4 °C). Cell envelopes were collected by ultracentrifugation (50,000 x g for 30 min, 4 °C) and dissolved in PBS (pH 7.4). The envelope solution was injected subcutaneously (in multiple sites, 0.5 mg without any adjuvant) into rabbits. The animals were boosted 3 and 6 weeks later with the same membrane solution. Blood was collected from the central auricular vein of each ear 15 days later.

5.2.9 Human urine preparation

Human urine was collected from healthy individuals who had no history of UTI. Informed consent was obtained from all human subjects. The fresh urine was pooled and filtered with a 0.22-μm-pore-size, stored at 4 °C and used within the next 1 to 3 days.

5.2.10 Dot-blot immunoassay

The immunoassay was performed as per the methods described by Harlow and Lane, 1988 but with some modifications.[43] A 3 μl volume for each bacterial suspension (10^5 CFU/ml in PBS) were spotted on a nitrocellulose membrane. The spots were allowed to dry. The membrane was subsequently blocked using a blocking solution comprising of 5% wt/vol non-fat dry milk, 0.2% Tween 20 and 0.02% sodium azide in PBS for 1 hr under agitation. The membrane was then washed with PBS solution containing 0.2% Tween 20 and incubated for 2 hr with 1:100 dilution of the rabbit antibodies against *E. coli*. After the incubation, the membrane was washed thrice with PBS solution and incubated with a 1:5000 dilution of horseradish peroxidase-conjugated anti-rabbit IgG. 4-chloro-1-naphthol was added onto the membrane to visualize the binding reaction.

5.3. Results and discussion

5.3.1 Crossed surface relief gratings (CSRGs)

A CSRG consists of two perpendicularly superimposed SRGs. The relation for SPs excitation along the surface of a SRG is $k_{sp} = k_0 n\sqrt{(\varepsilon_m \varepsilon_d / \varepsilon_m + \varepsilon_d)}$, where k_{sp} is the surface plasmon wave number, k_0 is the free-space wave number, and ε_m and ε_d are the permittivities of the metallic and dielectric materials respectively. Once SPR conditions are achieved in one of the gratings, followed by a simultaneous re-radiation of the plasmonic energy by its orthogonal counterpart in the orthogonal light polarization. As a result, when placed between crossed polarizers, the orthogonally-superimposed gratings allow for the transmission of only the SPR signal while eliminating all the incident light wavelengths other than that of the SPR – a distinctive plasmonic characteristic of CSRGs.[17] Resonant excitation of surface plasmons (i.e. photon-to-electron coupling) at a metal-dielectric surface requires energy and momentum matching between the incident light and the SPP. For a single gold-coated SRG configuration and assuming almost flat interfaces, the grating equation can be used to find the phase-matching condition:

$$k_{sp} = k_0 n \sin\theta \pm 2\pi m/\Lambda \tag{5.2}$$

where θ is the incidence angle, m is the diffraction order (normally limited to unity) and Λ is the grating pitch. In addition to equation (5.2), SPR a diffraction grating using requires the incident light polarization to be along the grating vector. At normal incidence, the wave number can be further simplified to $k_{sp} = 2\pi/\lambda_{sp}$, and the light wavelength at which SP excitation occurs is given by:

$$\lambda_{spr} = n\Lambda\sqrt{\varepsilon_m/(n^2+\varepsilon_m)} \tag{5.3}$$

For a CSRG, the individual SRG diffraction characteristics are retained, enabling the use of equations (5.2) and (5.3) to identify an SPR peak wavelength prior to the fabrication of the grating [17]. Controlling the fabrication parameters, such as the laser irradiance, exposure time and the incidence angle of the laser on the Lloyd mirror, CSRGs can be fabricated with high precision without employing expensive and time-consuming clean-room techniques.

A design SRG pitch of 450 nm was selected to achieve a theoretical λ_{spr} of 648 nm, using equation (5.3**)**. This wavelength was chosen since it is within the region where the azobenzene thin films are almost transparent (above 600 nm), but it is also close to the peak wavelength (626 nm) of the red LED used in the experiments. Even though the equations above predict only one SPR wavelength to be excited using a particular grating, practically, a narrow band of wavelengths is excited near the SPR wavelength due to dispersion. For that reason, the selected grating pitch was chosen so that the peak wavelength of the red LED falls on the steepest slope of the SPR spectrum to enable maximum sensitivity to change in the refractive index of the dielectric medium.

It was previously found that the intensity of the plasmonic resonance depends on the grating modulation depth.[34] The thickness of the azobenzene film was therefore optimized, considering experimental limitations, to obtain CSRG with the narrowest and strongest SPR signal. Azo-glass solution was spin-coated at 3 different RPMs (800, 1000 and 1200) on a pre-cleaned 2.5 cm × 2.5 cm microscopic glass slide and Au-CSRGs were fabricated on these samples using the fabrication method described in Section 5.2.1. The corresponding plasmonic signal from each sample was obtained with the spectral interrogation setup, as described in Section 5.2.3 Figure 5.1a shows the SPR signal obtained from each sample, keeping water as the dielectric medium above the CSRG. As evident from plots, Au-CSRG fabricated on azo-glass spin-coated samples at 1000 RPM provided with the strongest (intensity ~ 8000 a.u.) and narrowest signal (FWHM ~ 38 nm). The AFM was usd to measure the topography of the CSRG surface. The depth and pitch of the CSRG, measured with the AFM analysis tool, were c.a. 75 nm and 450 nm, respectively. An image obtained through the AFM tool is shown in Figure 5.1b. The orientation of the AFM image is meant to assist the visualization of the unique two-dimensional periodicity of the surface.

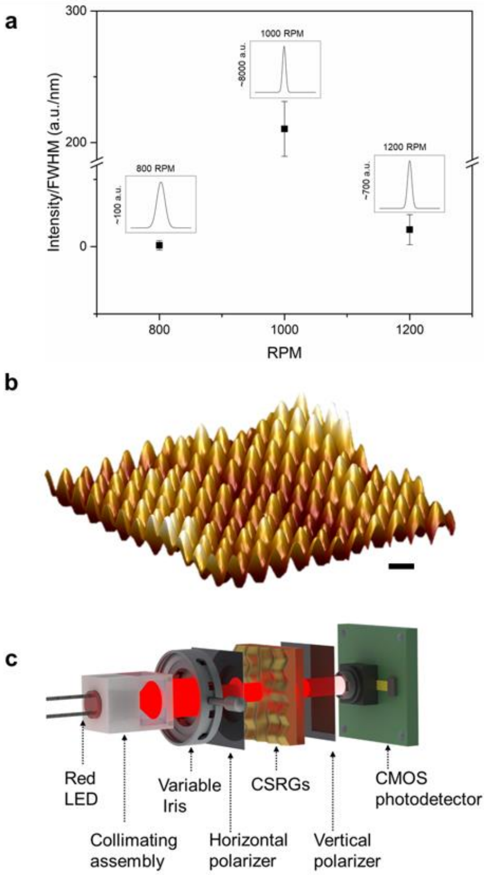

Figure 5.1 a) Signal quality (Intensity/FWHM) for transmitted SPR signal acquired from metallic CSRG fabricated on azo-glass thin film spin-coated on glass slides at different RPMs (800, 1000 and 1200). The dielectric medium in contact with the metallic CSRG was water (RI = 1.330). Error bars represent the standard deviation (n = 3). b) AFM scan of the CSRG (scan area = 5 µm × 5 µm) displaying the surface topography (pitch = 450 nm, depth c.a. 75 nm). Scale bar represents 500 nm. c) Schematic of the optical assembly for SPRi measurements.

5.3.2 Optical characterization

CSRG-based SPRi sensing is achieved by measuring the changes in the transmitted light intensity associated with the spectral shift that results from the near-field refractive index change at the liquid-metal interface. The changes in light intensity are continuously monitored and captured via a CMOS photodetector. Figure 5.1c shows a schematic representation of the platform employed in this work. Collimated light from a 3D printed assembly is first directed towards a horizontally aligned polarizer, and then onto the CSRG. The LED used in the platform was selected to have peak intensity in the wavelength range from 600 - 650 nm, which is a linear region in the transmission spectrum of the CSRG using a halogen lamp for different refractive index (RI) solutions, as previously reported elsewhere.[20] Considering equation (5.3), it is expected that an increase in the near-field RI results in a red-shift in the transmitted SPR spectrum, which is translated to a decrease in the transmitted light intensity of the image acquired by the CMOS photodetector. FDTD simulations were used to verify the electric field enhancement due to SPR excitation at the surface of the CSRG, considering the fabrication design parameters. Figure 5.2a shows the isometric view of the simulation environment with the grating structures and the dielectric medium above the CSRG. Figure 5.2b shows the electric field enhancement enabled by the CSRG using normally incident p-polarized light. In contrast with a plain gold surface, also shown in Figure 5.2b, the CSRG facilitates an electric field intensity enhancement of ~30 times at the metal-dielectric interface. This enhancement produces a highly sensitive interface to changes in the local RI, as observed in the simulation results of Figure 5.2c. Since CSRGs have a complex 3D surface, simulations were performed using a surface fit function (details provided in Section 5.2.4) to closely emulate the CSRG's surface topography. Due to the slight topographic difference between the surface fit and the actual CSRG, a light source with a wavelength of 613 nm was used for the electric field distribution in the FDTD simulations. The approximation is suitable, considering the FWHM of the red LED light source used in the experimental work is ~16 nm (λ_{peak} = 626 nm).

In biosensing, sensitivity is a critical performance indicator of a sensor and its ability to resolve minute differences in concentration upon analyte recognition. Sensitivity measurements with CSRGs depends on the relative intensity changes in the transmitted light intensity, using a reference measurement as base intensity value. As first control, we performed a total of four independent experiments for the signal acquisition of the transmitted light intensity using PBS solution. The signal was acquired at one-minute intervals (n = 8) for the four experiments. As shown in Figure 5.2d, the variation of the relative intensity was less than 0.1 a.u., which in negligible when compared intensity differences for changes in local RI. Once the stability of the base PBS solution signal was known, the sensitivity of the CSRG-based SPRi platform was determined using aqueous sucrose solutions with different concentrations (c.a. 0%, 5%, 10%, 15% and 20%, w/v) and known respective RIs of 1.330, 1.337, 1.344, 1.351 and 1.357. A thin 2 cm × 2 cm PDMS chamber with an 8 mm × 8 mm opening was placed on top of the CSRG for housing the test solutions and allowing for the liquid-metal contact. The chamber contained approximately ~140 µL of the solutions and was covered with a glass cover slip to eliminate lensing effects. The transmitted images for each solution were acquired, and subsequently processed via the Fiji image processing software. The mean image intensity values of the transmitted images for each of the above-mentioned solutions are plotted against their respective RIs in Figure 5.2e. The negative slope of the linear fit aligns with the red shift expected with the increase in the refractive index of the test solution. The numerical value of the slope is the bulk sensitivity of the platform, and it is found to be 613.45 Pixel Intensity Unit (PIU)/ Refractive Index Unit (RIU). This is almost a 3-fold improvement over the bulk sensitivity of SPRi platforms reported elsewhere.[28,44] It should also be noted that only off-the-shelf, relatively inexpensive optical and electronic components were used, thus lowering the overall cost of the platform significantly. Based on the bulk sensitivity and a repeatability of 10^{-3} PIU, the resolution of the platform is in the order of 10^{-6} RIU.[45] The signal-to-noise ratio (SNR) for the system, was calculated following the standard methods previously reported in the literature.[46,47] SNR was calculated using the equation $SNR_{dB} = 10*\log_{10}(\mu_{signal}/\sigma_{background})$, where μ_{signal} and $\sigma_{background}$ correspond to the average intensity of the transmitted signal and the standard deviation of the background noise, respectively. The resulting SNR for the metallic CSRGs-based platform is ~33 dB, a value comparable to other reported SNR optimization methods for SPR systems.[48] We postulate the high SNR achieved by the CSRG-based SPRi platform is due to the elimination of residual light by cross-polarization.

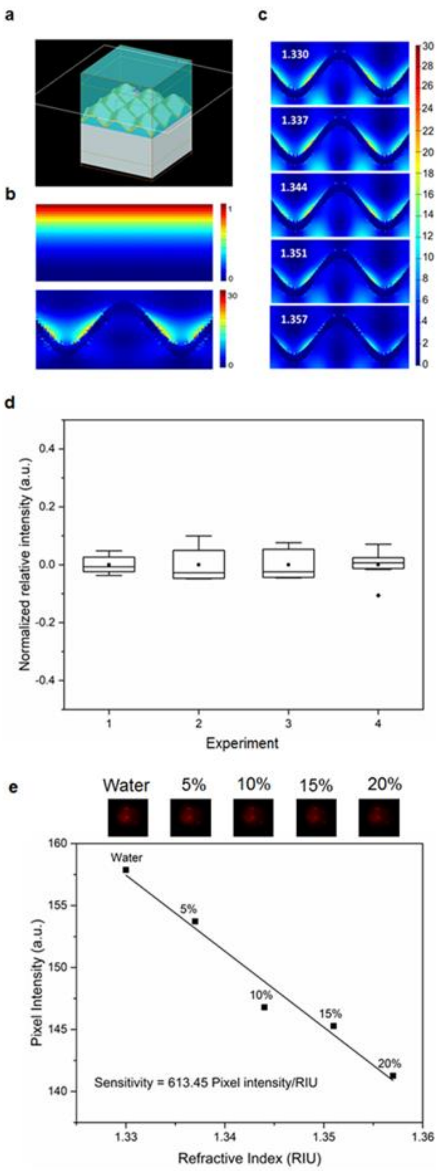

Figure 5.2 FDTD simulations and control experiments using PBS and changes in bulk RI. a) Isometric view of the simulation environment. b) Simulated electric field enhancement $|\boldsymbol{E}/\boldsymbol{E_0}|^2$ for : (Top) plain gold surface (Bottom) CSRG for air (RI = 1) as the dielectric medium. White scale bar = 100 nm. c) Top-bottom represents simulated electric field enhancement $|\mathbf{E}/\boldsymbol{E_0}|^2$ for CSRG at $\lambda = 613$ nm for increasing refractive indices (RI = 1.330 to 1.357). d) Relative intensity variation of the acquired signal using PBS solution as control, for four independent measurements (n = 8). e) Experimental bulk refractive index sensing plot representing the data points for transmitted intensity vs. the refractive indices of the test solutions. Actual acquired images are shown as inset. The slope of the linear fit represents the sensitivity of the platform, with a value of ~ 613 pixel intensity/RIU. Error bars (n = 3) are smaller than the size of the symbol representing the mean in the graph.

5.3.3 Quantitative detection of uropathogenic E. coli via CSRG-based SPRi

Real-time detection of near-surface RI changes is an important utility of CSRGs-based biosensing platform, which can be translated for real-world applications, such as in situ UTI diagnosis in complex biological matrices. UTI affects people from all demographics, with millions of cases reported each year and the primary culprit (>85 % cases) is UPEC.[49] The SPRi platform employing nanofabricated CSRGs, with high sensitivity, allows for the quantification and precise detection of biomolecular assembly bound on the surface of the CSRG. Moving towards this goal, we employed the platform for the quick, label-free and cost-effective detection of whole bacterium UPEC. First, the surface of the CSRG was functionalized with UPEC-specific antibodies which bind to the outer membrane of the bacteria by anchoring to proteins, phospholipids, and oligosaccharides on the cell's surface.[50] Figure 5.3a shows the relative intensity shift observed for both, the surface modification with antibodies (t = 1 min to 16 min), and for the detection of UPEC (t > 16 min). The relative shift is calculated in relation to the baseline light intensity observed for pure PBS solution over the sensor at t = 0 min. The surface modification of the sensor via incubation of UPEC-specific antibodies for 15 min was monitored, in real-time, via the change in transmitted light intensity corresponding to the shift in the plasmonic peak towards longer wavelengths. The surface of the CSRG was then gently rinsed with PBS solution, which left the amplitude of the intensity of the signal unaltered, confirming the near-surface modification with the Ab. Subsequently, 140 µL of 10^9 CFU/mL UPEC was added to the sensor surface and the transmitted light intensity was acquired at one-min intervals for 15 min. The relative shift corresponding to the immobilization of the antibodies on the surface of the sensor and the subsequent binding of UPEC to the antibodies was 3.384 a.u. and 4.795 a.u., which corresponds to an intensity change that is comparable with similar techniques reported previously.[28] Also, as a negative control experiment, the biosensing platform was tested for the detection of *Klebsiella pneumonia*, *Pseudomonas aeruginosa* and *Proteus mirabilis* at a concentration of 10^9 CFU/mL, to assess the selectivity of the functionalized surface of the sensor. No significant intensity change (mean relative intensity shift for K. pneumonia = 0.038 a.u., Proteus mirabilis = 0.012 a.u. and P. aeruginosa = 0.017 a.u.) was observed for the non-specific bacteria runs, confirming the high specificity for UPEC detection (Figure 5.3b). A dot-blot immunoassay was used to confirm the specificity of the antibody towards UPEC, and the non-specific binding of the abovementioned gram-negative bacteria, as shown in Figure 5.3b (inset).

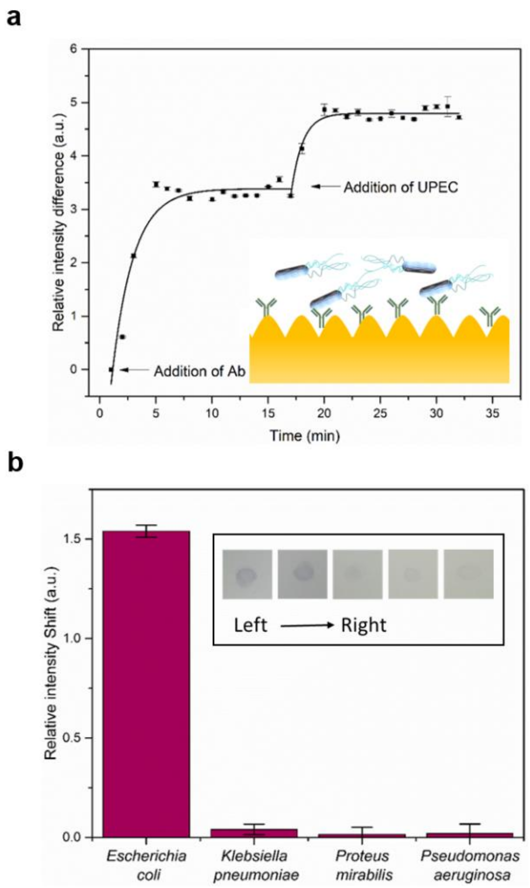

Figure 5.3 Quantification and evaluation of selective UPEC capture and detection. a) Plot represents the real-time binding of the UPEC-specific antibody (t = 1 min to 16 min) and UPEC at 10^9 CFU/mL in PBS (t > 16 min) via corresponding shift in pixel intensity observed over time. Error bars represent the standard deviation (n=3). (inset) Schematic depiction of the biodetection scheme, where bacteria are captured by immobilized antibodies on the CSRG surface. b) Relative transmitted light intensity change for *Klebsiella pneumonia*, *Proteus mirabilis* and *Pseudomonas aeruginosa*, in comparison to UPEC. The experiments were conducted using the same bacterial concentration and procedure of detection in all cases. Error bars represent standard deviation (n = 3). (Inset) Dot-blot affinity immunoassay of anti-*E. coli* antibody

for Gram-negative bacteria. From left to right: positive control, uropathogenic *E. coli* (UPEC), *Klebsiella pneumonia, Pseudomonas aeruginosa* and *Proteus mirabilis*."

The LOD of the CSRG-based platform was calculated based on the definition by the International Union of Pure and Applied Chemistry (IUPAC), as the blank signal plus three times the value of the standard deviation.[51] The calculated LOD is 0.03 a.u., based on the linear fit line for the different concentrations of the bacteria, we attributed the bacterial concentration to give 0.03 a.u. shift as the LOD of our platform (~100 CFU/mL). In order to relate the LOD with bacterial concentration, we employed a dose-based binding study was performed using bacterial concentration spanning 6-orders of magnitude, from 10^3 CFU/mL to 10^9 CFU/mL. Figure 5.4 shows the relative shift associated with the detection of different concentrations (10^3, 10^5, 10^7, 10^9 CFU/mL) of UPEC, on antibody-functionalized CSRG surface. The intensity shift varies linearly with the logarithmic concentration of bacteria with a 0.9 regression coefficient. Based on the signal for the antibody functionalization before the addition of bacteria and the standard deviation of the acquired signal, the LOD of the system is in the order of 100 CFU/mL.[52] The LOD value for UPEC detection by the CSRG-based SPRi platform is comparable to the values reported in the literature.[53] It is important to note that the lowest concentration detectable by the sensing platform presented here is well below the clinical threshold of UPEC (~10^5 CFU/mL) for UTI diagnosis in clinical samples.[49,54] Additionally, the platform is able to detect the whole bacterium, as opposed to genome sequence-based methods which are costly and time-consuming, using inexpensive, off-the-shelf electronic and optical components. Furthermore, to emulate a real-world scenario, and to validate the platform as a viable POC testing device, UPEC detection procedure was carried out in a complex biological matrix as opposed to laboratory standard PBS solution. In clinical settings, UTI detection is carried out by culturing the bacteria from patient urine samples to diagnose the infection. The SPRi platform presented here provides a fast, cost-effective alternative to the clinical method, which is demonstrated by employing the platform for real-time detection in healthy human urine spiked with UPEC bacteria. Human urine samples collected from healthy individuals with no history of UTI were spiked with UPEC to prepare bacterial solutions with concentrations of 10^5 and 10^7 CFU/mL. UPEC-specific antibodies were incubated on the CSRG surface using the experimental procedure outlined above. The spiked human urine samples were then incubated on the surface of the sensor for 15 min, and the transmitted light was acquired via the CMOS detector. The relative shift observed for the spiked human urine samples is denoted in Figure 5.4 by red stars, demonstrating the detection of whole bacteria in complex biological matrices, such as human urine. The relative intensity shift observed for both, the urine and the PBS samples spiked with UPEC (10^5 and 10^7 CFU/mL), is almost similar, which demonstrates the high selectivity of the platform for UPEC detection.

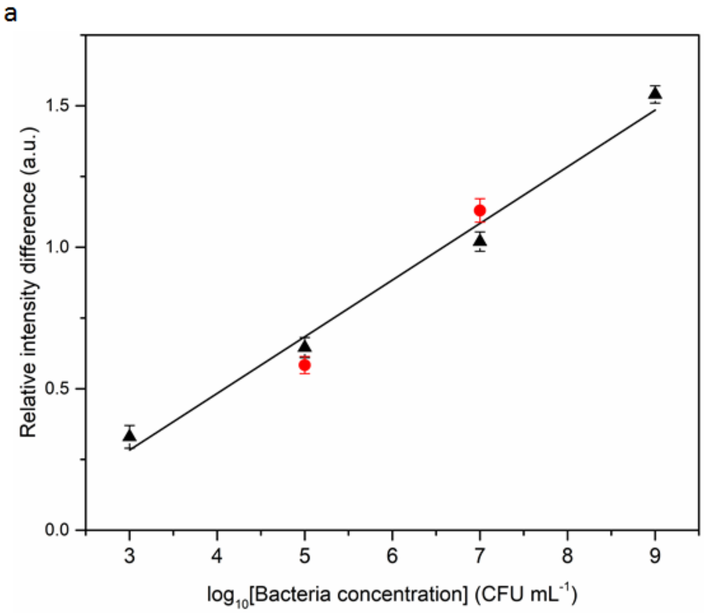

Figure 5.4 Standard calibration curve for selective detection of UPEC for concentrations ranging from 10^3 to 10^9 CFU/mL. Signals are obtained by flowing UPEC suspensions in both PBS (black triangle) and human urine (red circles) at different concentrations over UPEC-specific antibodies immobilized on the CSRG surface. Some of the error bars (n = 3) are comparable to the size of the symbol representing the mean.

5.4 Conclusions

This work presents the first demonstration of SPRi-based biosensing enabled by metallic CSRGs. The imaging platform employs nanoplasmonic two-dimensional gratings that promote a unique plasmonic energy transfer between the metallic nanostructures, and inexpensive, off-the-shelf optical and electronic components. The miniaturized biosensing platform is fully integrated within a total envelope of 2.5 cm × 2.5 cm × 10 cm. FDTD simulations demonstrate a 30-fold electric field intensity enhancement at the surface of Au-CSRG, compared to a flat gold surface. The experimental sensitivity and resolution of the platform are ~ 600 PIU/RIU and 10^{-6} RIU, respectively with an SNR of ~33 dB. The platform was developed using 3D-printed holders and aligners with inexpensive LED and CMOS systems (~ US$100), in contrast with other SPRi platforms reported in the literature, which involve bulky microscope assemblies and expensive CCD arrays. We also demonstrate the platform's capability to perform real-time detection of UPEC for bacterial suspensions in PBS solution and human urine, for concentrations ranging from 10^3 to 10^9 CFU/mL. In contrast to clinical detection timelines, the complete detection of UPEC at a clinically relevant concentration of 10^5 CFU/mL was completed in 35 min. The platform has a dynamic range spanning 6-orders of magnitude with a LOD of ~100 CFU/mL, which is a value below the threshold for UTI diagnosis (~10^5 CFU/mL) in clinical practice. The UPEC selectivity of the platform was experimentally verified by assessing non-specific binding to UPEC antibodies of other UTI-causing gram-negative bacteria. In contrast to traditional genome amplification-based approaches, the presented platform enables whole-bacterium detection in human urine (i.e. a complex matrix) which significantly reduces the overall cost and operator labor. In addition, this platform could be coupled with the cameras in portable electronic devices, such as smartphones, making it practical to use outside the clinical laboratory.

5.5 References

(1) Brolo, A. G. Plasmonics for Future Biosensors. Nat. Photonics 2012, 6 (11), 709–713. https://doi.org/10.1038/nphoton.2012.266.

(2) Canalejas-Tejero, V.; Herranz, S.; Bellingham, A.; Moreno-Bondi, M. C.; Barrios, C. A. Passivated Aluminum Nanohole Arrays for Label-Free Biosensing Applications. ACS Appl. Mater. Interfaces 2014, 6 (2), 1005–1010. https://doi.org/10.1021/am404509f.

(3) Couture, M.; Brulé, T.; Laing, S.; Cui, W.; Sarkar, M.; Charron, B.; Faulds, K.; Peng, W.; Canva, M.; Masson, J.-F. High Figure of Merit (FOM) of Bragg Modes in Au-Coated Nanodisk Arrays for Plasmonic Sensing. Small 2017, 13 (38), 1700908. https://doi.org/10.1002/smll.201700908.

(4) Eftekhari, F.; Escobedo, C.; Ferreira, J.; Duan, X.; Girotto, E. M.; Brolo, A. G.; Gordon, R.; Sinton, D. Nanoholes As Nanochannels: Flow-through Plasmonic Sensing. Anal. Chem. 2009, 81 (11), 4308–4311. https://doi.org/10.1021/ac900221y.

(5) Escobedo, C.; Chou, Y.-W.; Rahman, M.; Duan, X.; Gordon, R.; Sinton, D.; Brolo, A. G.; Ferreira, J. Quantification of Ovarian Cancer Markers with Integrated Microfluidic Concentration Gradient and Imaging Nanohole Surface Plasmon Resonance. Analyst 2013, 138 (5), 1450. https://doi.org/10.1039/c3an36616b.

(6) Li, X.; Soler, M.; Szydzik, C.; Khoshmanesh, K.; Schmidt, J.; Coukos, G.; Mitchell, A.; Altug, H. Label-Free Optofluidic Nanobiosensor Enables Real-Time Analysis of Single-Cell Cytokine Secretion. Small 2018, 14 (26), 1800698. https://doi.org/10.1002/smll.201800698.

(7) López-Muñoz, G. A.; Estevez, M.-C.; Peláez-Gutierrez, E. C.; Homs-Corbera, A.; García-Hernandez, M. C.; Imbaud, J. I.; Lechuga, L. M. A Label-Free Nanostructured Plasmonic Biosensor Based on Blu-Ray Discs with Integrated Microfluidics for Sensitive Biodetection. Biosens. Bioelectron. 2017, 96, 260–267. https://doi.org/10.1016/J.BIOS.2017.05.020.

(8) Soler, M.; Belushkin, A.; Cavallini, A.; Kebbi-Beghdadi, C.; Greub, G.; Altug, H. Multiplexed Nanoplasmonic Biosensor for One-Step Simultaneous Detection of Chlamydia Trachomatis and Neisseria Gonorrhoeae in Urine. Biosens. Bioelectron. 2017, 94, 560–567. https://doi.org/10.1016/j.bios.2017.03.047.

(9) Suutari, T.; Silen, T.; S¸en Karaman, D.; Saari, H.; Desai, D.; Kerkelä, E.; Laitinen, S.; Hanzlikova, M.; Rosenholm, J. M.; Yliperttula, M.; Viitala, T. Real-Time Label-Free Monitoring of Nanoparticle Cell Uptake. Small 2016, 12 (45), 6289–6300. https://doi.org/10.1002/smll.201601815.

(10) Urraca, J. L.; Barrios, C. A.; Canalejas-Tejero, V.; Orellana, G.; Moreno-Bondi, M. C. Molecular Recognition with Nanostructures Fabricated by Photopolymerization within Metallic Subwavelength Apertures. Nanoscale 2014, 6 (15), 8656–8663. https://doi.org/10.1039/c4nr01129e.

(11) Homola, J. Surface Plasmon Resonance Based Sensors; Springer Series on Chemical Sensors and Biosensors; Springer Berlin Heidelberg, 2006.

(12) Vala, M.; Chadt, K.; Piliarik, M.; Homola, J. High-Performance Compact SPR Sensor for Multi-Analyte Sensing. Sensors Actuators B Chem. 2010, 148 (2), 544–549. https://doi.org/10.1016/j.snb.2010.05.067.

(13) Bhatta, D.; Stadden, E.; Hashem, E.; Sparrow, I. J. G.; Emmerson, G. D. Multi-Purpose Optical Biosensors for Real-Time Detection of Bacteria, Viruses and Toxins. Sensors Actuators B Chem. 2010, 149 (1), 233–238. https://doi.org/10.1016/j.snb.2010.05.040.

(14) Yeh, W.-H.; Kleingartner, J.; Hillier, A. C. Wavelength Tunable Surface Plasmon Resonance-Enhanced Optical Transmission Through a Chirped Diffraction Grating. Anal. Chem. 2010, 82 (12), 4988–4993. https://doi.org/10.1021/ac100497w.

(15) Masson, J.-F. Surface Plasmon Resonance Clinical Biosensors for Medical Diagnostics. ACS Sensors 2017, 2 (1), 16–30. https://doi.org/10.1021/acssensors.6b00763.

(16) Ahmed, A.; Rushworth, J. V.; Hirst, N. A.; Millner, P. A. Biosensors for Whole-Cell Bacterial Detection. Clin. Microbiol. Rev. 2014, 27 (3), 631–646. https://doi.org/10.1128/CMR.00120-13.

(17) Nair, S.; Escobedo, C.; Sabat, R. G. Crossed Surface Relief Gratings as Nanoplasmonic Biosensors. ACS Sensors 2017, 2 (3), 379–385. https://doi.org/10.1021/acssensors.6b00696.

(18) Sabat, R. G.; Rochon, N.; Rochon, P. Dependence of Surface Plasmon Polarization Conversion on the Grating Pitch. J. Opt. Soc. Am. A 2010, 27 (3), 518. https://doi.org/10.1364/JOSAA.27.000518.

(19) Watts, R. A.; Harris, J. B.; Hibbins, A. P.; Preist, T. W.; Sambles, J. R. Optical Excitation of Surface Plasmon Polaritons on 90° and 60° Bi-Gratings. J. Mod. Opt. 1996, 43 (7), 1351–1360.

(20) Nair, S.; Gomez-Cruz, J.; Manjarrez-Hernandez, Á.; Ascanio, G.; Sabat, R.; Escobedo, C. Selective Uropathogenic E. Coli Detection Using Crossed Surface-Relief Gratings. Sensors 2018, 18 (11), 3634. https://doi.org/10.3390/s18113634.

(21) Wong, C. L.; Olivo, M. Surface Plasmon Resonance Imaging Sensors: A Review. Plasmonics 2014, 9 (4), 809–824. https://doi.org/10.1007/s11468-013-9662-3.

(22) Lesuffleur, A.; Im, H.; Lindquist, N. C.; Lim, K. S.; Oh, S.-H. Laser-Illuminated Nanohole Arrays for Multiplex Plasmonic Microarray Sensing. Opt. Express 2008, 16 (1), 219. https://doi.org/10.1364/OE.16.000219.

(23) Blanchard-Dionne, A.-P.; Guyot, L.; Patskovsky, S.; Gordon, R.; Meunier, M. Intensity Based Surface Plasmon Resonance Sensor Using a Nanohole Rectangular Array. Opt. Express 2011, 19 (16), 15041. https://doi.org/10.1364/OE.19.015041.

(24) Bocková, M.; Slabý, J.; Špringer, T.; Homola, J. Advances in Surface Plasmon Resonance Imaging and Microscopy and Their Biological Applications. Annu. Rev. Anal. Chem. 2019, 12 (1), 151–176. https://doi.org/10.1146/annurev-anchem-061318-115106.

(25) Coskun, A. F.; Cetin, A. E.; Galarreta, B. C.; Alvarez, D. A.; Altug, H.; Ozcan, A. Lensfree Optofluidic Plasmonic Sensor for Real-Time and Label-Free Monitoring of Molecular Binding Events over a Wide Field-of-View. Sci. Rep. 2015, 4 (1), 6789. https://doi.org/10.1038/srep06789.

(26) Cetin, A. E.; Coskun, A. F.; Galarreta, B. C.; Huang, M.; Herman, D.; Ozcan, A.; Altug, H. Handheld High-Throughput Plasmonic Biosensor Using Computational on-Chip Imaging. Light Sci. Appl. 2014, 3 (1), e122. https://doi.org/10.1038/lsa.2014.3.

(27) Forest, S.; Breault-Turcot, J.; Chaurand, P.; Masson, J.-F. Surface Plasmon Resonance Imaging-MALDI-TOF Imaging Mass Spectrometry of Thin Tissue Sections. Anal. Chem. 2016, 88 (4), 2072–2079. https://doi.org/10.1021/acs.analchem.5b03309.

(28) Gomez-Cruz, J.; Nair, S.; Manjarrez-Hernandez, A.; Gavilanes-Parra, S.; Ascanio, G.; Escobedo, C. Cost-Effective Flow-through Nanohole Array-Based Biosensing Platform for the Label-Free Detection of Uropathogenic E. Coli in Real Time. Biosens. Bioelectron. 2018, 106. https://doi.org/10.1016/j.bios.2018.01.055.

(29) Guner, H.; Ozgur, E.; Kokturk, G.; Celik, M.; Esen, E.; Topal, A. E.; Ayas, S.; Uludag, Y.; Elbuken, C.; Dana, A. A Smartphone Based Surface Plasmon Resonance Imaging (SPRi) Platform for on-Site Biodetection. Sensors Actuators B 2017, 239, 571–577. https://doi.org/10.1016/j.snb.2016.08.061.

(30) Peterson, A. W.; Halter, M.; Tona, A.; Plant, A. L. High Resolution Surface Plasmon Resonance Imaging for Single Cells. BMC Cell Biol. 2014, 15 (1), 35. https://doi.org/10.1186/1471-2121-15-35.

(31) Shpacovitch, V.; Temchura, V.; Matrosovich, M.; Hamacher, J.; Skolnik, J.; Libuschewski, P.; Siedhoff, D.; Weichert, F.; Marwedel, P.; Müller, H.; Überla, K.; Hergenröder, R.; Zybin, A. Application of Surface Plasmon Resonance Imaging Technique for the Detection of Single Spherical Biological Submicrometer Particles. Anal. Biochem. 2015, 486, 62–69. https://doi.org/10.1016/j.ab.2015.06.022.

(32) Bennani, O. R.; Al-Hujran, T. A.; Nunzi, J.-M.; Sabat, R. G.; Lebel, O. Surface Relief Grating Growth in Thin Films of Mexylaminotriazine-Functionalized Glass-Forming Azobenzene Derivatives. New J. Chem. 2015, 39 (12), 9162–9170. https://doi.org/10.1039/C5NJ01299F.

(33) Rochon, P.; Batalla, E.; Natansohn, A. Optically Induced Surface Gratings on Azoaromatic Polymer Films. Appl. Phys. Lett. 1995, 66 (4), 136–138. https://doi.org/10.1063/1.107369.

(34) Monteiro, J. P.; Ferreira, J.; Sabat, R. G.; Rochon, P.; Santos, M. J. L.; Girotto, E. M. SPR Based Biosensor Using Surface Relief Grating in Transmission Mode. Sensors Actuators, B Chem. 2012, 174 (July 2015), 270–273. https://doi.org/10.1016/j.snb.2012.08.026.

(35) Bdour, Y.; Escobedo, C.; Sabat, R. G. Wavelength-Selective Plasmonic Sensor Based on Chirped-Pitch Crossed Surface Relief Gratings. Opt. Express 2019, 27 (6), 8429. https://doi.org/10.1364/oe.27.008429.

(36) Johnson, P. B.; Christy, R. W. Optical Constants of the Noble Metals. Phys. Rev. B 1972, 6 (12), 4370–4379. https://doi.org/10.1103/PhysRevB.6.4370.

(37) Mavrona, E.; Mailis, S.; Podoliak, N.; D'Alessandro, G.; Tabiryan, N.; Trapatseli, M.; Blach, J.-F.; Kaczmarek, M.; Apostolopoulos, V. Intrinsic and Photo-Induced Properties of High Refractive Index Azobenzene Based Thin Films [Invited]. Opt. Mater. Express 2018, 8 (2), 420. https://doi.org/10.1364/OME.8.000420.

(38) Duffy, D. C.; McDonald, J. C.; Schueller, O. J. A.; Whitesides, G. M. Rapid Prototyping of Microfluidic Systems in Poly(Dimethylsiloxane). Anal. Chem. 1998, 70 (23), 4974–4984. https://doi.org/10.1021/ac980656z.

(39) Beitollahi, H.; Tajik, S.; Alizadeh, R. Nano Composite System Based on Zno-Functionalized Graphene Oxide Nanosheets for Determination of Cabergoline. J. Electrochem. Sci. Technol. 2017, 8 (4), 307–313. https://doi.org/10.5229/JECST.2017.8.4.307.

(40) Zijlstra, P.; Paulo, P. M. R.; Orrit, M. Optical Detection of Single Non-Absorbing Molecules Using the Surface Plasmon Resonance of a Gold Nanorod. Nat. Nanotechnol. 2012, 7 (6), 379–382. https://doi.org/10.1038/nnano.2012.51.

(41) Dies, H.; Raveendran, J.; Escobedo, C.; Docoslis, A. In Situ Assembly of Active Surface-Enhanced Raman Scattering Substrates via Electric Field-Guided Growth of Dendritic Nanoparticle Structures. Nanoscale 2017, 9 (23), 7847–7857. https://doi.org/10.1039/C7NR01743J.

(42) Miller, J. H. Experiments in Molecular Genetics; Cold Spring Harbor Laboratory: New york, 1972.

(43) Harlow D., E. L. A Laboratory Manual; Cold Spring Harbor Laboratory, 1988. https://doi.org/10.1016/0968-0004(89)90307-1.

(44) Escobedo, C.; Vincent, S.; Choudhury, A. I. K.; Campbell, J.; Brolo, A. G.; Sinton, D.; Gordon, R. Integrated Nanohole Array Surface Plasmon Resonance Sensing Device Using a Dual-Wavelength Source. J. Micromechanics Microengineering 2011, 21 (11), 115001. https://doi.org/10.1088/0960-1317/21/11/115001.

(45) Hwang, G. M.; Pang, L.; Mullen, E. H.; Fainman, Y. Plasmonic Sensing of Biological Analytes Through Nanoholes. IEEE Sens. J. 2008, 8 (12), 2074–2079. https://doi.org/10.1109/JSEN.2008.2007663.

(46) Piliarik, M.; Vaisocherová, H.; Homola, J. Towards Parallelized Surface Plasmon Resonance Sensor Platform for Sensitive Detection of Oligonucleotides. Sensors Actuators B Chem. 2007, 121 (1), 187–193. https://doi.org/10.1016/J.SNB.2006.09.009.

(47) Nelson, B. P.; Grimsrud, T. E.; Liles, M. R.; Goodman, R. M.; Corn, R. M. Surface Plasmon Resonance Imaging Measurements of DNA and RNA Hybridization Adsorption onto DNA Microarrays. Anal. Chem. 2001, 73 (1), 1–7.

(48) Abumazwed, A.; Kubo, W.; Shen, C.; Tanaka, T.; Kirk, A. G. Projection Method for Improving Signal to Noise Ratio of Localized Surface Plasmon Resonance Biosensors. Biomed. Opt. Express 2017, 8 (1), 446.

(49) Grabe, M.; Bjerklund-Johansen, T. E.; Botto, H.; Cai, T.; Çek, M.; Köves, B.; Naber, K. G.; Pickard, R. S.; Tenke, P.; Wagenlehner, F. Guidelines on Urological Infections. Eur. Assoc. Urol. 2015, 14.

(50) Nikaido, H.; Vaara, M. Molecular Basis of Bacterial Outer Membrane Permeability. Microbiol. Rev. 1985, 49 (1), 1–32. https://doi.org/10.1128/MMBR.67.4.593-656.2003.

(51) IUPAC Compendium of Chemical Terminology the Gold Book., Version 1.0.0.; International Union of Pure and Applied Chemistry,: [Research Triangle Park, N.C.] :, 2006.

(52) Horwitz, W.; Lauwaars, M.; Sp, L.; Prof, S.; Vrije, M.; Brussel, U.; Prof, B.; Miller, J.; Nyeland, M. B.; Empa, R.; Gallen, S.; Prof, S.; Smeyers-Verbeke, J.; Suchanek, M.; Verplaetse, H.; Walsh, M.; Wegscheider, P. W.; Westwood, D.; Agency, E.; Mr, U.; Van De Wiel, H. J. The Fitness for Purpose of Analytical Methods; 1998; Vol. 1.

(53) Dudak, F. C.; Boyaci, I. H. Rapid and Label-Free Bacteria Detection by Surface Plasmon Resonance (SPR) Biosensors. Biotechnology Journal. John Wiley & Sons, Ltd July 2009, pp 1003–1011. https://doi.org/10.1002/biot.200800316.

(54) Flores-Mireles, A. L.; Walker, J. N.; Caparon, M.; Hultgren, S. J. Urinary Tract Infections: Epidemiology, Mechanisms of Infection and Treatment Options. Nat. Rev. Microbiol. 2015, 13 (5), 269–284. https://doi.org/10.1038/nrmicro3432.

Chapter 6

Structural stability of optofluidic nanostructures in flow-through operation

With minor changes to fulfill formatting requirements, this chapter is as it appears in: Yazan Bdour, Juan Gomez-Cruz and Carlos Escobedo. Micromachines 11 (4), 373.

Abstract: Optofluidic sensors based on periodic arrays of subwavelength apertures that support surface plasmon resonance can be employed as both optical sensors and nanofluidic structures. In flow-through operation, the nanoapertures experience pressures differences across the substrate in which they are fabricated, which imposes the risk for structural failure. This work presents an investigation of the deflection and structural stability of nanohole array based optofluidic sensors operating in flow-through mode. The analysis was approached using experiments, simulations via finite element method and established theoretical models. The results depict that certain areas of the sensor deflects under pressure, with some regions suffering of high mechanical stress. The offset in the deflection values between theoretical models and actual experimental values is overturned when only the effective area of the substrate, of 450 µm, is considered. Experimental, theoretical and simulation results suggest that the periodic nanostructures can safely operate under trans-membrane pressures of up to 20 psi, which induce deflections of up to ~20 µm.

6.1 Introduction

The development of new point-of-care (POC) diagnostic technologies require low-cost, fully integrated sensing platforms capable of providing quantitative results in situ. At the same time, POC diagnostic platforms have a tremendous potential that has yet to be fully exploited.

Telemedicine, for instance, aims to monitor the health of patients remotely through on-site sensing using personal devices, holding a global market of c.a. US$7 billion.[1] A trendy, and increasingly demanded approach to in situ sensing is the use of lab-on-a-chip platforms enabled by cell phones to record, analyze and transmit the results.[2–4] With the recent emergence of the new pathogens, such as the Coronavirus, and the Yaravirus, an on-site analysis will limit their health impact with a rapid sensing test, quantifying the severity of the infection, and assist with the quarantine measures.[5,6] Periodic arrays of subwavelength structures fabricated in metal films enable surface plasmon resonance (SPR), which has motivated their use as biosensors for several applications in different fields.[7–12] Ordered arrays of metallic nanoholes are optofludic structures that enable both, transport of fluid and analyte via nanofluidic confinement, and nanoplasmonic sensor. The plasmonic resonance signature obtained from nanohole arrays (NHAs) allow the detection of biologically relevant analytes in label-free fashion and real-time. Toward the development of POC biosensing platforms, these optofluidic nanostructures have been integrated into microfluidic environments in order to create fully-integrated sensors compatible with portable electronics.[13] NHA-based sensors are ideal for field applications due to their small footprint and integration abilities as evidenced by recent demonstrations for the detection of bacteria, such as Chlamydia trachomatis,[14] viruses, such as Ebola,[15] cancer biomarkers[16] and uropathogenic bacteria.[17] Flow-through optofluidic structures also enable the enrichment of analytes in liquids by an electrohydrodynamic effect occurring around the NHAs when an electric potential and a pressure bias are applied to the fluid in a closed system.[18] Despite their demonstrated potential in sensing, most applications involving nanohole arrays have been focused on exploiting the conventional optical capacities of these nanostructures. The mechanical stability of the nanohole membranes is an overlooked aspect of their properties that are key when functioning as nanofluidic structures. In analogy to porous silicon-based membranes, where permeability increases significantly as membrane thickness decreases, the volumetric flow across nanostructured optofluidic sensors increase with the open pore fraction.

However, plasmonic nanostructures built thin membranes may suffer from low mechanical stability which could limit, critically, their use as optofluidic flow-through sensors.[19–21] The membrane's mechanical properties change due to the change in the structural morphology of the porous membrane as it deflects under pressure. The stability decreases by a correction factor (1-P), where P is related to the porosity of the membrane.[22]

Recent studies demonstrate that through-nanoapertures fabricated in thin (~50 nm) gold-coated Si3N4 substrates offer additional fluidic abilities that can be used to target in-hole delivery of analytes when operated as optofluidic sensors.[23,24] However, flow-through operation results in transmem¬brane pressures that could potentially damage the rather brittle nanostructures. The mechanical properties of the organized nanohole arrays are not completely understood due to their sensitivity, brittleness and nano-sized structures. Here, we present a study on structural aspects of Au-on-nitride optofluidic nano-plasmonic sensors operating in flow-through fashion at flowrates compatible with biosensing applications.

6.2 Materials and Methods

6.2.1 Fabrication of periodic through subwavelength apertures

Through nanohole arrays were fabricated using focused ion beam (FIB) milling using 100 nm thick Si3N4 free-standing membranes (Norcada, Edmonton, AB, Canada) coated with a thermally evaporated 100 nm layer of gold via a 5 nm chromium adhesion layer. Milling was achieved using a gallium ion beam set at 40 keV with a beam current of ~ 30 pA, with a typical beam spot size of 10 nm, and the dwell time of the beam at one pixel was set to 20 µs. Two arrays of through nanohole arrays with an area of 20 µm by 20 µm, diameter of c.a. 230 nm and pitch of 560 nm were fabricated.

6.2.2 Fabrication of microfluidic chips

The microfluidic chip was fabricated using a replica molding technique as described in detail elsewhere.[25] The general steps of the fabrication procedure are briefly described next. A mask with the microfluidic pattern was generated using SolidWorks CAD software. The design included one inlet and one outlet of 1.5 mm, and a 5-mm-wide channel with 100 μm in height. A master was fabricated by spin-coating SU-8 100 photoresist (MicroChem Corp., Newton, MA) on a clean 3-inch silicon wafer (Silicon Quest International Inc., Santa Clara, CA). The coated wafer was then prebaked for one minute at 65°C and for 10 minutes at 95°C. The mask with the channel pattern was then placed over the coated wafer and exposed to UV light for 90 seconds. Next, the exposed wafer was hard baked at 65 °C for 1 minute and at 95°C for 10 minutes. The master was subsequently developed using a SU-8 developer (MicroChem Corp., Newton, MA). A 12:1 mixture of Sylgard 184 elastomer to curing agent (Dow Corning, Midland, MI) was mixed, degassed in a vacuum and poured onto the master. After baking at 85°C for 20 minutes, the replica was removed from the mould. Inlets and outlets were provided one-mm punched holes for fluidic access. Microfluidic connections were achieved using polyetherether-ketone (PEEK) tubing (Upchurch Scientific, Oak Harbor, WA). A schematic representation of the setup is shown in Figure 6.1.

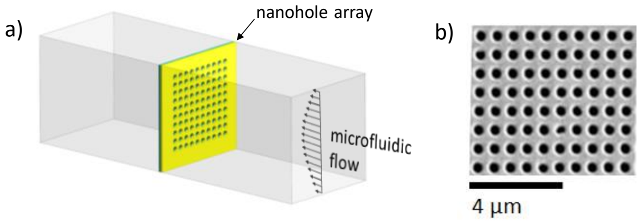

Figure 6.1 (a) SEM image of fabricated periodic subwavelength apertures via FIB. The nanostructures had 230 nm in diameter and 560 nm in pitch. (b) Schematic representation of a nanohole array in a microfluidic chip in flow-through operation.

6.2.3 Optofluidic Structure Deflection Analysis

Finite Element Analysis (FEA) was used as means to know the order of magnitude of the deflection and the mechanical stress that the optofluidic sensor may experience in flow-through operation. COMSOL Multiphysics (COMSOL, Sweden) was used to simulate a simplified model of the optofluidic sensor under a prescribed unidirectional and orthogonal pressure on one of the faces of the suspended membrane. The simulations were used first to estimate the order of magnitude of applied pressures that would result on the deflection of the substrate containing the optofluidic structures. This first model involved a stationary elastic model with default Lagrange-Quadratic element type. The finite element analysis solves for the displacement field at specific a specific point on the membrane for every input force. For the linear model, the system is governed by three tensor partial differential equations: $\nabla \cdot \sigma + F_v = 0$; $\varepsilon = \frac{1}{2}[(\nabla u)^T + \nabla u + (\nabla u)^T \nabla u]$; and $C = C(E, v)$, where, σ is the Cauchy stress tensor, F_v is the body force per unit, u, is the displacement vector, ε is the infinitesimal strain tensor, C is the fourth order stiffness tensor, E is the Young's modulus, v is the Poisson's ratio. A second static, nonlinear stress-strain model was used to compare the experimental data and to validate the deflection values obtained for the prescribed pressure range. The the nonlinear stress-strain behavior was achieved by using a power-law nonlinear elastic material model, accounting for geometric nonlinearities, which is governed by Ludwik's law: $\tau = \tau_0 + k\gamma^{1/n}$, where τ is the shear stress, γ is the shear strain and n is an integer.[26,27] User-controlled mesh with Lagrange-Quadratic element type was used for this nonlinear model, to guarantee an acceptable mesh size along the thickness of the modelled substrate. The finite element analysis solves for the displacement field at specific a specific point on the membrane for every input force. In both models, linear and nonlinear, the parameters of the Si_3N_4 were mainly used, as the values for the mechanical properties for this material supersede those of the metal components in the sensor, namely a Young's modulus of 250×10^9 Pa, a density of 3.1×10^3 kg/m^3 and a Poisson's ratio of 0.23. The surrounding surfaces around the membrane that corresponds to the areas that define the thickness of the substrate, were set as fixed boundaries. The transmembrane pressures were varied from 1 and 20 psi, as this range corresponds to flow rates in the order of nL/min, which are commonly used in biosensing applications. The deflection of the substrate and the stress (von Mises criterion) were recorded.

In addition to FEM based models, analytical models on the mechanical behaviour of perforated membranes published in the literature were also used to estimate the deflection of the optofluidic sensors in this study, as detailed in the Results and Discussion section.[22]

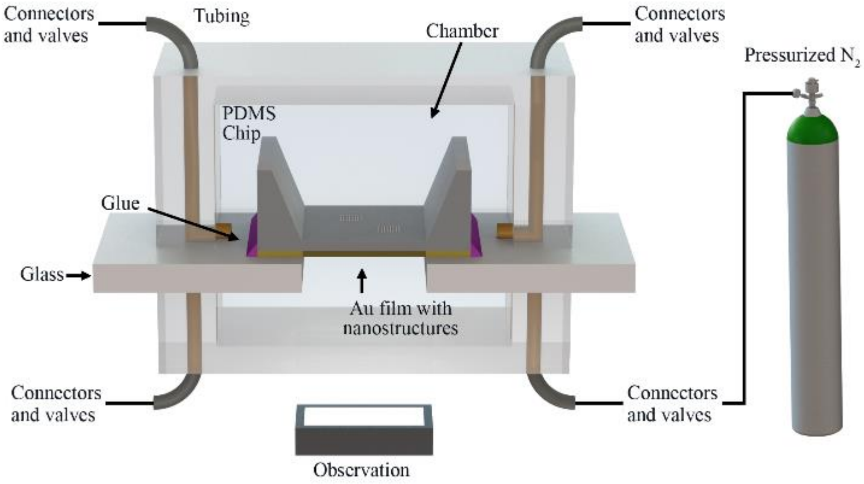

Figure 6.1 Schematic representation of the experimental setup.

6.3 Results and Discussion

Figure 6.3 shows the CAD models used to study the deflection of the optofluidic sensors via COMSOL Multiphysics software. Figure 6.3a shows the simplified model with a single nanoaperture at the center, used in the linear elastic material simulations. The model accounts for a 100-nm-thick membrane with a square surface with a side length of 500 μm, and a circular opening of 10 μm for surface coverage equivalency of the effective surface of the nano-apertures. Figure 6.3b shows an image of the CAD model used for the nonlinear simulations, a square 100-nm-thick membrane with side length of 500 μm and a 20 μm x 20 μm array of 230-nm-diameter holes with pitch-to-diameter ratio of 2. In both cases, linear and nonlinear models, the mesh curvature factor was 0.6, maximum element scaling factor of 1.9, resolution of narrow regions of

0.3 and the optimize quality feature was set to ON. The linear model had a maximum element size at all boundaries was 30×10^{-9}. The resulting mesh had ~210×10^3 domain elements with ~40×10^3 boundary elements and ~1.4×10^3 edge elements. The nonlinear model had ~1.4×10^4 domain elements, ~900×10^3 boundary elements and ~6×10^3 edge elements. The models were solved for pressures applied to the bottom surface of the substrate, for 1 psi and then using the sweep parameter feature for a pressure range of 2 to 20 psi with 2 psi pressure increments.

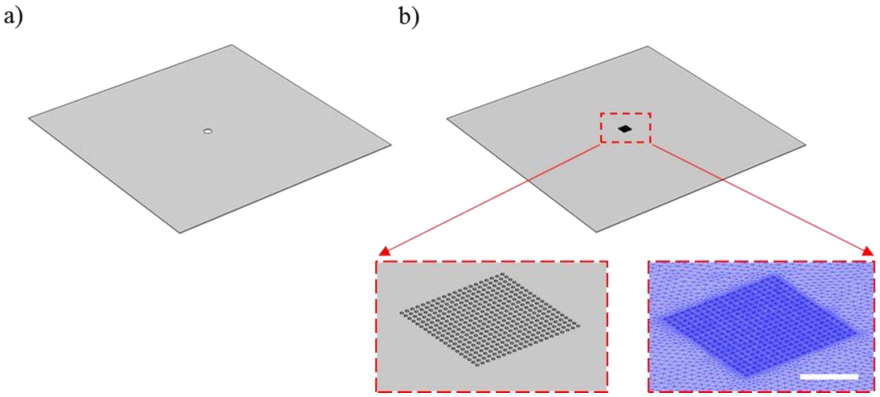

Figure 6.3 CAD models used for the FEM based simulations. (a) CAD model used for linear elastic simulations. (b) CAD model used for the nonlinear elastic simulations. A detail of the nanoapertures in the CAD model and the corresponding mesh are shown as insets. Scale bar represents 10 μm.

Figure 6.4 shows images of selected values for the deflection and stress distribution of the model of the membrane under an applied pressure of 20 psi. Figures 6.4a and 6.4b show the displacement in the z-direction for the linear and nonlinear models, respectively. The results are presented as non-deformed, with vectors representing the direction and magnitude of the deflection. The pattern of deflection observed from the simulations, as expected, is quasi-circular, with increasing magnitude towards the center of the free-standing membrane. The maximum deflection values, for the linear and nonlinear simulations at an applied pressure of 20 psi, were 24.08 and 19.39 μm, respectively. Maxima were always obtained at the apex of the deformed membrane. Figure 6.4c and 6.4d show the von Mises stress distribution for an applied pressure of 20 psi. The maximum stress found in the simulations was in the order of 1-10× 10^8 Pa, which suggests that the substrate which is housing the nanoapertures could well withstand the deformations resulting from the applied pressure. The simulation results were used to define a range of pressure that could be used experimentally, avoiding failure of the membrane.

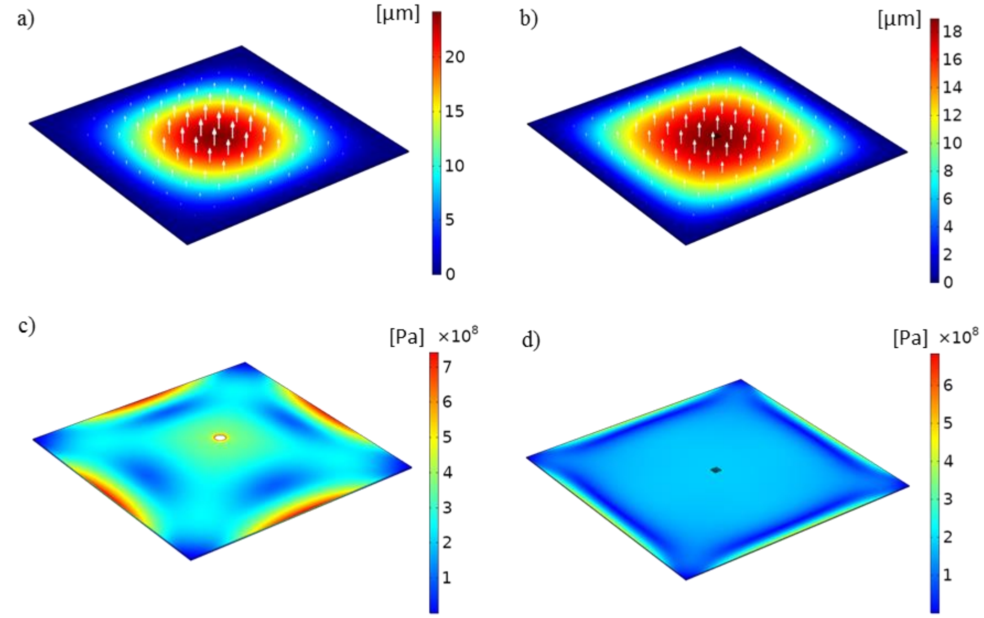

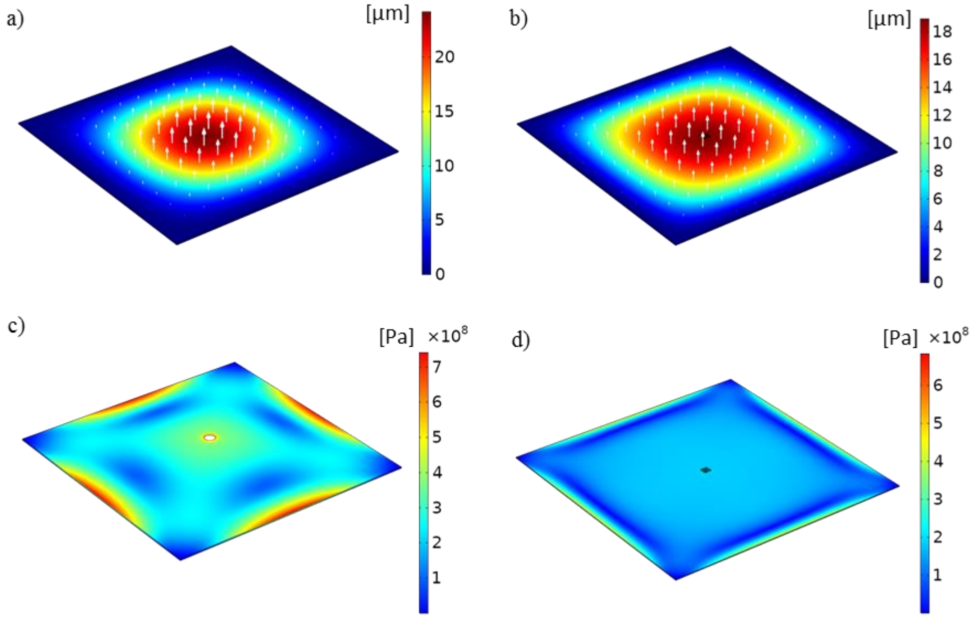

Figure 6.4 Simulation results of linear and nonlinear models. Membrane deflection under an applied pressure of 20 psi for (a) the linear model and (b) the nonlinear model. The apertures are shown in the insets within yellow dashed boxes

in both cases. Stress distribution (von Mises yield criterion) under an applied pressure of 20 psi for (c) the linear model and (d) the nonlinear model.

Figure 6.5 shows a bright field microscopy image of the Au-on-nitride membrane before and after the application of a pressure of 10 psi. The substrate included two rectangular periodic arrays of nanoapertures, indicated with yellow dashed lines. The boundaries of the Si3N4 membrane are indicated by red dashed lines. The focal plane in both images is the same, which indicates the deflection of the substrate under the applied pressure.

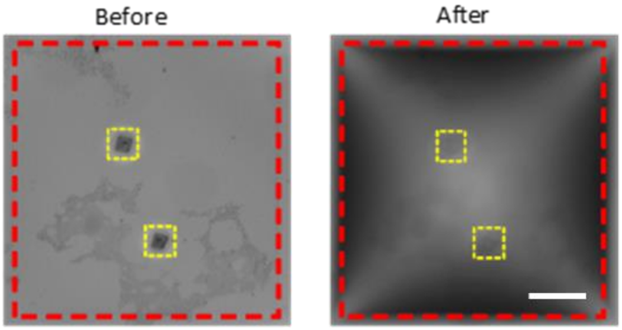

Figure 6.2 Membrane deflection before and after the application of a pressure of 20 psi. Scale bar represents 100 µm.

In order to measure the deflection experimentally, the elevation difference at the apex of the membrane was used as reference, and the in-focus z-positions were recorded. The applied pressure on the surface of the substrate was monitored and regulated to achieve a constant value throughout the measurement of the deflection. Fringe patterns can be observed in the deflected membrane case, which correspond to the reflected light, confirming a level gradient along the surface of the substrate, and a maximum translation at the apex. The z-positioning precision of the inverted microscopy system used in this study is 0.2 µm, which allowed measuring deflec¬tions with micrometer precision, at 2-µm intervals.

Figure 6.6 shows experimental and simulations results for applied pressures of 1 to 20 psi. The trend from the linear simulation model is linear, as expected, with corresponding minimum and maximum deflections of 1.209 and 24.08 µm. In contrast, the deflection results from the nonlinear model decrease with the applied pressure, with minimum and maximum values of 2.584 and 19.39 µm. The same trend was found for experimental values, the magnitude of the maximum deflection at the apex decreasing with the applied pressure. This can be explained by considering the physical restriction along the frame of the free-standing membrane, and due to the mechanical properties of the material. The figure also shows the results from three analytical models that were used to obtain theoretical values: the Rijn et al.,[22] Ugural[28] and Kovacs et al.[29] models, as well as an adjusted Kovacs model fit with the experimental values. These models are similar to each other, where all consider the perforation in a membrane as an error factor affecting the Young's modulus of the membrane. The deflection of a membrane is given by:[30]

$$w_{max} = k_0\, L \sqrt[3]{\frac{P_0\, L}{E_{eff}\, h}} \tag{6.1}$$

where w is the z-axis displacement, L and h are the size and the thickness of the membrane and P_0 is the applied pressure. The constant k_0 equals 0.318, 0.325 and 0.319 within Rijn's, Ugural's, and Kovacs' models respectively.[30] E_{eff} is the effective Young's modulus, and is calculated as $E_{eff} = (1 - P)E_{closed}$, where E_{closed} is the Young's modulus of unperforated membrane and P is the correction factor. P is dependent on the perforation and is defined as the fraction of the open areas over the total area of the membrane. As the models are similar, there is negligible difference between the deflection values obtained using the three different models.[30] In the case of the optofluidic sensor, the deformable section of the membrane is smaller than the 500 µm by 500 µm of the free-standing substrate, as observed in Figure 6.5. The theoretical models do not consider the frame around the deformable area. Therefore, there is an offset between the deflection values obtained using the models and those obtained experimentally, as shown in Figure 6.6.

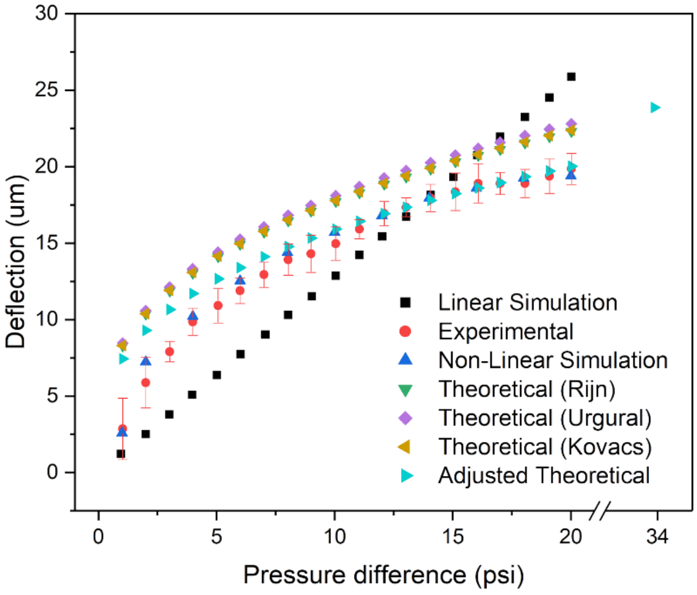

Figure 6.3 Experimental, theoretical and simulation results of the maximum membrane deflection (apex). Error bars indicate standard deviation (n = 5).

The experimental results have a similar trend compared to the theoretical models. Over the non-linear region (<7 psi), the experimental values are on average ~32% below the theoretical maximum, and ~12% below the theoretical maximum within the linear region (>7 psi). The slope for and the experimental values and the theoretical (Kovacs) were 0.4831 and 0.4826 µm/psi, respectively within the linear region, with R-square (COD) values of 0.937 and 0.993, respectively. The slopes indicate that the models do not quantify the actual deflection of the membrane. However, they accurately represent the trend of the membrane's deflection. As such, the unperforated area around the nanohole arrays is influential on the mechanical stability of the membrane. With the assumption that some length of area around the unperforated area does not deflect, then the deflection of the membrane can be rewritten as such:

$$w_{max,} = k_0\, L_{eff}\ \sqrt[3]{\frac{P_0\, L_{eff}}{E_{eff}\, h}} \tag{6.2}$$

where L_{eff}, is the effective length of the membrane based on the experimental values and calculated as $L_{eff} = \sqrt{Area\ of\ holes/P_{eff}}$. P_{eff} is the effective correction factor based on the experimental values, where it is assumed that some length around the unperforated area does not deflect. E_{eff} is adjusted to the experimental values and calculated as $E_{eff} = \left(1 - P_{eff}\right)E_{closed}$. The model found a range of P_{eff} values based on each experimental deflection point from 2.138(10^{-3}) to 5.09(10^{-4}), corresponding to effective membrane lengths of 225 µm to 460 µm respectively. Figure 6.6 illustrates that the model is incapable of fitting all the experimental values with one value of P_{eff}. The initial deflection value of the experimental values has an L_{eff} of 225 µm, where the L_{eff} non-linearly increases until it plateaus to a constant value of 460 µm within the linear region of the experimental values. The effective length paints a clear image of the membrane's behaviour under pressure. Initially, at low pressures, only the center area of the membrane deflects, while majority of the membrane is not affected by the applied pressures. As the applied pressure increases, the deflected area grows until it reaches a maximum constant value (460 µm). Even at the maximum value of effective lengths, some outer areas of the membrane do not deflect, reassuring the limitations of deflection model. The experiment was not designed to bring the substrate to mechanical failure; however, the pressure value for the breaking point can be extrapolated from the theoretical model based on the material's properties. The inflection point of the membrane is not at the edges of the membrane but limited to the effective length of the membrane (i.e. L_{eff}). Based on Rijn et al. and Timoshenko et al. models, the maximum pressure applied can be found based on the total stress of the material as shown in Equation 6.3.[22,31]

$$\sigma_{total} = \sigma_{tensile} + \sigma_{bend} = \frac{0.297}{1 - v}\left(1 + \frac{1.439}{0.358}\right)\sqrt[3]{\frac{{P_0}^2\, {L_{eff}}^2\, E_{eff}}{(1 - v^2)\, h^2}} \tag{6.3}$$

where σ_{total} is the total stress of the membrane, and $\sigma_{tensile}$ and σ_{bend} are the tensile stress due to stretching and the maximum bending stress near the middle of the membrane's deflection edges respectively. The model is valid when the substrate is under a substantial load that results in large deflections (i.e. $w_{max}/h \gg 1$). Considering the reported ultimate stress, σ_ultimate, is in the order of 109 Pa, and the intrinsic tensile stress 108 Pa for a silicon nitride membrane, then the internal stresses can be neglected since they are order of magnitudes lower than the total stress.[22] For a nonductile inorganic material, the σ_ultimate is equivalent to its yield stress. Taking 2.5 GPa as σ_total, based on the mechanical properties of the material, a pressure of 33.91 psi and deflection of 23.87 μm are obtained, corresponding to the maximum possible values at the verge of mechanical failure.[32] This theoretical maximum deflection value at the verge of failure, which follows well the trend of the adjusted theoretical curve, is shown in Figure 6.6.

6.4 Conclusions

This work presents an investigation of the deflection and structural stability of optofluidic nanohole array-based sensors operating in flow-through mode. The study was approached using experiments, theoretical models and FEA via computer simulations through FEM. Linear and nonlinear material models were simulated using COMSOL Multiphysics software. The simplified linear model had an expected discrepancy with experimental values but were useful to obtain an estimation of the order of magnitude of transmembrane pressures that would allow to study the deflection of the substrate when used in flow-through operation, while avoiding mechanical failure. The discrepancies were up to ~20%. In contrast, the nonlinear model, accounting for a complete nanohole array, described accurately the deflection values obtained experimentally. The stresses corresponding to these deflections can be used to predict maximum operation values that could prevent failure of the optofluidic nanostructures. Three analytical models were used to analyse the deformation of the sensor. The models depicted the behaviour of the deflected substrate under pressure but did not intrinsically fit the experimental results since only a fraction of the surface deflects due to the attachment of the free-standing substrate to the silicon frame. Even when the entire 500 µm membrane is under pressure, only a reduced square area, ranging from 225 µm to a maximum of 460 µm per side, deflects. Once adjusted, the theoretical model fit better the experimental deflection values. Based on the models, the fracture point was extrapolated from the maximum yield stress of silicon nitride membranes. As the membranes are composed of nonductile, inorganic material, their yield stress is equivalent their ultimate stress, which resulted with a maximum possible deflection of 23.9 µm, with the applied pressure of 33.9 psi. Although the optofluidic structures are limited by their fragile mechanical stability in flow-through operation, these result show that they are capable of withstanding transmembrane pressures compatible with sensing applications, where analyte is required to be brought into the apertures. Simulations that could predict the deflection of the structures would greatly benefit the design needs of flow-through optofluidic platforms for specific applications in the context of biosensing.

6.4 References

(1) The Canadian Medical Technology Sector: Opportunities for Swiss Companies. OSEC Business Network Switzerland2011.

(2) Preechaburana, P.; Gonzalez, M. C.; Suska, A.; Filippini, D. Surface Plasmon Resonance Chemical Sensing on Cell Phones. Angew. Chemie - Int. Ed. 2012, 51 (46), 11585–11588. https://doi.org/10.1002/anie.201206804.

(3) Comina, G.; Suska, A.; Filippini, D. Autonomous Chemical Sensing Interface for Universal Cell Phone Readout. Angew. Chemie Int. Ed. 2015, 54 (30), 8708–8712. https://doi.org/10.1002/anie.201503727.

(4) Ding, X.; Srinivasan, B.; Tung, S. Development and Applications of Portable Biosensors. Journal of Laboratory Automation. SAGE Publications Inc. August 25, 2015, pp 365–389. https://doi.org/10.1177/2211068215581349.

(5) Li, G.; De Clercq, E. Therapeutic Options for the 2019 Novel Coronavirus (2019-NCoV). Nature reviews. Drug discovery. NLM (Medline) March 1, 2020, pp 149–150. https://doi.org/10.1038/d41573-020-00016-0.

(6) Boratto, P. V. M.; Oliveira, G. P.; Machado, T. B.; Andrade, A. C. S. P.; Baudoin, J. P.; Klose, T.; Schulz, F.; Azza, S.; Decloquement, P.; Chabrière, E.; Colson, P.; Levasseur, A.; la Scola, B.; Abrahão, J. S. A Mysterious 80 Nm Amoeba Virus with a Near-Complete "ORFan Genome" Challenges the Classification of DNA Viruses. bioRxiv. bioRxiv January 28, 2020, p 2020.01.28.923185. https://doi.org/10.1101/2020.01.28.923185.

(7) Brolo, A. G.; Gordon, R.; Leathem, B.; Kavanagh, K. L. Surface Plasmon Sensor Based on the Enhanced Light Transmission through Arrays of Nanoholes in Gold Films. Langmuir 2004, 20 (12), 4813–4815. https://doi.org/10.1021/la0493621.

(8) Ebbesen, T. W.; Lezec, H. J.; Ghaemi, H. F.; Thio, T.; Wolff, P. A. Extraordinary Optical Transmission through Sub-Wavelenght Hole Arrays. Nature 1998, 391 (6668), 667–669. https://doi.org/10.1038/35570.

(9) Craighead, H. Future Lab-on-a-Chip Technologies for Interrogating Individual Molecules. Nature. Nature Publishing Group July 27, 2006, pp 387–393. https://doi.org/10.1038/nature05061.

(10) Ahn, C. H.; Choi, J. W.; Beaucage, G.; Nevin, J. H.; Lee, J. B.; Puntambekar, A.; Lee, J. Y. Disposable Smart Lab on a Chip for Point-of-Care Clinical Diagnostics. In Proceedings of the IEEE; Institute of Electrical and Electronics Engineers Inc., 2004; Vol. 92, pp 154–173. https://doi.org/10.1109/JPROC.2003.820548.

(11) Herrmann, M.; Veres, T.; Tabrizian, M. Enzymatically-Generated Fluorescent Detection in Micro-Channels with Internal Magnetic Mixing for the Development of Parallel Microfluidic ELISA. Lab Chip 2006, 6 (4), 555–560. https://doi.org/10.1039/b516031f.

(12) Chin, C. D.; Linder, V.; Sia, S. K. Lab-on-a-Chip Devices for Global Health: Past Studies and Future Opportunities. Lab on a Chip. Royal Society of Chemistry December 19, 2007, pp 41–57. https://doi.org/10.1039/b611455e.

(13) Gomez-Cruz, J.; Nair, S.; Ascanio, G.; Escobedo, C. Flow-through Nanohole Array Based Sensor Implemented on Analogue Smartphone Components. In Proceedings of SPIE - The International Society for Optical Engineering; 2017; Vol. 10346. https://doi.org/10.1117/12.2272433.

(14) Soler, M.; Belushkin, A.; Cavallini, A.; Kebbi-Beghdadi, C.; Greub, G.; Altug, H. Multiplexed Nanoplasmonic Biosensor for One-Step Simultaneous Detection of Chlamydia Trachomatis and Neisseria Gonorrhoeae in Urine. Biosens. Bioelectron. 2017, 94, 560–567. https://doi.org/10.1016/j.bios.2017.03.047.

(15) Yanik, A. A.; Huang, M.; Kamohara, O.; Artar, A.; Geisbert, T. W.; Connor, J. H.; Altug, H. An Optofluidic Nanoplasmonic Biosensor for Direct Detection of Live Viruses from Biological Media. Nano Lett. 2010, 10 (12), 4962–4969. https://doi.org/10.1021/nl103025u.

(16) Escobedo, C.; Chou, Y.-W.; Rahman, M.; Duan, X.; Gordon, R.; Sinton, D.; Brolo, A. G.; Ferreira, J. Quantification of Ovarian Cancer Markers with Integrated Microfluidic Concentration Gradient and Imaging Nanohole Surface Plasmon Resonance. Analyst 2013, 138 (5), 1450. https://doi.org/10.1039/c3an36616b.

(17) Gomez-Cruz, J.; Nair, S.; Manjarrez-Hernandez, A.; Gavilanes-Parra, S.; Ascanio, G.; Escobedo, C. Cost-Effective Flow-through Nanohole Array-Based Biosensing Platform for the Label-Free Detection of Uropathogenic E. Coli in Real Time. Biosens. Bioelectron. 2018, 106 (January), 105–110. https://doi.org/10.1016/j.bios.2018.01.055.

(18) Escobedo, C.; Brolo, A. G.; Gordon, R.; Sinton, D. Optofluidic Concentration: Plasmonic Nanostructure as Concentrator and Sensor. Nano Lett. 2012, 12 (3). https://doi.org/10.1021/nl204504s.

(19) Cruz, S.; Hönig-d'Orville, A.; Müller, J. Fabrication and Optimization of Porous Silicon Substrates for Diffusion Membrane Applications. J. Electrochem. Soc. 2005, 152 (6), C418. https://doi.org/10.1149/1.1914747.

(20) Sinton, D.; Gordon, R.; Brolo, A. G. Nanohole Arrays in Metal Films as Optofluidic Elements: Progress and Potential. Microfluid. Nanofluidics 2008, 4 (1–2), 107–116. https://doi.org/10.1007/s10404-007-0221-0.

(21) Wu, H. A.; Liu, G. R.; Wang, J. S. Atomistic and Continuum Simulation on Extension Behaviour of Single Crystal with Nano-Holes. Model. Simul. Mater. Sci. Eng. 2004, 12 (2), 225–233. https://doi.org/10.1088/0965-0393/12/2/004.

(22) Van Rijn, C.; Van Der Wekken, M.; Nijdam, W.; Elwenspoek, M. Deflection and Maximum Load of Microfiltration Membrane Sieves Made with Silicon Micromachining. J. Microelectromechanical Syst. 1997, 6 (1), 48–54. https://doi.org/10.1109/84.557530.

(23) Escobedo, C.; Brolo, A. G.; Gordon, R.; Sinton, D. Nanoplasmonics as Nanofluidics: Transport and Sensing in Flowthrough Nanohole Arrays. In Microfluidics, BioMEMS, and Medical Microsystems IX; SPIE, 2011; Vol. 7929, p 79290Q. https://doi.org/10.1117/12.875848.

(24) Escobedo, C. On-Chip Nanohole Array Based Sensing: A Review. Lab on a Chip. Royal Society of Chemistry July 7, 2013, pp 2445–2463. https://doi.org/10.1039/c3lc50107h.

(25) Duffy, D. C.; McDonald, J. C.; Schueller, O. J. A.; Whitesides, G. M. Rapid Prototyping of Microfluidic Systems in Poly(Dimethylsiloxane). Anal. Chem. 1998, 70 (23), 4974–4984. https://doi.org/10.1021/ac980656z.

(26) Luecke, W. E.; Wiederhorn, S. M. A New Model for Tensile Creep of Silicon Nitride. J. Am. Ceram. Soc. 2004, 82 (10), 2769–2778. https://doi.org/10.1111/j.1151-2916.1999.tb02154.x.

(27) Wunderlich, W. Ceramic Materials; Wunderlich, W., Ed.; Sciyo, 2010. https://doi.org/10.5772/243.

(28) Ugural, A. C. Stresses in Beams, Plates, and Shells; Applied and Computational Mechanics; CRC Press, 2009.

(29) Mescheder, U.; Kovács, Á.; Vízváry, Z.; Kovács, A.; Mescheder, U. LARGE DEFLECTION ANALYSIS OF PERFORATED SILICON NITRIDE MEMBRANES; 2006.

(30) Kovács, A.; Kovács, Á.; Pogány, M.; Mescheder, U. Mechanical Investigation of Perforated and Porous Membranes for Micro- and Nanofilter Applications. Sensors Actuators, B Chem. 2007, 127 (1), 120–125. https://doi.org/10.1016/j.snb.2007.07.044.

(31) Timoshenko, S.; Woinowsky-Krieger, S. Theory of Plates and Shells, 2nd ed.; McGraw-Hill, 1959.

(32) Boe, A.; Coulombier, M.; Pardoen, T.; Raskin, J.-P.; Boé, A.; Coulombier, M.; Safi, A.; Pardoen, T.; Raskin, J.-P. On-Chip Testing Laboratory for Nanomechanical Characterization of Thin Films; 2009.

Chapter 7

Variable Pitch Crossed Surface Relief Gratings for Point-of-Care Sensing

With minor changes to fulfill formatting requirements, this chapter is as it appears in: Juan Gomez-Cruz, Yazan Bdour, Eduardo Carrasco, Ribal Georges Sabat and Carlos Escobedo. 2019 International Conference on Electromagnetics in Advanced Applications (ICEAA), 0515-0515, IEEE.

7.1 Abstract

Nanostructures consisting of crossed surface relief gratings (CSRGs) support surface plasmon resonances (SPRs) that are compatible with biosensing applications.[1,2] At normal incidence, surface plasmons are excited between a metal and a dielectric at a light wavelength (λ_{SPR}) given by $\lambda_{SPR} = n\Lambda\left[\sqrt{\varepsilon_m/(n^2+\varepsilon_m)}\right]$, where n is the index of refraction of the dielectric, and ε_m is the real part of the permittivity of the metal and Λ is the grating pitch. When placed between crossed linear polarizers, CSRGs allow for plasmonic energy exchange between the two superimposed gratings that eliminate any incident polychromatic light, except for the narrow SPR bandwidth where polarization conversion occurs. The result is an effective transmission of the SPR signal with a high signal-to-noise ratio. The single pitch of CSRGs, however, limit their operation to a specific plasmonic resonance wavelength. Here, we present a plasmonic sensor based on variable-pitch CSRG that allows plasmonic resonances at different wavelength bandwidth depending on the illuminated region. The variable-pitch CSRGs (VP-CSRGs) are fabricated on azobenzene-functionalized films through a simple two-step procedure. Fig. 1a presents an actual AFM image of the surface of a nanofabricated VP-CSRGs. The plasmonic response of the VP-

CSRG sensor was evaluated using Finite-Difference Time-Domain (FDTD) simulations to show the e-field intensity distribution on the gold-coated VP-CSRG surface. Electric field enhancement and distribution, due to the plasmonic conversion, was assessed through the change of the RI of the dielectric medium in contact with the metallic crossed gratings, and through the spectral diversity of the light source to excite the surface plasmons. For the simulations, the surface of the CSRGs with pitches of 520, 540 and 560 nm were modeled using the function $f(x, y) = G(\cos[(2\pi/p)x] + \cos[(2\pi/p)y])$, where G is the amplitude and p the period of the structure (Fig. 1a). The simulations were used to obtain the e-field intensity distribution, normalized with respect to the incident plane wave. Periodic boundary conditions in both x and y directions and a perfectly matched layer (PML) in the z direction were used for the analysis region. A uniform mesh size of 3 nm was used for the envelope of the nanostructure, comprising the azobenzene layer, the gold film and the dielectric medium, in all the directional axes. A plane wave, polarized along the y-axis and orthogonal to the x-y plane, was employed to induce a SPR in the structure. Fig. 1b demonstrates the plasmonic excitation in the x-direction, when using p-polarized light and the absence of plasmonic excitation in the y-direction. However, when s-polarized light is used, the nanostructures are excited in the y-direction. These results present an evidence on the unique plasmonic energy transfer between the crossed gratings that has been hypothesised before.[1] Experimentally, these results can be used to confirm that the transmitted light acquired in a collinear setup using VP-CSRGs between two orthogonal polarizers corresponds, only, to the plasmonic signature of the nanostructure.

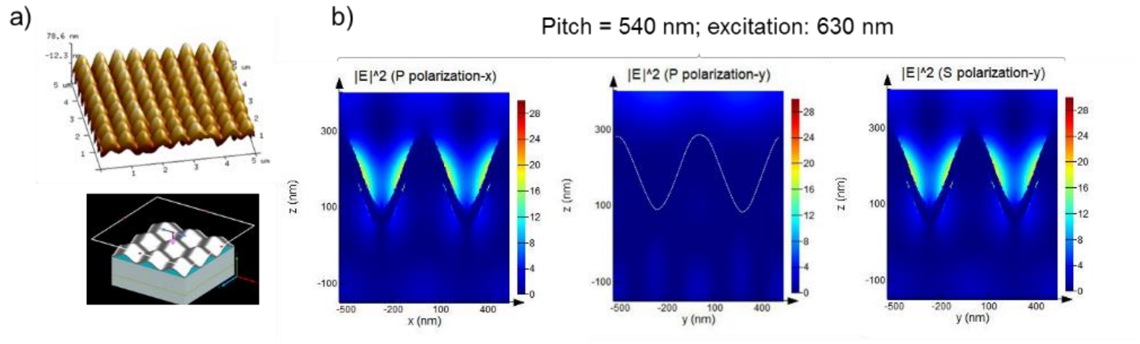

Figure 7.1 a) AFM image of the VP-CSRG (top) and the model used for the FDTD simulations (bottom). b) Simulation results for p- and s-polarized light in the x- and y-directions along 540-nm-pitch VP-CSRGs.

7.2 References

(1) Nair, S.; Escobedo, C.; Sabat, R. G. Crossed Surface Relief Gratings as Nanoplasmonic Biosensors. ACS Sensors 2017, 2 (3), 379–385. https://doi.org/10.1021/acssensors.6b00696.

(2) Nair, S.; Gomez-Cruz, J.; Manjarrez-Hernandez, Á.; Ascanio, G.; Sabat, R.; Escobedo, C. Selective Uropathogenic E. Coli Detection Using Crossed Surface-Relief Gratings. Sensors 2018, 18 (11), 3634. https://doi.org/10.3390/s18113634.

Chapter 8

Cicada Wing Inspired Template-Stripped SERS Active 3D Metallic Nanostructures for the Detection of Toxic Substances

With minor changes to fulfill formatting requirements, this chapter is as it appears in: Srijit Nair, Juan Gomez-Cruz, Gabriel Ascanio, Aristides Docoslis, Ribal Georges Sabat and Carlos Escobedo. *Sensors* 2021, *21*(5), 1699.

Abstract: This article introduces a bioinspired, cicada wing-like surface-enhanced Raman scattering (SERS) substrate based on template-stripped crossed surface relief grating (TS-CSRG). The substrate is polarization-independent, has tunable nanofeatures and can be fabricated in a cleanroom-free environment via holographic exposure followed by template-stripping using a UV-curable resin. The bioinspired nanostructures in the substrate are strategically designed to minimize the reflection of light for wavelengths shorter than their periodicity, promoting enhanced plasmonic regions for the Raman excitation wavelength at 632.8 nm over a large area. The grating pitch that enables an effective SERS signal is studied using Rhodamine 6G, with enhancement factors of the order of 10^4. Water contact angle measurements reveal that the TS-CSRGs are equally hydrophobic to cicada wings, providing them with potential self-cleaning and bactericidal properties. Finite-difference time-domain simulations are used to validate the nanofabrication parameters and to further confirm the polarization-independent electromagnetic field enhancement of the nanostructures. As a real-world application, label-free detection of melamine up to 1 ppm, the maximum concentration of the contaminant in food permitted by the World Health Organization, is demonstrated. The new bioinspired functional TS-CSRG SERS substrate holds great potential as a large-area, label-free SERS-active substrate for medical and biochemical sensing applications.

8.1 Introduction

Biomimicry is an emerging field with the objective of replicating physical or chemical attributes found in nature to create human-made devices. The development of biomimetic materials and devices has been particularly useful in optics and sensing applications.[1,2] Examples of bioinspired materials include polymer-based biohybrid sensor interfaces,[3] functional nanostructures of S-proteins for breast cancer cell detection,[4] wearable eye health monitoring sensors,[5] anti-Moiré grids with the optoelectronic performance[6] and SERS substrates inspired by the geometry of lotus seedpod.[7] Subwavelength periodic structures, such as nipple arrays and tapered pillars, can be found in some insect eyes and wings. Cicadas, in particular, have tapered nanopillars in their transparent wings to suppress light reflection, which makes them invisible to predators[8] and provides them with self-cleaning, superhydrophobic and bactericidal properties.[9] The amplitude and periodicity of the nanopillars range between 170 and 300 nm in order to achieve minimal reflection in the visible 300–800 nm spectrum.[10–13] In previous studies, direct deposition of metals on cicada wings has been used to investigate broadband light absorption properties of the nanostructures,[14] as surface-enhanced Raman scattering (SERS) substrates[15,16] and to produce bio-templated SERS-active nanostructures transferred to optical fibers.[17] Other studies include photocatalytically deposited metallic nanoparticles on cicada and butterfly wings.[18] However, these methodologies enable the production of fixed-pitch nanostructures, preventing the tailored fabrication of SERS active surfaces of similar or identical morphologies.

Nanostructures that support surface plasmon resonance (SPR) have been widely used for sensing and biosensing applications through the use of different techniques, including SPR spectroscopy,[19–25] SPR imaging[26–29] and surface-enhanced Raman scattering (SERS) spectroscopy.[30–37] SERS, particularly, allows for highly sensitive detection and specific identification of analytes. Nevertheless, metallic nanostructures must enable high enhancement of near-surface electromagnetic field intensities to qualify as SERS substrate.[36] Nano-engineered substrates such as metallic tips,[35] nanohole arrays[38] and nanogratings[32] have been investigated for better controlled and reproducible SERS substrates. These structures provide a uniform enhancement over a large surface area, negating the concept of plasmonic "hot-spots" where only specific regions experience electromagnetic field strength enhancement.[15] Metallic nanogratings, in particular, experience large-area uniform electromagnetic enhancement, which increases the chances for analyte detection via SERS spectroscopy.[39–41] However, excitation of plasmons on 1D nanogratings is maximized when the polarization of the incident light is aligned with the grating vector.[34] Optimal enhancement is determined by the morphology of the nanogratings and the relative angle between the incoming light polarization and the grating vector. The polarization dependency of the nanostructures can be overcome by structuring them into a 2-dimensional (2D) arrangement. Crossed relief gratings (CSRGs) are 2D nanostructures that enable polarization-independent SERS detection, offering enormous potential for specific analyte sensing.[19,21,26] SPR excitation by one of the superimposed gratings is re-radiated by its orthogonal counterpart in a polarization state that is orthogonal to that of the incident light. Metallic CSRG may enhance the electromagnetic field intensity at a metal-dielectric boundary near-surface region by ~30 times, but they are fabricated from an azobenzene molecular glass (gDR1) solution that consists of azobenzene chromophore molecules, which are SERS active. This aspect has limited the deployment of CSRGs for SERS-based analysis as target signals may get masked by the azobenzene Raman spectra. One way to tackle this problem, and the main motivation of this work, is by replicating the tapered nanopillars in the cicada wings, to take advantage of their optical properties, and to use template stripping to allow the transfer of the metallic nanostructures to another substrate without the gDR1 layer that could potentially mask SERS signals, with the additional benefit of being pitch-customizable to provide antireflective (AR) or signal generation properties at desired wavelengths. Template stripping is a cost-effective and cleanroom-free approach that has been used for transferring other types of metallic nanostructures while preserving their shape and plasmonic efficiency.[42,43]

Here, we present a polarization-independent, template-stripped Ag CSRG (TS-CSRG) SERS substrate, inspired by the tapered nanopillars found in the Cicada wings,[15] along with the outstanding plasmonic capabilities of subwavelength metallic CSRG. The new methodology is achieved using holographic exposure and template-stripping of silver-coated CSRG using a UV-curable epoxy that enables fabrication of homogeneous, pitch-customizable, large-area, and low-cost substrates that allows for reproducible SERS signals. FDTD simulations are used in the design process to confirm the enhancement and distribution of the electromagnetic field along the nanostructures. The pitch-dependency of the TS-CSRG is used to tailor the SERS signals response upon the adsorption of Raman reporter molecule Rhodamine 6G (R6G). To showcase the capabilities of Ag TS-CSRG as SERS substrates in a real sensing context, we demonstrate the effective, label-free detection of melamine at concentrations of 1 ppm, which corresponds to the maximum residue limit for melamine in infant formula dictated by the World Health Organization (WHO).[44]

8.2 Materials and Methods

8.2.1 Atomic Force Microscopy

Imaging of the cicada wings, CSRGs, and TS-CSRGs structures was performed using a Dimension Edge atomic force microscope (AFM) system (Bruker, Massachusetts, USA). A ScanAsyst-Air AFM tip (Bruker, Massachusetts, USA) was utilized to scan a 5 µm × 5 µm area, using the peak-force tapping mode, with a scan rate of 1 Hz per line. Bruker NanoScope Analysis software was used to fit and analyze the AFM scans and obtain parameters such as the topography, depth, and pitch of the structures.

8.2.2 Fabrication of Nanogratings

The surface plasmon resonance wavelength of CSRGs is found by matching the SPR wavevector to the diffracted light via the grating equation so that the following equality is obtained:[19]

$$\mathrm{k_{spp}} = \mathrm{k_0\ nsin\theta\ \pm\ 2\pi m/\Lambda} \tag{8.1}$$

where k_{sp} is the surface plasmon wave number, k_0 is the incident light wave number in free space, n is the refraction index of the dielectric, θ is the incidence angle, m is the diffraction order (normally limited to unity), and Λ is the grating pitch.

Fabrication of the CSRGs was performed using the rapid and high-throughput interferometric technique described elsewhere.[19,21,26] Azobenzene molecular glass (gDR1) solution (DR1-glass, 2.99 mM, 94%) was prepared according to the methods described elsewhere.[45] A volume of 500 µL of 3 wt % gDR1 solution, diluted in dichloromethane, was spin-coated on a 2.5 cm × 2.5 cm Corning 0215 soda lime microscope glass slide (TED PELLA, INC., California, USA) using a Headway Research spin-coater (Headway Research Inc. Garland, TX, USA) at 1000 RPM for 20 s. The spin-coated samples were then dried and annealed for 1 h at 90 °C in a Yamato ADP-21 oven (Santa Clara, CA, USA) to generate a uniform gDR1 film of approximately 200 nm thick, verified by a Sloan Dektak II surface profiler (Veeco Instruments Inc., Plainview, NY, USA). CSRGs were written on the gDR1-coated substrates by direct holographic exposure to the laser-light interference pattern assisted by a Lloyd mirror optical setup. The laser beam from a solid-state diode-pumped laser (COHERENT, USA, Verdi V6, λ = 532 nm, irradiance = 140 mW/cm^2) was directed onto a Lloyd mirror optical setup to allow for molecular mass transport of the azo-molecules to generate of nanopatterned SRGs. After the initial inscription of the SRGs (time of exposure = 300 s), the sample was rotated by 90° and a second exposure for 100 s was performed to fabricate orthogonally superimposed SRGs. An 80-nm layer of silver was subsequently sputtered over the CSRG using a Bal-Tec SCD 050 sputter-coater, to make an Ag-CSRG. The prepared samples had a periodicity of 450, 500, 550, 600 nm.

8.2.3 Template-Stripping Procedure

The fabricated Ag-CSRG was spin-coated with a UV-curable epoxy (NOA61, Norland Products Inc., NJ, USA) to generate uniform epoxy coating. Next, a pre-cleaned Corning 0215 soda lime microscope glass slide (TED PELLA, INC., California, USA) was pressed against the epoxy-coated Ag-CSRG. The sandwiched system was then exposed to UV light in an enclosed UV chamber (Novascan PSD-UV, Novascan Technologies Inc., IA, USA) for 30 min. When the epoxy was cured, the patterned silver was stripped from the Ag-CSRG by a simple peel-off. The stripped substrate, consisting of the smooth Ag nanogratings, was subjected to a final rinsing with 10% ethanol and DI water to dissolve and remove any remaining gDR1 from the metal surface. The cleaned substrate was then air-dried and stored in a microscope glass slide holder for further use.

8.2.4 Raman Measurements

A Horiba/Jobin-Yvon Raman spectrometer (Model: LabRAM) with a 632.8 nm HeNe laser (17 mW), 1800 1/mm grating and an Olympus BX-41 microscope system were used. The collection of spectra was performed in the backscattered mode under the following conditions: ×100 microscope objective, 500 μm pinhole, 500 μm slit width, laser filter 10×, for a sampling time of 10 seconds with 10 repeats. All Raman spectra were background corrected through polynomial subtraction, and the noise was reduced with a Savitsky–Golay filter.

8.2.5 Analyte Sample Preparation

R6G was dissolved in methanol at a stock concentration of 0.1 M and diluted in methanol to generate solutions in the range of 1 mM–1 µM. Melamine was dissolved in Millipore® water to a stock concentration of 1 mg mL^{-1} (1000 ppm) and diluted in water to generate solutions in the range of 100 ppm–1 ppm.

8.2.6 Contact Angle Measurements

Contact angle measurements were performed using an OCA 15EC digital goniometer (DataPhysics, Charlotte, NC, USA). Droplets (volume of 2.56 ±0.13 µL, n = 5) of Nanopure water were dispensed onto a 500 nm Ag TS-CSRG at standard conditions using an electronically controlled syringe. The resulting contact angle was calculated using the SCA 20 software module (DataPhysics, Charlotte, NC, USA) with a Young-Laplace fitting feature for the sessile drop method.

8.2.7 Enhancement Factor Calculations

SERS EF for R6G molecule absorbed on Ag-CSRG was calculated using the following equation:[46]

$$EF = (I_{SERS} / N_{SERS})/(I_{Bulk} / N_{Bulk}) \tag{8.2}$$

I_{SERS} and I_{Bulk} are the intensities of the 1358 cm^{-1} peak with SERS and normal Raman (flat Ag surface), respectively. N_{Bulk} is the number of molecules illuminated in bulk, giving a normal Raman signal, and N_{SERS} is the number of molecules illuminated on the nanostructured metallic substrate, giving the SERS signal. The peak at 1358 cm^{-1} represents intensity at a characteristic band wave number for R6G absorbed on an Ag-CSRG and a flat Ag substrate.

8.2.8 Finite-Difference Time-Domain (FDTD) simulations

Three-dimensional FDTD was used to simulate the distribution of the near-field electromagnetic field on the surface of the TS-CSRG using Lumerical FDTD Solutions software. Simulations under S and P polarizations were recorded and added to emulate the plasmonic response under a quasi-unpolarized broadband excitation light source. Symmetric and antisymmetric boundary conditions were set for the x- and y- directions, respectively, and a perfectly matched layer (PML) in the z-direction. The dielectric permittivity used in the simulations for the UV-curable epoxy and silver were obtained from the manufacturer and the literature, respectively.[47] The topography of a CSRG was modeled according to the following function:

$$\begin{aligned} f(x,y)=A/2\{&|\sin[(4\pi/p)x]|-|\cos[(4\pi/p)x]|-|\sin[(8\pi/p)x]|+|(|\sin[(4\pi/p)x]|-\\ &|\cos[(4\pi/p)x]|)|+|\sin[(4\pi/p)y]|-|\cos[(4\pi/p)y]|-|\sin[(8\pi/p)y]|+\\ &|(|\sin[(4\pi/p)y]|-|\cos[(4\pi/p)y]|)|-\cos[(8\pi/p)x]-\cos[(8\pi/p)y]\} \end{aligned} \tag{8.3}$$

where A and p correspond to the amplitude and period of the structure, respectively, in accordance with the AFM characterization. A uniform mesh size of 3 nm was used for the envelope of the nanostructure, comprising the UV-curable epoxy, the silver film, and the dielectric medium in all the directional axes. A time-averaged electric field intensity distribution, normalized with respect to the incident plane wave $|E / E_0|^2$, was calculated for the Ag-CSRG. A frequency-domain field profile is placed at the *xy* plane of the CSRG. To match experimental conditions, $|E / E_0|^2$ was recorded at 632.8 nm, corresponding to the excitation wavelength of the Raman apparatus.

8.2.9 Scanning Electron Microscopy

High-magnification image acquisition of the surface of TS-CSRGs was achieved using a high vacuum scanning electron microscope (SEM) Quanta FEG 150 ESEM (Field Electron and Ion Company, FEI, Oregon, USA) with BF/DF STEM detector, at 10 kV. Images of TS-CSRG of 450, 500, 550 and 600 nm were acquired at magnifications of 16000x, 20000x and 25000x (images of all TS-CSRGs are provided in the Supplementary Information).

8.3 Results and Discussion

A piece of the external façade of the wing of a natural cicada *Neotibicen canicularis* was scanned using atomic force microscopy (AFM). Figure 8.1a shows a digital picture of the cicada, and Figure 8.1b shows the AFM scan image of the external surface of a distal portion of the wing. The inset shows an image of a droplet atop the wing of the cicada, acquired during contact angle measurements (more details can be found in the Supplementary Information). Even when the AR nature of the nanostructured cicada wings is dictated by evolutionary survival strategies, the topography between different species of cicadas may vary. Figure 8.1c shows an AFM scan of the external wing topography of a wing of cicada *Cryptotympana atrata fabricius* reported previously.[48]

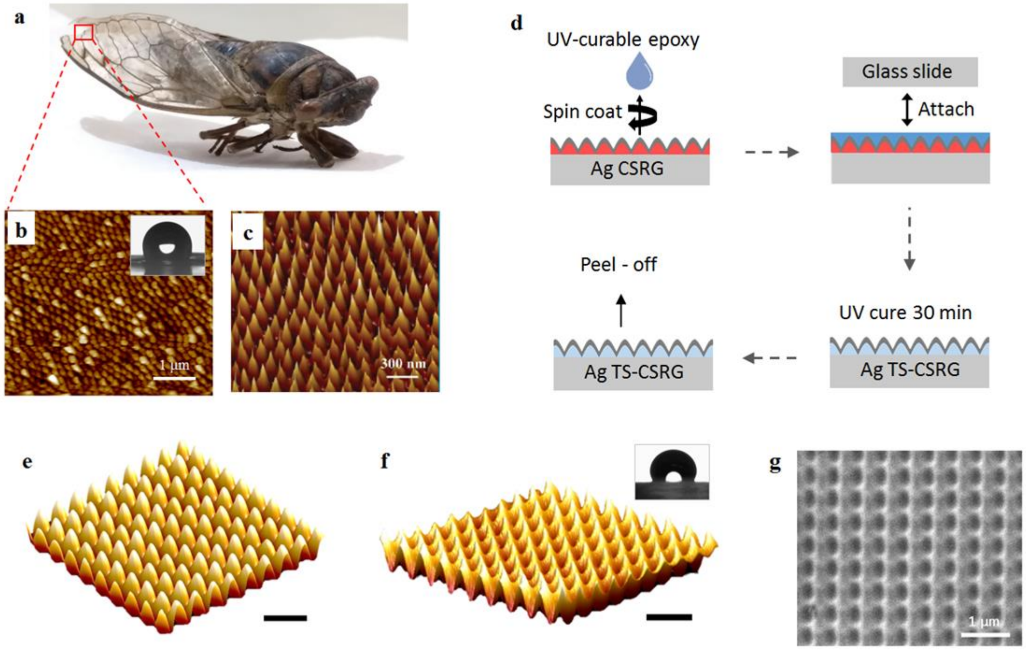

Figure 8.1 (a) Picture of a cicada *Neotibicen canicularis*. (b) atomic force microscope (AFM) image of the external surface from a piece of the wing of the cicada; inset: wetting state of a water droplet on a cicada *Neotibicen canicularis.* (c) AFM image of the external surface of the wing of a cicada *Cryptotympana atrata fabricius*. Reprinted with permission.[48] Copyright 2017, The Royal Society of Chemistry. (d) Schematic representation of the fabrication procedure for creating template-stripped Ag template-stripped crossed surface relief grating (TS-CSRG). AFM scan of a 5 µm × 5 µm area of a 500-nm-pitch (e) Ag CSRG, and (f) Ag TS-CSRG; inset: wetting state of a water droplet on an Ag TS-CSRG; scale bars correspond to 1 µm. (g) SEM image of a 500 nm-pitch Ag TS-CSRG.

As the nanostructure pattern in the cicada wing is nearly complementary to a CSRG, it can be reproduced via template-stripping to create the bioinspired SERS-active substrate. The fabrication procedure of the TS-CSRG is schematically shown in Figure 8.1d. First, surface relief gratings (SRGs) were fabricated by dissolving photoactive gDR1 in dichloromethane, followed by a spin-coating step on a pre-cleaned microscopic glass to achieve a uniform thin film of ~200 nm. Using a laser, gratings with the desired pitch were written on the gDR1-coated substrate by direct holographic exposure to an interference pattern as reported elsewhere.[19] CSRGs were achieved by the in-plane, orthogonal superposition of two sequentially inscribed SRG, as detailed in the Experimental section. Nanometer-level precision in the periodicity of the CSRG is achieved by controlling the fabrication parameters, including laser power, exposure time, and angular position of the sample. The precise control in the periodicity enables the creation of a tailored pitch in ~6 min. A 50-nm thick layer of Ag was deposited on the CSRG to provide the metallic interface for the SPR excitation. Figure 8.1e shows an AFM scan of a 500-nm-pitch Ag-coated CSRG. The final TS-CSRGs were achieved by selective lift-off of the Ag layer from the CSRG. UV-curable epoxy was spin-coated on the Ag CSRG and then pressed against a pre-cleaned microscopic glass slide and placed in a UV curing chamber for 30 min to allow the epoxy to solidify. The Ag nanostructures were then peeled off and cleaned with ethanol to dissolve any remnant gDR1. This method provided a large-area and smooth Ag TS-CSRG with a complementary pattern of the CSRG, as shown in the AFM scan in Figure 8.1f. The inset shows an image of a droplet atop the TS-CSRG, acquired during contact angle measurements (more details can be found in the Supplementary Information). Figure 8.1g shows an SEM image of a 500-nm-pitch Ag TS-CSRG, where the valleys and peaks of the nanostructures are recognizable, analogous to the topology revealed by the AFM scan. Notably, the fabricated TS-CSRGs have a remarkable resemblance to the nanostructures on the wing of cicada *Cryptotympana atrata fabricius*. The nanostructures have a total sensing area of approximately ~1 cm^2, allowing for a large-area approach for target analyte detection, in contrast to established hot spot methods.

The nanostructures on the wings of the cicadas not only provide them antireflection but also self-cleaning and antibacterial properties that arise from the hydrophobicity of the surface.[9] Compared to a flat silver substrate, the TS-CSRG allows for a metal-dielectric interface with nanoscopic features that significantly alter the wettability of the surface. Typically, the contact angles (CA) of non-wetting surfaces range between 90° and 180°, whether a perfect wetting surface is 0°. An ideal flat silver surface is perfectly wetting; although the CA can vary depending on the cleanness of the surface, it is significantly low compared to values for non-wetting surfaces.[49] The nanostructured features of Ag TS-CSRGs induce a Wenzel state, where the surface exhibits the apparent CA of a non-wetting surface,[50] similar to the self-cleaning hydrophobic surface of cicada wings. We investigated the wettability of the TS-CSRG and cicada wing by measuring the static CA using microscopic droplets of DI water. The insets in Figure 8.1b,f show, respectively, images of droplets on the external surface of a piece of a cicada *Neotibicen canicularis* wing and atop a pristine TS-CSRG taken with the automatic CA measurement system. From the images, it is qualitatively evident the hydrophobicity exhibited by both surfaces. Quantitatively, the measured CA from the cicada wing and the TS-CSRG were, respectively 115°±2.075° and 119°±3.4222° (n=5).

Electromagnetic enhancement is critical for SERS-based detection. In a backscattering approach, a surface-confined enhancement assisted by SPR excitations allows for the enhancement of small molecule Raman signals. However, a SERS substrate needs to be tailored to allow for the excitation depending on the incident laser wavelength. Using Equation (1), for air (n=1) and assuming normal incidence, the desired pitch of the gratings was calculated to be ~560 nm for a laser excitation wavelength of 632.8 nm. However, any analyte on the surface of the metal will eventually change the dielectric permittivity as perceived by the incident light. Hence, a set of TS-CSRGs with a grating pitch ranging from 450 to 600 nm with a 50-nm pitch increment was fabricated to acknowledge the dielectric change encountered by the incident light on the surface. The nanostructures were strategically designed with those periodicities to minimize the reflection of light for wavelengths shorter than the periodicity, promoting therefore enhanced plasmonic regions for the Raman excitation wavelength of 632.8 nm.

FDTD simulations were used to demonstrate the polarization-independent electric field enhancement in the vicinity of the TS-CSRG and to confirm the nanostructure pitch leading to the highest EF. Details on the methodology, including the equation utilized to replicate the topography of the nanostructures, are described in the Experimental section. Figure 8.2a,b shows, respectively, the 3D surface created from Equation (3) and the simulation model used for the FDTD simulations.

This equation was utilized to create a model of the TG-CSRGs on Lumerical FDTD solutions software to perform FDTD simulations, which are presented in Figure 8.2b. The simulations demonstrated the polarization-independent electric field enhancement in the vicinity of the TS-CSRG and confirmed the nanostructures pitch leading to the highest EF. Details on the methodology, including the equation utilized to replicate the topography of the nanostructures, are described in the Experimental section.

Figure 8.2c–f shows the electric field intensity distribution, $|E/E_0|^2$, recorded along the *xy* cross-section, for gratings with periodicities spanning from 450 nm to 600 nm for a dielectric with RI of 1.33. All the simulation results were scale-adjusted for intensity values of 0–100. The plasmonic enhancement obtained for all the structures demonstrated to be the same for s- and p-polarized incident light. Figure 8.2d shows the simulated electric field enhancement of the TS-CSRG of 500-nm pitch, which is at least five times higher than the other periodicities investigated in this work (Figure 8.2c,e and f). Additionally, it can be observed that the highest electric field enhancement occurs at the crests of the nanostructures. The strength of the electric field decreases in a quasi-radial pattern towards the center of the valleys. Although the simulations may indeed vary from real samples on account of alterations in RI or topography, they served to confirm the response for the TS-CSRG periodicities scrutinized in this work.

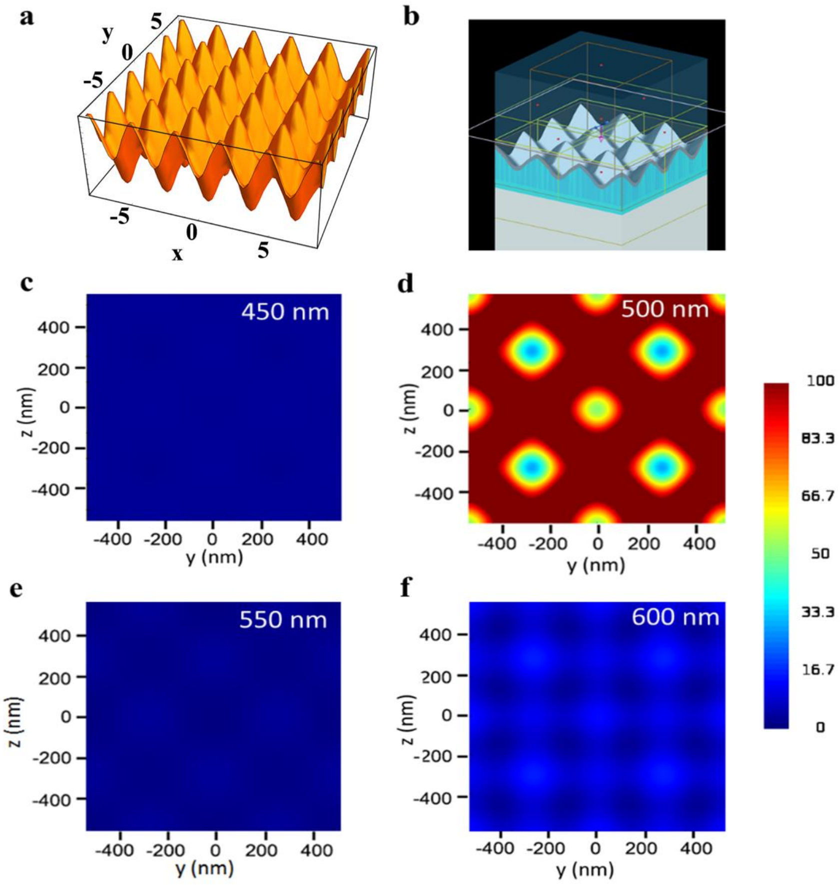

Figure 8.2 Finite-difference time-domain (FDTD) simulations. (a) 3D surface created from Equation (3). (b) FDTD simulation model. (c–f) Electric field distribution along *xy* cross-section for Ag TS-CSRGs with grating pitch spanning from 450 nm to 600 nm, with 50 nm increments.

The pitch-dependency of the TS-CSRG was used to tailor the SERS signals response upon the adsorption of Rhodamine 6G (R6G), a Raman reporter molecule with a distinct Raman spectrum. Figure 8.3a shows the Raman spectra for a flat Ag surface and TS-CSRG with pitches of 450, 500, 550 and 600 nm. Raman peaks at c.a. 610, 770, 1180, 1306, 1360, 1505, 1570, 1595, and 1645 cm^{-1} are characteristic of R6G.[51,52] The reference peak at 1360 cm^{-1}, corresponding to aromatic C-C stretching,[53] is commonly used as a reference to track changes on the surface of the substrate, and it can be clearly observed in all CSRGs. However, the peak is more prominent in the

500-nm-pitch grating, concurring with the simulation results shown in Figure 8.2c–f. The SERS enhancement factor (EF), which correlates to the evaluation of signal intensities observed from SERS-active and passive substrates (i.e., flat Ag substrate), was calculated. The Raman vibration of R6G at 1358 cm^{-1} was used for the EF calculations, and the corresponding intensity for R6G (10^{-2} M) on a flat Ag substrate was calculated to be 70 arbitrary units (a.u.). The intensities at 1358 cm^{-1} were recorded for each of the substrates with different pitches using R6G (10^{-5} M). The EF values were calculated using Equation (2) for TS-CSRG with pitches 450, 500, 550 and 600 nm were 3.8×10^4, 7.6×10^4, 6.1×10^4 and 1.6×10^4, respectively. The TS-CSRG with a pitch of 500 nm exhibited the highest EF—a value that may serve as a guideline for SERS detection applications and further investigations, with magnitude comparable to reported values for grating-based SERS substrates[54] and commercial SERS substrates.[30]

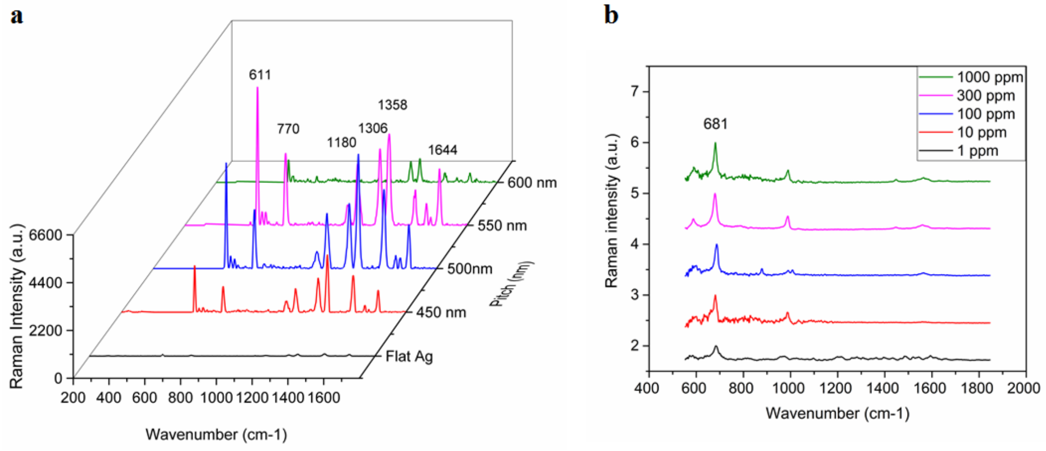

Figure 8.3 Surface-enhanced Raman scattering (SERS) activity of Ag TS-CSRG. (a) Pitch-dependency of SERS spectra for R6G (10^{-5} M) with pitches ranging 450 nm to 600 nm, and for a flat Ag substrate for R6G (10^{-2} M). (b) Average SERS spectra of melamine on Ag TS-CSRG for concentrations ranging from 1 ppm to 1000 ppm.

The TS-CSRG was further evaluated in a real-world detection scenario for the detection of melamine. Melamine is a toxic, nitrogen-rich (66% by mass) chemical used in the plastics industry for the production of compounds for molding, coating, adhesives, and glues. Due to its high nitrogen content, it is illegally added to foodstuffs such as pet food, milk, infant formula to inflate the apparent protein content of the food.[55] Melamine contamination is virtually undetectable by standardized tests as they rely on the amount of nitrogen in test samples as a proxy for the amount of protein. Illegal contamination of dairy products led to severe health problems, resulting in renal failure and even death, with the hospitalization of over 50,000 infants in some cases.[56] The World Health Organization dictates 2.5 ppm (2.0×10^{-5} M) as the maximum residue limit for melamine in milk and 1 ppm (7.9×10^{-6} M) as the maximum residue limit in infant formula.[57] Detection of melamine usually involves laborious, expensive, and time-consuming methods such as HPLC and LC–MS. In spite of the low detection limit of those methods, they involve immovable heavy equipment and sample preprocessing that make them impractical for point-of-use testing. Melamine has a strong characteristic Raman peak associated with the in-plane deformation of the triazine ring peak (around 676–690 cm^{-1}), depending on reaction conditions.[58] This provides an opportunity to allow for the detection of melamine using the Ag TS-CSRG SERS substrate. Melamine in water with concentrations ranging 1 ppm–1000 ppm were drop-casted on the Ag TS-CSRG, followed by SERS spectra acquisition. Figure 8.3b shows the normalized acquired spectra for melamine for the different concentrations. The characteristic Raman peak associated with the in-plane deformation of the triazine ring peak is distinguishable up to 1 ppm, a concentration that is in line with the WHO regulations for melamine in food products. These results demonstrate that the Ag TS-CSRG presented here can be used as an inexpensive, yet effective SERS sensor with a topology that can be customized to transmit or reflect specific light wavelengths, similarly to actual nanostructures in cicada wings, to enable signals tailored to employ and acquire specific wavelengths for sensing.

8.4 Conclusions

In conclusion, this work presents a new Ag TS-CSRG as polarization-independent SERS active substrate, inspired by the tapered nanopillars found in cicada wings. The fabrication of the substrate is cost-effective and achieved in a cleanroom-free environment via holographic exposure followed by a template-stripping step using a UV-curable resin. Inspired by the AR properties of the cicada wings, the nanostructures are strategically designed to minimize the reflection of light for wavelengths smaller than their periodicity, promoting enhanced plasmonic regions for the Raman excitation wavelength at 632.8 nm. AFM scans reveal that the TS-CSRGs possess a remarkable resemblance to the nanostructures in the wings of cicada *Cryptotympana atrata fabricius* and are equally hydrophobic, providing them with potential self-cleaning and bactericidal properties. The nanostructures enable a field enhancement that allows for the sensitive and reproducible SERS detection of R6G. Simulations and experimental investigation of the SPR-assisted electromagnetic enhancement are performed via FDTD and detection of SERS-active dye R6G, respectively, to validate the nanofabrication parameters. More important, the TS-CSRG enables the label-free, sensitive detection of melamine at concentrations compatible with the maximum residue limits allowed by the WHO in food. The fabrication methodology of TS-CSRG allows for the generation of nanostructures with customized periodicities that can be tailored for specific applications. Therefore, the new bio-inspired functional, SERS-active TS-CSRG introduced here holds great promise as large-area, label-free SERS-active substrates for medical and biochemical sensing applications.

8.5 References

(1) Motamedi, M.; Warkiani, M. E.; Taylor, R. A. Transparent Surfaces Inspired by Nature. Adv. Opt. Mater. 2018, 6 (14), 1800091. https://doi.org/https://doi.org/10.1002/adom.201800091.

(2) Yu, K.; Fan, T.; Lou, S.; Zhang, D. Biomimetic Optical Materials: Integration of Nature’s Design for Manipulation of Light. Progress in Materials Science. Elsevier Ltd July 1, 2013, pp 825–873. https://doi.org/10.1016/j.pmatsci.2013.03.003.

(3) Özgür, E.; Parlak, O.; Beni, V.; Turner, A. P. F.; Uzun, L. Bioinspired Design of a Polymer-Based Biohybrid Sensor Interface. Sensors Actuators, B Chem. 2017, 251, 674–682. https://doi.org/10.1016/j.snb.2017.05.030.

(4) Damiati, S.; Peacock, M.; Mhanna, R.; Søpstad, S.; Sleytr, U. B.; Schuster, B. Bioinspired Detection Sensor Based on Functional Nanostructures of S-Proteins to Target the Folate Receptors in Breast Cancer Cells. Sensors Actuators, B Chem. 2018, 267, 224–230. https://doi.org/10.1016/j.snb.2018.04.037.

(5) Gao, B.; He, Z.; He, B.; Gu, Z. Wearable Eye Health Monitoring Sensors Based on Peacock Tail-Inspired Inverse Opal Carbon. Sensors Actuators, B Chem. 2019, 288, 734–741. https://doi.org/10.1016/j.snb.2019.03.029.

(6) Li, Z.; Huang, Z.; Yang, Q.; Su, M.; Zhou, X.; Li, H.; Li, L.; Li, F.; Song, Y. Bioinspired Anti-Moiré Random Grids via Patterning Foams. Adv. Opt. Mater. 2017, 5 (23), 1700751. https://doi.org/10.1002/adom.201700751.

(7) Jin, B.; He, J.; Li, J.; Zhang, Y. Lotus Seedpod Inspired SERS Substrates: A Novel Platform Consisting of 3D Sub-10 Nm Annular Hot Spots for Ultrasensitive SERS Detection. Adv. Opt. Mater. 2018, 6 (13), 1800056. https://doi.org/https://doi.org/10.1002/adom.201800056.

(8) Cronin, T. W. Camouflage: Being Invisible in the Open Ocean. Current Biology. Cell Press November 21, 2016, pp R1179–R1181. https://doi.org/10.1016/j.cub.2016.09.056.

(9) Hasan, J.; Webb, H. K.; Truong, V. K.; Pogodin, S.; Baulin, V. A.; Watson, G. S.; Watson, J. A.; Crawford, R. J.; Ivanova, E. P. Selective Bactericidal Activity of Nanopatterned Superhydrophobic Cicada Psaltoda Claripennis Wing Surfaces. Appl. Microbiol. Biotechnol. 2013, 97 (20), 9257–9262. https://doi.org/10.1007/s00253-012-4628-5.

(10) Large, M. C. J. Optical Biomimetics : Materials and Applications; Woodhead Pub. Ltd, 2012.

(11) Nien, C. K.; Yu, H. H. The Applications of Biomimetic Cicada-Wing Structure on the Organic Light-Emitting Diodes. Mater. Chem. Phys. 2019, 227, 191–199. https://doi.org/10.1016/j.matchemphys.2019.01.059.

(12) Liu, F.; Dong, B.; Liu, X. Bio-Inspired Photonic Structures: Prototypes, Fabrications and Devices. In Optical Devices in Communication and Computation; Peng Xi, Ed.; InTech, 2012. https://doi.org/10.5772/50199.

(13) Han, Z.; Jiao, Z.; Niu, S.; Ren, L. Ascendant Bioinspired Antireflective Materials: Opportunities and Challenges Coexist. Progress in Materials Science. Elsevier Ltd June 1, 2019, pp 1–68. https://doi.org/10.1016/j.pmatsci.2019.01.004.

(14) Kobayashi, M.; Furusawa, T.; Chikuta, T.; Shimojo, M.; Kajikawa, K. Broadband Light Absorber Property of Metal-Coated Pillars on Cicada Wings. Opt. Mater. Express 2019, 9 (7), 2761. https://doi.org/10.1364/ome.9.002761.

(15) Jiwei, Q.; Yudong, L.; Ming, Y.; Qiang, W.; Zongqiang, C.; Wudeng, W.; Wenqiang, L.; Xuanyi, Y.; Jingjun, X.; Qian, S. Large-Area High-Performance SERS Substrates with Deep Controllable Sub-10-Nm Gap Structure Fabricated by Depositing Au Film on the Cicada Wing. Nanoscale Res. Lett. 2013, 8 (1), 1–6. https://doi.org/10.1186/1556-276X-8-437.

(16) Stoddart, P. R.; Cadusch, P. J.; Boyce, T. M.; Erasmus, R. M.; Comins, J. D. Optical Properties of Chitin: Surface-Enhanced Raman Scattering Substrates Based on Antireflection Structures on Cicada Wings. Nanotechnology 2006, 17 (3), 680–686. https://doi.org/10.1088/0957-4484/17/3/011.

(17) Kostovski, G.; White, D. J.; Mitchell, A.; Austin, M. W.; Stoddart, P. R. Nanoimprinted Optical Fibres: Biotemplated Nanostructures for SERS Sensing. Biosens. Bioelectron. 2009, 24 (5), 1531–1535. https://doi.org/10.1016/j.bios.2008.10.016.

(18) Tanahashi, I.; Harada, Y. Silver Nanoparticles Deposited on TiO2-Coated Cicada and Butterfly Wings as Naturally Inspired SERS Substrates. J. Mater. Chem. C 2015, 3 (22), 5721–5726. https://doi.org/10.1039/c5tc00956a.

(19) Nair, S.; Escobedo, C.; Sabat, R. G. Crossed Surface Relief Gratings as Nanoplasmonic Biosensors. ACS Sensors 2017, 2 (3), 379–385. https://doi.org/10.1021/acssensors.6b00696.

(20) Yanik, A. A.; Huang, M.; Kamohara, O.; Artar, A.; Geisbert, T. W.; Connor, J. H.; Altug, H. An Optofluidic Nanoplasmonic Biosensor for Direct Detection of Live Viruses from Biological Media. Nano Lett. 2010, 10 (12), 4962–4969. https://doi.org/10.1021/nl103025u.

(21) Nair, S.; Gomez-Cruz, J.; Manjarrez-Hernandez, Á.; Ascanio, G.; Sabat, R.; Escobedo, C. Selective Uropathogenic E. Coli Detection Using Crossed Surface-Relief Gratings. Sensors 2018, 18 (11), 3634. https://doi.org/10.3390/s18113634.

(22) Li, X.; Soler, M.; Ozdemir, C. I.; Belushkin, A.; Yesilkoy, F.; Altug, H. Plasmonic Nanohole Array Biosensor for Label-Free and Real-Time Analysis of Live Cell Secretion. Lab Chip 2017. https://doi.org/10.1039/C7LC00277G.

(23) Escobedo, C.; Brolo, A. G.; Gordon, R.; Sinton, D. Optofluidic Concentration: Plasmonic Nanostructure as Concentrator and Sensor. Nano Lett. 2012, 12 (3). https://doi.org/10.1021/nl204504s.

(24) Sannomiya, T.; Scholder, O.; Jefimovs, K.; Hafner, C.; Dahlin, A. B. Investigation of Plasmon Resonances in Metal Films with Nanohole Arrays for Biosensing Applications. Small 2011, 7 (12), 1653–1663. https://doi.org/https://doi.org/10.1002/smll.201002228.

(25) Escobedo, C. On-Chip Nanohole Array Based Sensing: A Review. Lab on a Chip. Royal Society of Chemistry July 7, 2013, pp 2445–2463. https://doi.org/10.1039/c3lc50107h.

(26) Nair, S.; Gomez-Cruz, J.; Manjarrez-Hernandez, A.; Ascanio, G.; Sabat, R. G.; Escobedo, C. Rapid Label-Free Detection of Intact Pathogenic Bacteria in Situ via Surface Plasmon Resonance Imaging Enabled by Crossed Surface Relief Gratings. Analyst 2020, 145 (6), 2133–2142. https://doi.org/10.1039/c9an02339a.

(27) Cetin, A. E.; Coskun, A. F.; Galarreta, B. C.; Huang, M.; Herman, D.; Ozcan, A.; Altug, H. Handheld High-Throughput Plasmonic Biosensor Using Computational on-Chip Imaging. Light Sci. Appl. 2014, 3 (1), e122. https://doi.org/10.1038/lsa.2014.3.

(28) Gomez-Cruz, J.; Nair, S.; Manjarrez-Hernandez, A.; Gavilanes-Parra, S.; Ascanio, G.; Escobedo, C. Cost-Effective Flow-through Nanohole Array-Based Biosensing Platform for the Label-Free Detection of Uropathogenic E. Coli in Real Time. Biosens. Bioelectron. 2018, 106. https://doi.org/10.1016/j.bios.2018.01.055.

(29) Escobedo, C.; Chou, Y.-W.; Rahman, M.; Duan, X.; Gordon, R.; Sinton, D.; Brolo, A. G.; Ferreira, J. Quantification of Ovarian Cancer Markers with Integrated Microfluidic Concentration Gradient and Imaging Nanohole Surface Plasmon Resonance. Analyst 2013, 138 (5), 1450. https://doi.org/10.1039/c3an36616b.

(30) Dies, H.; Raveendran, J.; Escobedo, C.; Docoslis, A. In Situ Assembly of Active Surface-Enhanced Raman Scattering Substrates via Electric Field-Guided Growth of Dendritic Nanoparticle Structures. Nanoscale 2017, 9 (23), 7847–7857. https://doi.org/10.1039/C7NR01743J.

(31) Couture, M.; Brulé, T.; Laing, S.; Cui, W.; Sarkar, M.; Charron, B.; Faulds, K.; Peng, W.; Canva, M.; Masson, J.-F. High Figure of Merit (FOM) of Bragg Modes in Au-Coated Nanodisk Arrays for Plasmonic Sensing. Small 2017, 13 (38), 1700908. https://doi.org/10.1002/smll.201700908.

(32) Deng, X.; Braun, G. B.; Liu, S.; Sciortino, P. F.; Koefer, B.; Tombler, T.; Moskovits, M. Single-Order, Subwavelength Resonant Nanograting as a Uniformly Hot Substrate for Surface-Enhanced Raman Spectroscopy. Nano Lett. 2010, 10 (5), 1780–1786. https://doi.org/10.1021/nl1003587.

(33) Fan, M.; Wang, P.; Escobedo, C.; Sinton, D.; Brolo, A. G. Surface-Enhanced Raman Scattering (SERS) Optrodes for Multiplexed on-Chip Sensing of Nile Blue A and Oxazine 720. Lab Chip 2012, 12 (8), 1554–1560. https://doi.org/10.1039/c2lc20648j.

(34) Ahmed, A.; Rushworth, J. V.; Hirst, N. A.; Millner, P. A. Biosensors for Whole-Cell Bacterial Detection. Clin. Microbiol. Rev. 2014, 27 (3), 631–646. https://doi.org/10.1128/CMR.00120-13.

(35) Freedman, K. J.; Crick, C. R.; Albella, P.; Barik, A.; Ivanov, A. P.; Maier, S. A.; Oh, S.-H.; Edel, J. B. On-Demand Surface- and Tip-Enhanced Raman Spectroscopy Using Dielectrophoretic Trapping and Nanopore Sensing. ACS Photonics 2016, 3 (6), 1036–1044. https://doi.org/10.1021/acsphotonics.6b00119.

(36) Chung, A. J.; Huh, Y. S.; Erickson, D. Large Area Flexible SERS Active Substrates Using Engineered Nanostructures. Nanoscale 2011, 3 (7), 2903–2908. https://doi.org/10.1039/C1NR10265F.

(37) Dies, H.; Raveendran, J.; Escobedo, C.; Docoslis, A. Rapid Identification and Quantification of Illicit Drugs on Nanodendritic Surface-Enhanced Raman Scattering Substrates. Sensors Actuators B Chem. 2018, 257, 382–388. https://doi.org/10.1016/J.SNB.2017.10.181.

(38) Brolo, A. G.; Arctander, E.; Gordon, R.; Leathem, B.; Kavanagh, K. L. Nanohole-Enhanced Raman Scattering. Nano Lett. 2004, 4 (10), 2015–2018. https://doi.org/10.1021/nl048818w.

(39) Du, L.; Zhang, X.; Mei, T.; Yuan, X. Localized Surface Plasmons, Surface Plasmon Polaritons, and Their Coupling in 2D Metallic Array for SERS. Opt. Express 2010, 18 (3), 1959. https://doi.org/10.1364/oe.18.001959.

(40) Kalachyova, Y.; Mares, D.; Lyutakov, O.; Kostejn, M.; Lapcak, L.; Švorčík, V. Surface Plasmon Polaritons on Silver Gratings for Optimal SERS Response. J. Phys. Chem. C 2015, 119 (17), 9506–9512. https://doi.org/10.1021/acs.jpcc.5b01793.

(41) Jiao, Y.; Ryckman, J. D.; Koktysh, D. S.; Weiss, S. M. Controlling Surface Enhanced Raman Scattering Using Grating-Type Patterned Nanoporous Gold Substrates. Opt. Mater. Express 2013, 3 (8), 1137. https://doi.org/10.1364/ome.3.001137.

(42) Nagpal, P.; Lindquist, N. C.; Oh, S. H.; Norris, D. J. Ultrasmooth Patterned Metals for Plasmonics and Metamaterials; 2009; Vol. 325. https://doi.org/10.1126/science.1174655.

(43) Hong, K. Y.; Menezes, J. W.; Brolo, A. G. Template-Stripping Fabricated Plasmonic Nanogratings for Chemical Sensing. Plasmonics 2018, 13 (1), 231–237. https://doi.org/10.1007/s11468-017-0503-7.

(44) Setiogi, S.; Matthews, C. WHO | International experts limit melamine levels in food https://www.who.int/mediacentre/news/releases/2010/melamine_food_20100706/en/ (accessed Mar 1, 2020).

(45) Kirby, R.; Sabat, R. G.; Nunzi, J.-M.; Lebel, O. Disperse and Disordered: A Mexylaminotriazine-Substituted Azobenzene Derivative with Superior Glass and Surface Relief Grating Formation. J. Mater. Chem. C 2014, 2 (5), 841–847. https://doi.org/10.1039/C3TC32034K.

(46) Das, G.; Patra, N.; Gopalakrishnan, A.; Zaccaria, R. P.; Toma, A.; Thorat, S.; Di Fabrizio, E.; Diaspro, A.; Salerno, M. Fabrication of Large-Area Ordered and Reproducible Nanostructures for SERS Biosensor Application. Analyst 2012, 137 (8), 1785–1792. https://doi.org/10.1039/c2an16022f.

(47) Johnson, P. B.; Christy, R. W. Optical Constants of the Noble Metals. Phys. Rev. B 1972, 6 (12), 4370–4379. https://doi.org/10.1103/PhysRevB.6.4370.

(48) Xie, H.; Huang, H. X.; Peng, Y. J. Rapid Fabrication of Bio-Inspired Nanostructure with Hydrophobicity and Antireflectivity on Polystyrene Surface Replicating from Cicada Wings. Nanoscale 2017, 9 (33), 11951–11958. https://doi.org/10.1039/c7nr04176d.

(49) Osman, M. A.; Keller, B. A. Wettability of Native Silver Surfaces. Appl. Surf. Sci. 1996, 99 (3), 261–263. https://doi.org/10.1016/0169-4332(96)00101-8.

(50) Giacomello, A.; Meloni, S.; Chinappi, M.; Casciola, C. M. Cassie-Baxter and Wenzel States on a Nanostructured Surface: Phase Diagram, Metastabilities, and Transition Mechanism by Atomistic Free Energy Calculations. Langmuir 2012, 28 (29), 10764–10772. https://doi.org/10.1021/la3018453.

(51) Kirubha, E.; Palanisamy, P. K. Green Synthesis, Characterization of Au-Ag Core-Shell Nanoparticles Using Gripe Water and Their Applications in Nonlinear Optics and Surface

Enhanced Raman Studies. Adv. Nat. Sci. Nanosci. Nanotechnol. 2014, 5 (4), 045006. https://doi.org/10.1088/2043-6262/5/4/045006.

(52) Rahomki, J.; Nuutinen, T.; Karvonen, L.; Honkanen, S.; Vahimaa, P. Horizontal Slot Waveguide Channel for Enhanced Raman Scattering. Opt. Express 2013, 21 (7), 9060. https://doi.org/10.1364/oe.21.009060.

(53) Hildebrandt, P.; Stockhurger, M. Surface-Enhanced Resonance Raman Spectroscopy of Rhodamine 6G Adsorbed on Colloidal Silver. J. Phys. Chem. 1984, 88 (24), 5935–5944. https://doi.org/10.1021/j150668a038.

(54) Ma, P.; Liang, F.; Sun, Y.; Jin, Y.; Chen, Y.; Wang, X.; Zhang, H.; Gao, D.; Song, D. Rapid Determination of Melamine in Milk and Milk Powder by Surface-Enhanced Raman Spectroscopy and Using Cyclodextrin-Decorated Silver Nanoparticles. Microchim. Acta 2013, 180 (11–12), 1173–1180. https://doi.org/10.1007/s00604-013-1059-7.

(55) Betz, J. F.; Cheng, Y.; Rubloff, G. W. Direct SERS Detection of Contaminants in a Complex Mixture: Rapid, Single Step Screening for Melamine in Liquid Infant Formula. Analyst 2012, 137 (4), 826. https://doi.org/10.1039/c2an15846a.

(56) Lin, M.; He, L.; Awika, J.; Yang, L.; Ledoux, D. R.; Li, H.; Mustapha, A. Detection of Melamine in Gluten, Chicken Feed, and Processed Foods Using Surface Enhanced Raman Spectroscopy and HPLC. J. Food Sci. 2008, 73 (8), T129–T134. https://doi.org/10.1111/j.1750-3841.2008.00901.x.

(57) Sabat, R. G.; Rochon, N.; Rochon, P. Dependence of Surface Plasmon Polarization Conversion on the Grating Pitch. J. Opt. Soc. Am. A 2010, 27 (3), 518. https://doi.org/10.1364/JOSAA.27.000518.

(58) Zhang, X.-F.; Zou, M.-Q.; Qi, X.-H.; Liu, F.; Zhu, X.-H.; Zhao, B.-H. Detection of Melamine in Liquid Milk Using Surface-Enhanced Raman Scattering Spectroscopy. J. Raman Spectrosc. 2010, 41 (12), 1655–1660. https://doi.org/10.1002/jrs.2629.

Chapter 9

Volatile Organic Compound Detection Using Silicone-Coated Metallic Flow-Through Nanohole Arrays

This chapter has been prepared as a draft manuscript and has not yet been submitted for publication.

Abstract: Organic contaminants, specifically volatile organic compounds (VOCs), are commonly employed in several industries. Exposure to these compounds over an extended period of time can cause serious health complications. However, the development of a sensitive, reliable, and reproducible sensor is still needed. Here, we present a rapid-fabrication VOC sensing platform that combines the experimental and theoretical quantification of analyte mole fraction. A metallic flow-through plasmonic nanohole array (NHA) coated with a thin layer of PDMS was utilized to measure the uptake and release of xylene into the PDMS in real-time. A mathematical model of the diffusion kinetics of the vapor solvent through the PDMS-NHA structure was developed to fit the experimental data. This approach improved the platform limit of detection (LoD) in two orders of magnitude (LoD = 4.4×10^{-5}) compared to the mole fraction from the experimental detection. The platform exhibited unique potential as a VOC detector, attributed to its low concentration quantification, reproducibility, and miniaturization and portability capabilities.

9.1 Introduction

Organic contaminants, specifically volatile organic compounds (VOCs) such as benzene, toluene, ethylbenzene, and xylenes (BTEX), are frequently employed in several industries, including polymer and plastic production, oil refineries, and paint production. When released, these compounds turn into atmospheric pollutants.[1] Prolonged exposure to high levels of these compounds can cause serious health side effects such as respiratory diseases, reproductive adversities and cancer,[1–3] making the development of an accurate, real-time BTEX sensor necessary.

Since its discovery, the Surface Plasmon Resonance (SPR) phenomenon has been widely explored as an optical sensing technique.[4] Due to its versatility, SPR-based sensing platforms have been used for point-of-care (POC) biosensing,[5,6] and drug[7] and explosive detection.[8] SPR sensors are based on the change in refractive index (RI) at a metal-dielectric interface; upon light excitation, the free electrons on the metal surface create an evanescent wave that travels along the interface, known as surface plasmon polariton (SPP). Periodic metallic nanostructures, such as flow-through nanohole arrays (NHAs), promote the propagation of SPP on the surface and allow for extraordinary optical transmission (EOT) as a consequence of the SPR response.[4,6,9] NHAs can be interrogated in transmission mode, in contrast to spectroscopic reflection interrogation in flat metallic thin films, which offer high sensitivity and the use of collinear optics, which in turn, facilitates the miniaturization and multiplexing of the detection platforms.[10,11] Plasmonic nanohole array sensors for VOC detection have been recently investigated, achieving great portability and high sensitivity. Nonetheless, all the reported methods require a multistep fabrication approach to achieve the reliable detection of VOC.[12,13]

Polydimethylsiloxane (PDMS) is an elastic, chemically inert, hydrophobic polymer with optical transparency in the ultraviolet-visible (UV-Vis) region of light.[14,15] These properties have led to its use in a wide variety of commercial, industrial, and scientific applications. Additionally, the partitioning and permeability properties are extremely useful in the analytical field as a means for solid-phase microextraction (SPME), analyte separation via gas chromatography columns, passive samplers with PDMS membranes, and lab-on-a-chip applications, to name a few.[16] PDMS, like other silicon-based inorganic polymers, bears a strong affinity to non-polar molecules. This allows VOCs to be readily absorbed into the polymer causing physical and chemical changes.[17,18] For instance, the uptake of VOCs into PDMS results in the alteration of its refractive index. The increase or decrease of RI of the polymer is strongly dependent on the VOC optical properties, solvent-polymer affinity, and sorption kinetics.[18,19]

Here, we present a novel VOC sensing approach using metallic flow-through NHAs coated with a thin layer of PDMS. The fabrication of the device is facile, rapid, and cleanroom-free. The sorption kinetics of xylene vapors into a thin layer of PDMS are investigated by measuring the peak-shift of the plasmonic signal upon the change in bulk RI, acquired in transmission mode. Using our expertise in VOC kinetics,[18,20] we developed a mole fraction mathematical model to describe the uptake and release of xylene in the system as a function of time, to determine the diffusion rates of an analyte through the polymer film. This approach enables the development of accurate portable and cost-effective sensing platforms for the detection of VOCs.

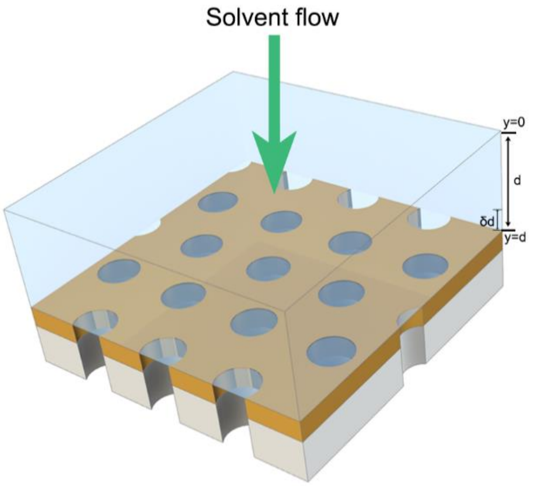

Figure 9.1 Schematic representation (not to scale) of the NHA sensor covered with a thin layer (d = 10 µm) of PDMS. The analyte flows from the PDMS surface (y = 0) to the NHA (y = d). δd corresponds to the maximum amplitude of the evanescent plasmonic wave.

9.2 Materials and Methods

9.2.1 PDMS-coated flowthrough NHAs

The plasmonic flow-through nanohole arrays are fabricated on a Si_3N_4 TEM grid structure (Ted Pella, USA) of 200 nm thickness with an effective sensing area of 500 um x 500 um. Physical vapor deposition (PVD) was used to deposit a 5 nm Cr adhesion layer, followed by 100 nm of Au. The hexagonal lattice of nanoholes has a hole diameter and periodicity of 200 nm and 400 nm, respectively. A 10 µm PDMS film (1:10 weight ratio of curing agent to prepolymer, Dow Corning, MI, USA) was spin-coated on top of the NHA structure.

9.2.2 Experimental setup

A transmission-based optical setup comprises a halogen lamp (Ocean Optics HL-2000, USA) as a light source, a collimating array including a 10x objective lens and a biconvex lens. The collimated light beam diameter was restricted through an iris and directed on top of the NHA structure. The transmitted light spectra, coming from the NHA, was captured by a UV-Vis spectrometer (Ocean Optics, USB4000, USA). The PDMS-NHA structure was enclosed in a 3D printed custom-made chamber that allows the transmission of light through the center of the chamber and allows for the gases to flow on top of the PDMS-NHA structure. The chamber was connected to a flow meter to regulate and maintain a constant flow rate of 230 sccm of gas. Xylene saturated in nitrogen gas, produced by flowing nitrogen into a glass container filled with xylene solvent, was used for absorption measurements, and pure nitrogen gas was used for desorption measurements.

9.2.3 FDTD simulations

Three-dimensional finite-difference time-domain simulation (Lumerical FDTD Solutions) was used to simulate the near-field electromagnetic field distribution. Simulations under S and P polarizations were recorded and added to emulate the plasmonic response of the PDMS-NHA structures under a quasi-unpolarized broadband excitation light source. Due to the periodicity of the hexagonal lattice of the NHAs, a unit cell of the structure was used with symmetric and antisymmetric boundary conditions set for the x- and y directions, respectively, and a perfect matched layer (PML) in the *z*-direction. A uniform mesh size of 3 nm was used for the nanostructure envelope, comprising the Si_3N_4, the chromium and gold films, and the PDMS layer. A time-averaged electric field intensity distribution, normalized with respect to the incident plane wave $|E / E_0|^2$, was calculated for the structure. The dielectric permittivity used in the simulations for the PDMS and gold were obtained from the manufacturer and the literature, respectively.[21]

9.3 Results and Discussion

9.3.1 FDTD Model

Figure 9.1 shows the schematic representation of the sensing structure comprised of the hexagonal plasmonic NHA, cover with a 10 µm PDMS layer. A hexagonal-lattice was preferred since it reduces the cross-talk between resonance peaks compare to conventional square-lattices.[22,23]

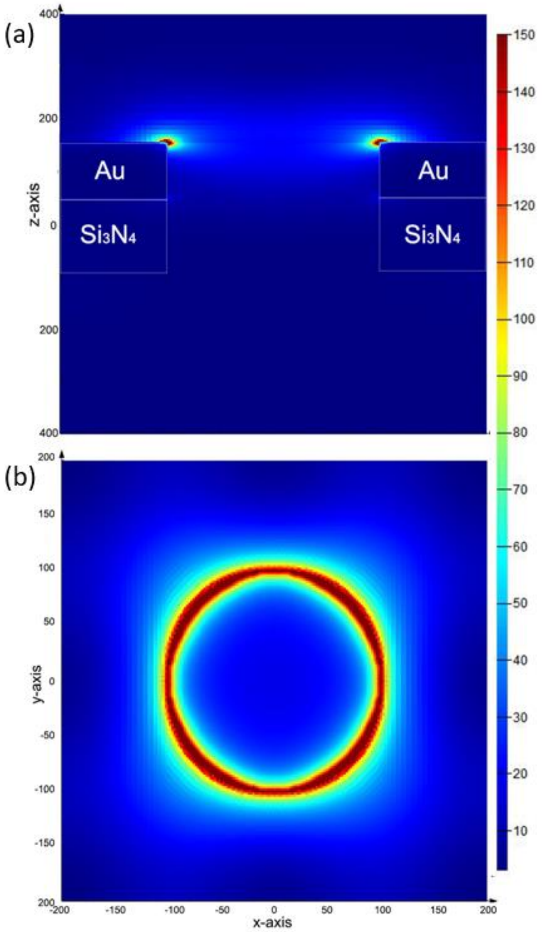

Figure 9.2 FDTD simulations showing the electric field intensity distribution around the rim of the NHA since these regions are the most sensitive to changes in RIs. The response was mapped at λ = 680 nm (a) cross-section. (b) x-y plane.

Calculations and Finite-Difference Time-Domain (FDTD) simulations were performed to predict the plasmonic response of the PDMS-NHA system. The simulated EOT maxima occurred at a wavelength of 680 nm. Figures 9.2 a and b show the electric field (e-field) intensity distribution at the interface of the NHAs and the PDMS layer. Unpolarized incident light was emulated using 0° and 90° polarization. Outstanding electric field enhancement, confined at the PDMS-gold interface, was observed on the rim of the nanoholes at a wavelength of 680 nm. Additionally, the penetration depth of the plasmonic wave into the PDMS (region sensitive to changes in RI) was calculated to be ~100 nm, and this was confirmed by simulations shown in Figure 9.2a.

9.3.2 VOC detection with PDMS-coated flow-through NHAs

The xylene sorption measurements were performed utilizing the setup shown in Figure 9.3. The spectral response of the PDMS-NHAs was recorded for 110 minutes, obtaining spectra measurements every 20 seconds. No solvent was flowed over the first 10 minutes to obtain a baseline signal. Xylene gas was flowed and absorbed into the PDMS for the next 50 minutes, followed by nitrogen gas to desorb the xylene over the subsequent 50 minutes. A set of raw data from a full experiment is presented in Figure 9.4a. The spectral response from the NHA shows a transmission from around 600 nm to 750 nm. However, it can be observed that the most sensitive region falls around 680 nm, which is consistent with the simulations. Tracking of the signal shift, due to the change in refractive index, was performed by the centroid method.[24,25] This method accounts for the change in the center of mass of the desired region of the signal. This method is preferred when the biggest change does not occur in the maxima or minima of the signal. All the experiments were analyzed using a custom MATLAB code that calculates the centroid of every spectra at the upper 75% of the signal. Figure 9.4b shows the centroid shifting over time, as a consequence of the RI change in the PDMS film, upon xylene absorption and desorption.

The characterization of the NHAs to changes in the bulk refractive index was performed by changing the volume percent of dimethyl sulfoxide (*DMSO RI*, $n = 1.473$) in water from 20% to 70%. This provides an RI change from $\eta = 1.3655$ to $\eta = 1.444$, which is within the range of the PDMS RI ($n = 1.427$).[26] The linear fitting provides a sensitivity of 241.5 nm/RIU (refractive index units), Figure 9.4a inset. This characterization was utilized to estimate the RI change during the sorption experiments.

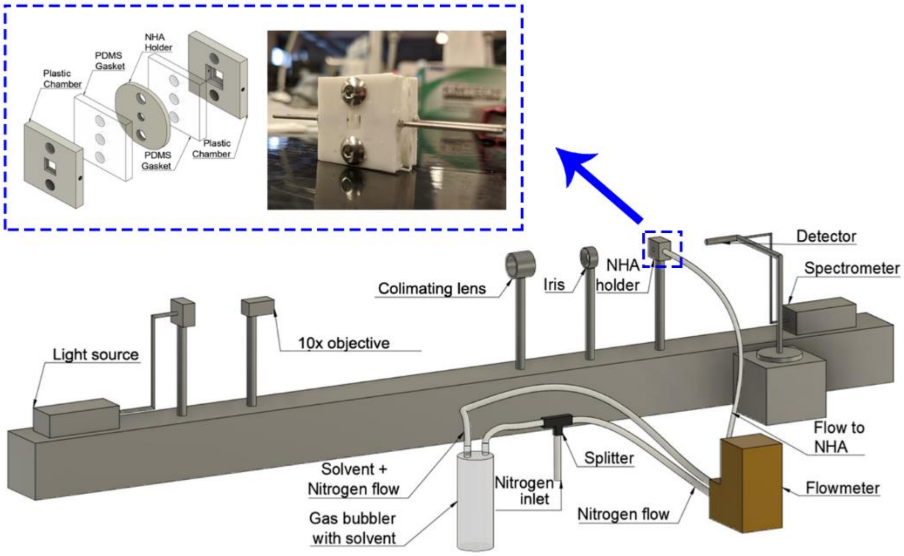

Figure 9.3 Schematic representation (not to scale) of the experimental setup for VOC sorption measurements. Xylene vapours were generated in a glass bubbler by flowing nitrogen gas to generate saturated solvent vapours. Saturated vapours and pure nitrogen were directed to the chamber containing the NHA (inset) for absorption and desorption experiments, respectively. Inset: photograph and schematic of the chamber containing the NHA.

9.3.3 Mole fraction model

The experimental mole fraction concentration of the xylene diffused in the PDMS was calculated using Equation 9.1 from our previously reported method:[18]

$$(t) = \frac{P_{PDMS} - P_{PDMS}\left(\frac{n_{PDMS}^2 + 2}{n_{PDMS}^2 - 1}\right)\left(\frac{n_{mix}^2(\mathrm{t}) - 1}{n_{mix}^2(\mathrm{t}) + 2}\right)\left(1 + \frac{\Delta d}{d}\right)}{P_{PDMS} - P_{PDMS}\left(\frac{n_{PDMS}^2 + 2}{n_{PDMS}^2 - 1}\right)\left(\frac{n_{mix(\mathrm{t})}^2 - 1}{n_{mix(\mathrm{t})}^2 + 2}\right)\left(1 + \frac{\Delta d}{d}\right) - P_{Xyl}} \tag{9.1}$$

where P_i is the molar polarization of the PDMS and xylene, n_{PDMS} the RI of the PDMS film before absorption and n_{mix} is the measured RI during sorption. The molar polarization was determined with:

$$P_i = \left(\frac{n_i^2 - 1}{n_i^2 + 2}\right)\left(\frac{M_i}{\rho_\mathrm{i}}\right) \tag{9.2}$$

where M_i is the molar mass and ρi is the density. The experiments performed in this work assumed a zero swelling from the film ($\Delta d = 0$). Although it is known that PDMS can swell, up to 50%, after 72 hours of exposure in a saturated xylene atmosphere,[17] Saunders et al.[18] suggested a two-step PDMS absorption mechanism of VOCs. Upon exposure, the analytes rapidly fill the PDMS pores causing a change in RI without significant volume changes; over time, the analyte is fully incorporated into the film, causing swelling. Additionally, our experiments did not expose the PDMS to xylenes for longer than 1 hour.

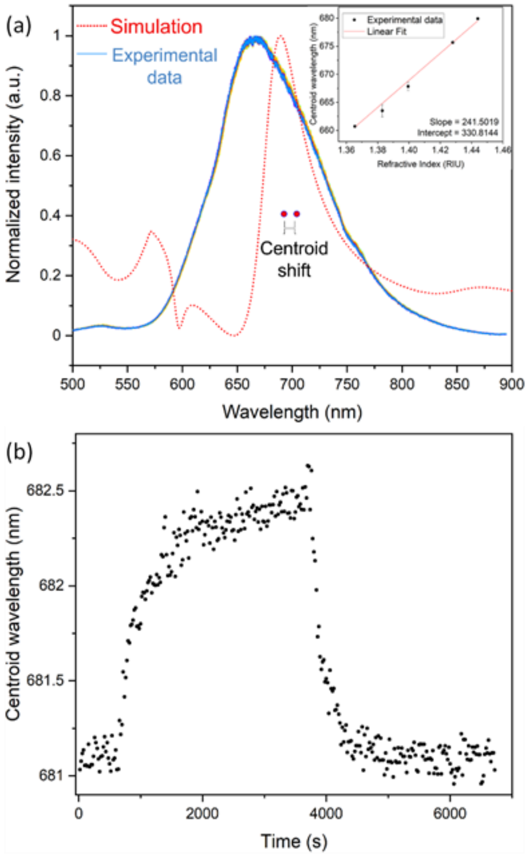

Figure 9.4 (a) Comparison between simulated (dotted red line) and experimental spectra (solid blue line). The transmission spectrum shift was performed by tracking the centroid of the signal, which lies within the simulation maxima

range. Inset: characterization curve of the sensor utilized to calculate the RI changes of the xylene sorption into the PDMS. (b) Centroid wavelength change over time for xylene sorption experiments.

The analyte migration into a polymer can be modelled by a Fickian diffusion mechanism when the temperatures are well above the glass transition temperature of the polymer.[27] Since PDMS glass transition temperature is Tg = -123°C,[28] a Fickian model can be used to describe analyte diffusion at room temperature. The PDMS layer on the surface is considerably thin compared to its lateral extension, and the hole diameter is orders of magnitude smaller than the film thickness. Therefore, the problem was analyzed as one-dimensional diffusion through a plane of finite thickness within an infinite reservoir of analyte on one side with either an impenetrable wall or zero concentration on the other side.

Based on Crank's solutions for a one-dimensional diffusion problem,[29] we mathematically described the sorption kinetics of a thin PDMS film supported by an array of nanoholes. The total analyte concentration accounts for the linear combination of the time-dependent mathematical expressions, describing an average mole fraction of the analyte over the near metal-film interface through a supported membrane (SM), $\bar{\boldsymbol{X}}_{\boldsymbol{SM}}$, and a free-standing membrane (FSM), $\bar{\boldsymbol{X}}_{\boldsymbol{FSM}}$. Both cases were applied for absorption (abs) in Equations 9.3 and 9.4 and desorption (des) in Equations 9.5 and 9.6:

$$\bar{X}_{SM\_abs} = X_{\infty}\left[1 - \frac{8d}{\pi^2 \delta y}\sum_{i=0}^{\infty}\frac{(-1)^i}{(2i+1)^2}\exp\left(-\frac{D(t-t_0)(2i+1)^2\pi^2}{4d^2}\right)\times \sin\left(\frac{(2i+1)\pi\delta y}{2d}\right)\right] \quad (9.3)$$

$$\bar{X}_{FSM\_abs} = X_{\infty}\left[\left(\frac{\delta y}{2d}\right) + \left(\frac{2d}{\pi^2 \delta y}\right)\sum_{i=1}^{\infty}\frac{(-1)^i}{i^2}exp\left(-\frac{D(t-t_0)i^2\pi^2}{d^2}\right)\times\left(1 - cos\left(\frac{i\pi\delta y}{d}\right)\right)\right] \quad (9.4)$$

$$\bar{X}_{SM\_des} = X_{\infty}\left[\frac{8d}{\pi^2 \delta y}\sum_{i=0}^{\infty}\frac{(-1)^i}{(2i+1)^2}exp\left(-\frac{D(t-t_0)(2i+1)^2\pi^2}{4d^2}\right)\times sin\left(\frac{(2i+1)\pi\delta y}{2d}\right)\right] \quad (9.5)$$

$$\bar{X}_{FSM\_des} = X_{\infty}\left[-\left(\frac{2d}{\pi^2 \delta y}\right)\sum_{i=1}^{\infty}\frac{(-1)^i}{i^2}exp\left(-\frac{D(t-t_0)i^2\pi^2}{d^2}\right)\times\left(1 - cos\left(\frac{i\pi\delta y}{d}\right)\right)\right] \quad (9.6)$$

where X_∞ is the equilibrium mole fraction in the film, D is the diffusion coefficient (calculated from the experimental fitting from Equation 9.7), d is the film thickness (10 µm), and δ_y is the effective amplitude of the evanescent plasmonic wave into the PDMS (100 nm). The total sensing area is 2.025×10^5 µm^2, and the nanoholes, representing the FSM, account for 3.976×10^4 µm^2 or 19.6% of the total area. Therefore, the linear combination representing the total solvent mole fraction is:

$$\bar{X} = (0.804)(\bar{X}_{sm}) + (0.196)\left(\bar{X}_{fsm}\right) \tag{9.7}$$

Figure 9.5a shows the experimental data in combination with the mathematical fitting utilizing Equations 9.3-9.7 for the xylene uptake and release into the PDMS. Equation 9.7 was a good approximation to the experimental data, supported by the residual plot (Figure 9.5b). Additionally, the limit of detection (LoD)[30] of 1.5×10^{-3} from the raw data was improved to 4.4×10^{-5} by the fitting method. Reproducibility among experiments was achieved for both experimental and mathematical fitting (Figure 9.5c).

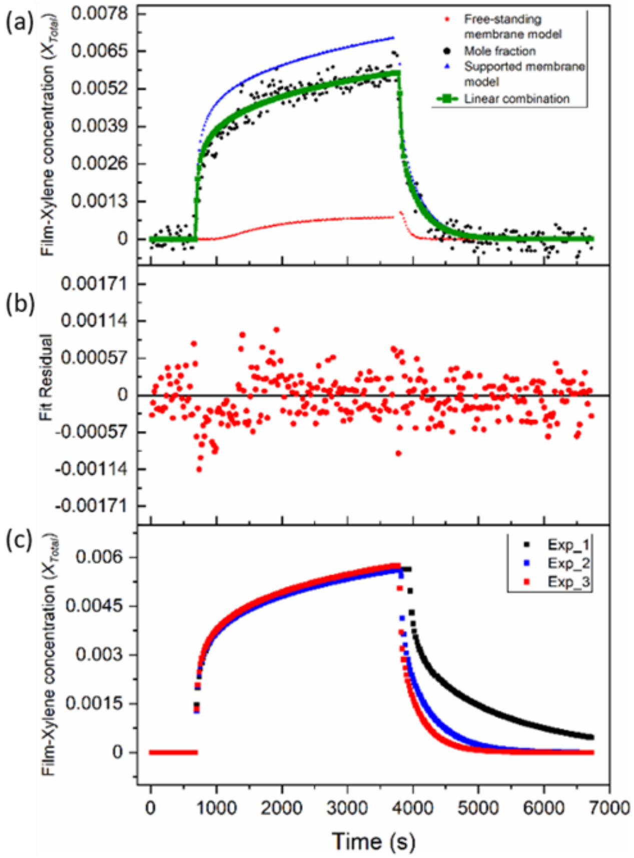

Figure 9.5 (a). Comparison between the experiment mole fraction values (black dots), and the mathematical fitting under a free-standing membrane model (red stars), supported membrane model (blue triangles), and the linear combination of both models (green squares) (b) Residuals corresponding to the mathematical model approximation and the experimental data. (c) Comparison of the mathematical model fitting corresponding to three different experiments performed under the same conditions.

9.4 Conclusions

In summary, we have presented the first experimental and analytical demonstration of the detection and quantification of VOC concentration in a PDMS thin film on a plasmonic flow-through nanohole array structure. With a bulk sensitivity of 241.5 nm/RIU, the sensing platform allows for the detection of the mole fraction of xylene vapors using the RI change in the PDMS layer. The implementation of a mathematical model for fitting the experimental data reduced the

LoD by two orders of magnitude to a mole fraction value of 4.4×10^{-5}. This platform exhibits great potential as a VOC sensor not only because of low concentration quantification, reproducibility, and the closeness of the experimental data with the mathematical model but also because it permits miniaturization, portability, and the possibility of detecting multiple solvent vapors by characterizing their sorption kinetics for each individual solvent.

9.5 References

(1) Montero-Montoya, R.; López-Vargas, R.; Arellano-Aguilar, O. Volatile Organic Compounds in Air: Sources, Distribution, Exposure and Associated Illnesses in Children. Ann. Glob. Heal. 2018, 84 (2), 225–238. https://doi.org/10.29024/aogh.910.

(2) Saunders, J. Refractometry Studies of the Optical Properties of Polymer Films and the Development of Polymer Coated Refractive Index Sensors, Queen’s University, 2016.

(3) Masekameni, M.; Moolla, R.; Gulumian, M.; Brouwer, D. Risk Assessment of Benzene, Toluene, Ethyl Benzene, and Xylene Concentrations from the Combustion of Coal in a Controlled Laboratory Environment. Int. J. Environ. Res. Public Health 2018, 16 (1), 95. https://doi.org/10.3390/ijerph16010095.

(4) Ebbesen, T. W.; Lezec, H. J.; Ghaemi, H. F.; Thio, T.; Wolff, P. A. Extraordinary Optical Transmission through Sub-Wavelenght Hole Arrays. Nature 1998, 391 (6668), 667–669. https://doi.org/10.1038/35570.

(5) Gomez, J.; Nair, S.; Ascanio, G.; Escobedo, C.; Gomez-Cruz, J.; Nair, S.; Ascanio, G.; Escobedo, C. Flow-through Nanohole Array Based Sensor Implemented on Analogue Smartphone Components; Tanaka, T., Tsai, D. P., Eds.; SPIE-Intl Soc Optical Eng, 2017; Vol. 10346, p 80. https://doi.org/10.1117/12.2272433.

(6) Gomez-Cruz, J.; Nair, S.; Manjarrez-Hernandez, A.; Gavilanes-Parra, S.; Ascanio, G.; Escobedo, C. Cost-Effective Flow-through Nanohole Array-Based Biosensing Platform for the Label-Free Detection of Uropathogenic E. Coli in Real Time. Biosens. Bioelectron. 2018, 106 (January), 105–110. https://doi.org/10.1016/j.bios.2018.01.055.

(7) Wang, J.; Yao, W.; Meng, F.; Wang, P.; Wu, Y.; Wang, B. A Surface Plasmon Resonance Immunoassay for the Rapid Analysis of Methamphetamine in Forensic Oral Fluid. J. Clin. Lab. Anal. 2019, 33 (9). https://doi.org/10.1002/jcla.22993.

(8) Wang, J.; Muto, M.; Yatabe, R.; Onodera, T.; Tanaka, M.; Okochi, M.; Toko, K. Rational Design of Peptide-Functionalized Surface Plasmon Resonance Sensor for Specific Detection of TNT Explosive. Sensors 2017, 17 (10), 2249. https://doi.org/10.3390/s17102249.

(9) Rodrigo, S. G.; De León-Pérez, F.; Martín-Moreno, L. Extraordinary Optical Transmission: Fundamentals and Applications. Proc. IEEE 2016, 104 (12), 2288–2306. https://doi.org/10.1109/JPROC.2016.2580664.

(10) Escobedo, C. On-Chip Nanohole Array Based Sensing: A Review. Lab on a Chip. Royal Society of Chemistry July 7, 2013, pp 2445–2463. https://doi.org/10.1039/c3lc50107h.

(11) Ferreira, J.; Santos, M. J. L.; Rahman, M. M.; Brolo, A. G.; Gordon, R.; Sinton, D.; Girotto, E. M. Attomolar Protein Detection Using In-Hole Surface Plasmon Resonance. J. Am. Chem. Soc. 2009, 131 (2), 436–437. https://doi.org/10.1021/ja807704v.

(12) Du, B.; Ruan, Y.; Ly, T. T.; Jia, P.; Sun, Q.; Feng, Q.; Yang, D.; Ebendorff-Heidepriem, H. MoS2-Enhanced Epoxy-Based Plasmonic Fiber-Optic Sensor for Selective and Sensitive Detection of Methanol. Sensors Actuators, B Chem. 2020, 305 (November 2019), 127513. https://doi.org/10.1016/j.snb.2019.127513.

(13) Zhao, Y.; Mukherjee, K.; Benkstein, K. D.; Sun, L.; Steffens, K. L.; Montgomery, C. B.; Guo, S.; Semancik, S.; Zaghloul, M. E. Miniaturized Nanohole Array Based Plasmonic Sensor for the Detection of Acetone and Ethanol with Insights into the Kinetics of Adsorptive Plasmonic Sensing. Nanoscale 2019, 11 (24), 11922–11932. https://doi.org/10.1039/c9nr03578h.

(14) Mata, A.; Fleischman, A. J.; Roy, S. Characterization of Polydimethylsiloxane (PDMS) Properties for Biomedical Micro/Nanosystems. Biomed. Microdevices 2005, 7 (4), 281–293. https://doi.org/10.1007/s10544-005-6070-2.

(15) Stankova, N. E.; Atanasov, P. A.; Nikov, R. G.; Nikov, R. G.; Nedyalkov, N. N.; Stoyanchov, T. R.; Fukata, N.; Kolev, K. N.; Valova, E. I.; Georgieva, J. S.; Armyanov, S. A. Optical Properties of Polydimethylsiloxane (PDMS) during Nanosecond Laser Processing. Appl. Surf. Sci. 2016, 374, 96–103. https://doi.org/10.1016/j.apsusc.2015.10.016.

(16) Seethapathy, S.; Górecki, T. Applications of Polydimethylsiloxane in Analytical Chemistry: A Review. Anal. Chim. Acta 2012, 750, 48–62. https://doi.org/10.1016/j.aca.2012.05.004.

(17) Rumens, C. V.; Ziai, M. A.; Belsey, K. E.; Batchelor, J. C.; Holder, S. J. Swelling of PDMS Networks in Solvent Vapours; Applications for Passive RFID Wireless Sensors. J. Mater. Chem. C 2015, 3 (39), 10091–10098. https://doi.org/10.1039/C5TC01927C.

(18) Saunders, J. E.; Chen, H.; Brauer, C.; Clayton, M.; Loock, H.-P. P. Two Distinct Mechanisms upon Absorption of Volatile Organic Compounds into Siloxane Polymers. Soft Matter 2018, 14 (12), 2206–2218.

(19) Howley, R.; MacCraith, B. D.; O'Dwyer, K.; Masterson, H.; Kirwan, P.; McLoughlin, P. Determination of Hydrocarbons Using Sapphire Fibers Coated with Poly(Dimethylsiloxane). Appl. Spectrosc. 2003, 57 (4), 400–406. https://doi.org/10.1366/00037020360625934.

(20) Saunders, J. E.; Chen, H.; Brauer, C.; Clayton, M.; Chen, W.; Barnes, J. A.; Loock, H. P. Quantitative Diffusion and Swelling Kinetic Measurements Using Large-Angle

Interferometric Refractometry. Soft Matter 2015, 11 (45), 8746–8757. https://doi.org/10.1039/c5sm02170g.

(21) Johnson, P. B.; Christy, R. W. Optical Constants of the Noble Metals. Phys. Rev. B 1972, 6 (12), 4370–4379. https://doi.org/10.1103/PhysRevB.6.4370.

(22) Xu, T.; Shi, H.; Wu, Y. K.; Kaplan, A. F.; Ok, J. G.; Guo, L. J. Structural Colors: From Plasmonic to Carbon Nanostructures. Small 2011, 7 (22), 3128–3136. https://doi.org/10.1002/smll.201101068.

(23) Jia, P.; Yang, J. A Plasmonic Optical Fiber Patterned by Template Transfer as a High-Performance Flexible Nanoprobe for Real-Time Biosensing. Nanoscale 2014, 6 (15), 8836–8843. https://doi.org/10.1039/c4nr01411a.

(24) Piliarik, M.; Homola, J. Surface Plasmon Resonance (SPR) Sensors: Approaching Their Limits? Opt. Express 2009, 17 (19), 16505. https://doi.org/10.1364/oe.17.016505.

(25) Soler, M.; Belushkin, A.; Cavallini, A.; Kebbi-Beghdadi, C.; Greub, G.; Altug, H. Multiplexed Nanoplasmonic Biosensor for One-Step Simultaneous Detection of Chlamydia Trachomatis and Neisseria Gonorrhoeae in Urine. Biosens. Bioelectron. 2017, 94, 560–567. https://doi.org/10.1016/j.bios.2017.03.047.

(26) Schneider, F.; Draheim, J.; Kamberger, R.; Wallrabe, U. Process and Material Properties of Polydimethylsiloxane (PDMS) for Optical MEMS. Sensors Actuators, A Phys. 2009, 151 (2), 95–99. https://doi.org/10.1016/j.sna.2009.01.026.

(27) Wang, X. D.; Wolfbeis, O. S. Fiber-Optic Chemical Sensors and Biosensors (2013-2015). Analytical Chemistry. American Chemical Society January 5, 2016, pp 203–227. https://doi.org/10.1021/acs.analchem.5b04298.

(28) Lambeck, P. V. Integrated Optical Sensors for the Chemical Domain. Measurement Science and Technology. Institute of Physics Publishing August 1, 2006, p R93. https://doi.org/10.1088/0957-0233/17/8/R01.

(29) Crank, J.; Crank, E. P. J. The Mathematics of Diffusion; Oxford science publications; Clarendon Press, 1979.

(30) Armbruster, D. A.; Pry, T. Limit of Blank, Limit of Detection and Limit of Quantitation. Clin. Biochem. Rev. 2008, 29 Suppl 1 (Suppl 1), S49-52.

Chapter 10

Conclusions and future work

10.1 Conclusions

This dissertation focused on the design and development of novel plasmonic metallic nanostructures and their implementation on SPR-based POC platforms. Metallic NHAs and CSRGs were studied and characterized by predicting their plasmonic behavior through theory and FDTD simulations. Subsequently, fabrication and experimentation allowed for the assessment of their potential in detecting molecules and biological analytes. NHAs and CSRGs demonstrated an excellent sensing capability and successful integration with other fields such as electronics, optics, and microfluidics.

In this work, gold-coated flow-through NHAs were investigated and implemented in a miniaturized SPRi-biosensing platform. The spectral plasmonic response in transmission mode and the electric field distribution of the NHAs were analyzed for different periodicities, hole sizes, and RI changes at the metal-dielectric interface. A miniaturized transmission-based optical assembly in conjugation with portable electronics was built to promote SPR in the NHAs and analyze their response. The platform was employed for the detection of real-time changes in the local RI. The platform was also evaluated as a proof-of-concept biosensing assay for the rapid detection of uropathogenic bacteria, demonstrating the potential of this platform for label-free detection in a real-world application. The portable and cost-effective platform allowed for the detection of intact UPEC in clinically relevant concentrations. The experimental detection limit was 2-orders of magnitude lower than the clinical limit for UTI diagnosis. Additionally, the platform demonstrated the detection of UPEC spiked in human urine with high specificity without the necessity of any pre-treatment.

Flow-through NHAs were also demonstrated for the detection of VOCs using their spectroscopic capabilities. By coating the metallic NHAs with a thin layer of a silicone-based polymer such as PDMS, the change in RI of the PDMS was measured in real-time as a result of the uptake and release of xylene vapors. This approach also enabled the development of a mathematical model of the diffusion kinetics of the vapor solvent through the PDMS-NHA structure to fit the experimental data.

CSRG metallic structures were also investigated using FDTD simulations and experimental approaches for various periodicities, materials, and RI at the metal-dielectric interface. Our group has previously demonstrated the potential of the CSRGs as an SPR biosensor in a transmission fashion, taking advantage of the SPR polarization conversion in CSRGs. A smart-phone compatible miniaturized and cost-effective optical platform was developed for the spectroscopic detection of uropathogenic *E. coli,* achieving a detection comparable to the clinical limit for UTI diagnosis. Inspired by CSRG biosensing capabilities, an SPRi-based platform consisting of a narrow band LED, and a CMOS was employed to detect intact uropathogenic bacteria in PBS and urine. Detection of concentrations spanning 6-orders of magnitude was performed in real-time, including clinically relevant concentrations of the pathogen.

A novel, bioinspired cicada wing-like SERS substrate was developed using a template-stripped CSRG (TS-CSRG) structure. Inspired by the antireflective properties of the cicada wings and the unique plasmonic enhancement of CSRGs, the structures were strategically designed for Raman excitation wavelength at 632.8 nm. Nanofabrication parameters were evaluated through FDTD simulations, and fabricated nanostructures were tested using R6G. TS-CSRGs also achieved a label-free melamine detection up to 1 ppm, which is the maximum concentration of the contaminant in food permitted by the World Health Organization.

10.2 Future work

There are many opportunities to improve the plasmonic structures and the POC platforms presented in this dissertation. Flexible plasmonic sensors based on NHAs and CSRGs are currently being investigated due to their potential to detect analytes in complex surfaces such as human skin. The combination of plasmonic nanostructures with a complex multi-layer microfluidic platform will allow for countless lab-on-a-chip applications where analytes can be selectively delivered for multiplexed SPR detection. Functionalization chemistry and techniques can be improved to increase the longevity of the sensor, especially for commercialization purposes. Finally, the decoration of NHAs and CSRGs with nanoparticles can be explored to improve the SERS substrate enhancement factor. Many nanoparticle shapes and materials can be utilized under different Raman excitation wavelengths for innumerous applications involving the detection and quantification of molecules and living cells.

Appendix A

Supplementary information to Chapter 3

With minor changes to fulfill formatting requirements, this Appendix is substantially as it appears as supplementary Information in: Juan Gomez-Cruz, Srijit Nair, Angel Manjarrez-Hernandez, Sandra Gavilanes Parra, Gabriel Ascanio and Carlos Escobedo. Biosensors and Bioelectronics, 2018, 106, 105-110.

Dot blot immunoassay

Bacterial detection was carried out according to the method described by Harlow and Lane,[1] 1988 but with some modifications. Briefly, 3 μl of concentrations of 105 cells diluted in PBS were spotted onto a nitrocellulose membrane. The spots were dried and the membrane was blocked with a blocking solution (5% wt/vol nonfat dry milk, 0.2% Tween 20 and 0.02% sodium azide in PBS) for 1 hour under agitation, washed with PBS containing 0.2% Tween 20, and incubated for 2 hours with 1:100 dilution of the rabbit antibodies against *E. coli*. Following three washes with PBS, the membranes were incubated with a 1:5000 dilution of horseradish peroxidase-conjugated anti-rabbit IgG and the reaction was visualized with 4-chloro-1-naphthol.

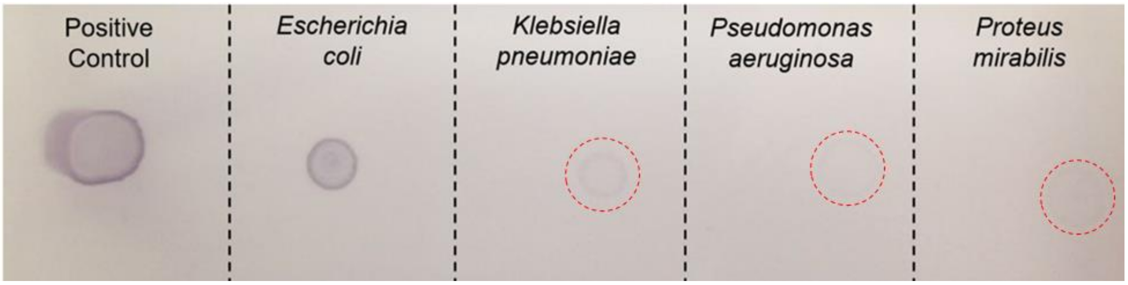

Figure A.1 Dot blot anti-E. coli Ab affinity immunoassay results for the Gram-negative bacteria uropathogenic *E. coli* (UPEC), *Klebisella pneumonia*, *Pseudomonas aeruginosa*, and *Proteus mirabilis* (red dashed circles facilitate the view of the dots of the last three).

Table A.1 Relative intensity-based quantification of dot blot immunoassay using ImageJ software.

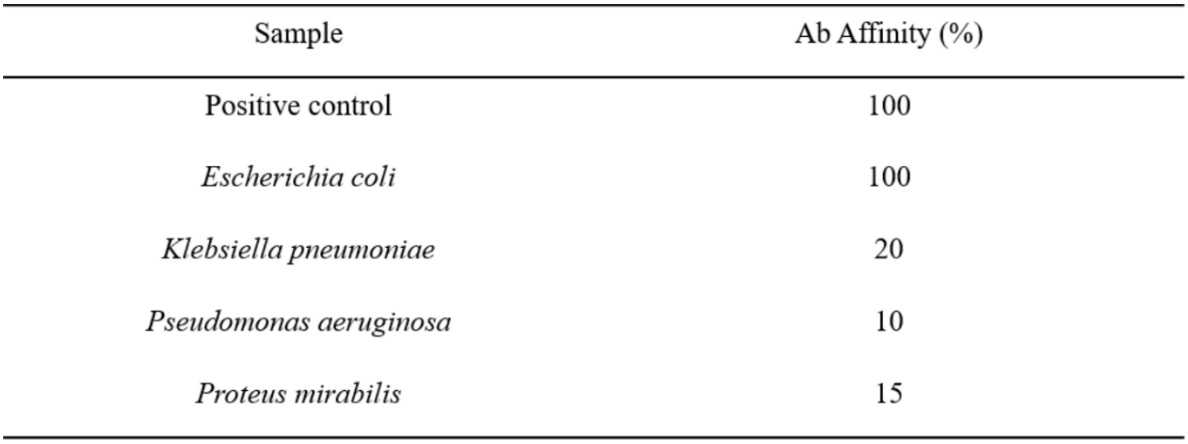

Sample	Ab Affinity (%)
Positive control	100
Escherichia coli	100
Klebsiella pneumoniae	20
Pseudomonas aeruginosa	10
Proteus mirabilis	15

References

(1) Harlow D., E. L. A Laboratory Manual; Cold Spring Harbor Laboratory, 1988. https://doi.org/10.1016/0968-0004(89)90307-1.

Appendix B

Supplementary information to Chapter 4

With minor changes to fulfill formatting requirements, this Appendix is substantially as it appears as supplementary Information in: Srijit Nair, Juan Gomez-Cruz, Ángel Manjarrez-Hernandez, Gabriel Ascanio, Ribal Georges Sabat and Carlos Escobedo. *Sensors* **2018**, *18*(11), 3634.

SPR peak drift experiments

Experiments were performed to determine any potential drift of the acquired signal when using DI water and PBS solutions as test samples. A thin PDMS slab (2 cm × 2 cm) with an 8 mm × 8 mm chamber was placed on the CSRGs, in order to allow liquid-metal contact. The liquid in the chamber (~140 µl) was covered with a cover slip to eliminate any potential lensing effects and diminish evaporation. Transmitted signal from the CSRGs were acquired for 20 minutes, with 30-seconds intervals between each acquisition. As shown in Figures B.1 and B.2, no considerable drift in the SPR signal was observed over the 20 minutes, for both DI water and PBS solution. A cysteamine-biotin-streptavidin assay, as reported elsewhere [1], was also performed in order to tabulate the potential drift associated with respect to binding of analytes and biomolecules on the CSRGs surface, akin to the bacterial detection presented in the article. A streptavidin solution (800 nM) was incubated atop a cysteamine-biotin complex immobilized on the surface of the CSRGs and the system was allowed to reach quasi-steady state. The signal from the system was acquired for 20 minutes, with 1-minute interval between each acquisition, as shown in Figure B.3. The signal was quite stable over the lapse of the experiment and no significant drift was observed.

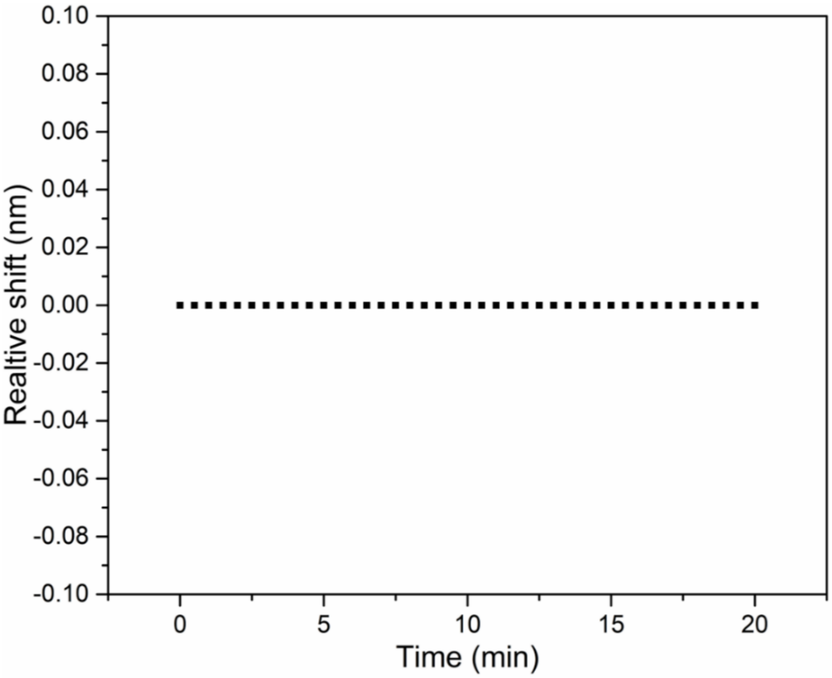

Figure B.1 Relative shift in SPR peak recorded for water from t = 0 min to t = 20 minutes, with 30-seconds interval between signal acquisition.

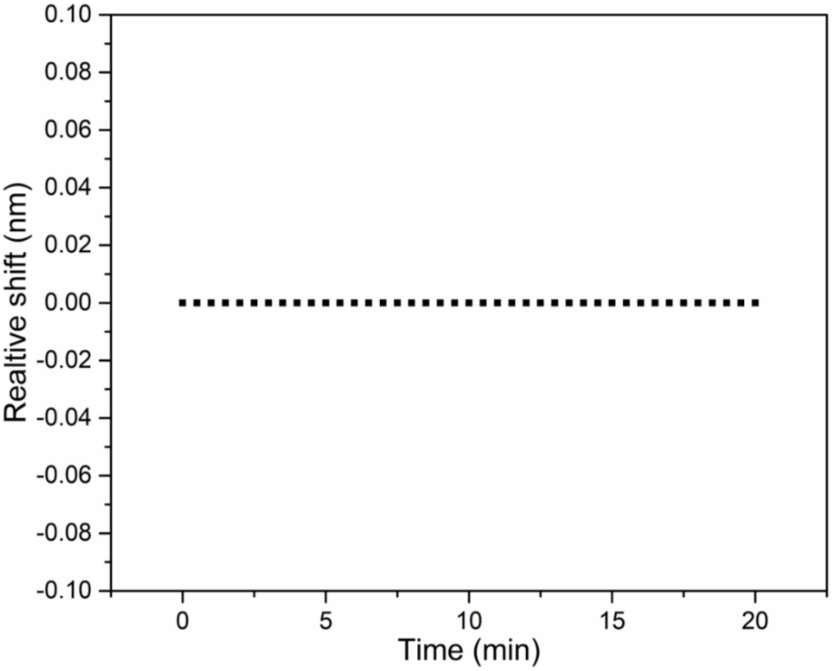

Figure B.2 Relative shift in SPR peak recorded for PBS solution from t = 0 min to t = 20 minutes, with 30-seconds interval between signal acquisition.

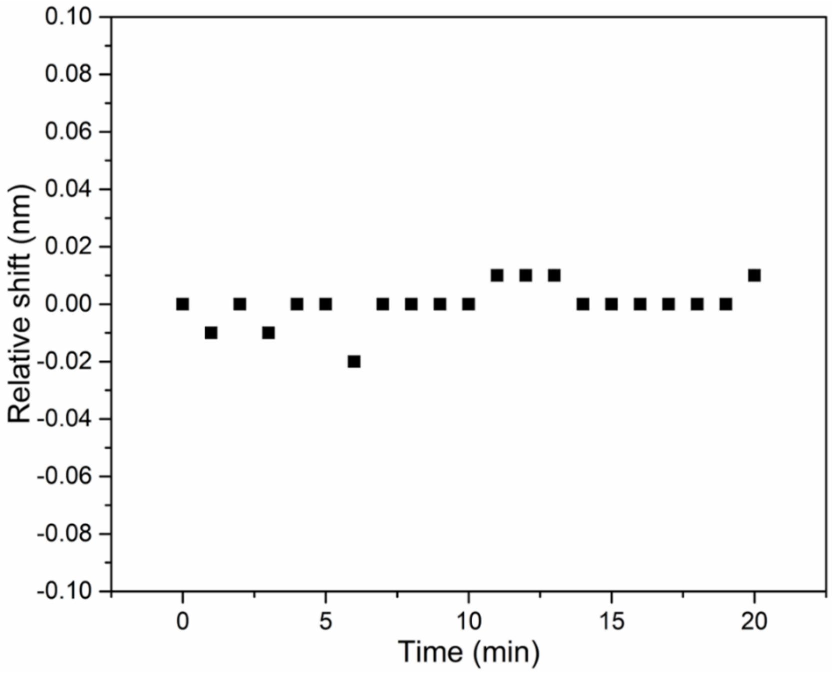

Figure B.3 Relative shift in SPR peak recorded for bound streptavidin on immobilized biotin-cysteamine complex on CSRGs surface from t = 0 min to t = 20 minutes, with 1-minute interval between signal acquisition.

References

(1) Nair, S.; Escobedo, C.; Sabat, R. G. Crossed Surface Relief Gratings as Nanoplasmonic Biosensors. ACS Sensors 2017, 2 (3), 379–385. https://doi.org/10.1021/acssensors.6b00696.

Appendix C

Supplementary information to Chapter 8

With minor changes to fulfill formatting requirements, this Appendix is substantially as it appears as supplementary Information in: Srijit Nair, Juan Gomez-Cruz, Gabriel Ascanio, Aristides Docoslis, Ribal Georges Sabat and Carlos Escobedo. Sensors, 2021.

Contact angle measurements

The wetting state of surfaces is often used to evaluate bactericidal properties of both bioinspired and natural nanostructured materials [1,2]. In that context, the wetting state of the bioinspired TS-CSRGs and the cicada wings were compared through contact angle (CA) measurements. Figure C.1 shows images of the profile of microdroplets on the wings of the cicada *Neotibicen canicularis* and on the TG-CSRG structures, taken during the CA measurements, as described in Section 8.2.6. The resulting CAs demonstrate similar hydrophobic properties with contact angles of 115°±2.075° and 119°±3.4222° (n=5) for the cicada wings and the TS-CSRG, respectively.

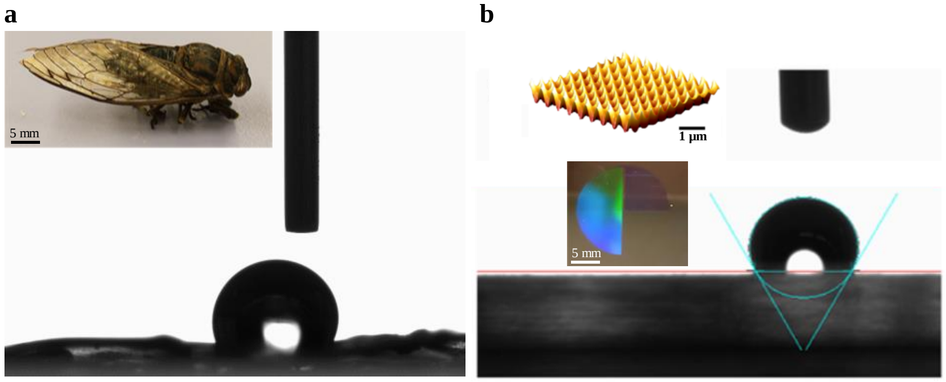

Figure C.1 Images taken during contact angle measurements of a DI water droplet atop the surface of a) a piece of wing from a cicada Neotibicen canicularis (inset: cicada used as sample source); and b) an Ag TS-CSRG (inset: TS-CSRG, left; AFM scan, right).

Preparation and inspection of the TS-CSRG SERS substrates

The template stripping process to fabricate the TS-CSRGS is shown in the pictures in Figure C.2. Macroscopic and microscopic optical inspection of the nanostructures was performed in order to evaluate the successful preparation of the SERS-active substrates. Figure C.2a shows the inscribed and silver-coated CSRG (methodology described in Section 8.2.2). The two orthogonal pitches of the CSRG were verified for accuracy by measuring the first-order diffraction angle from a low-power Helium-Neon laser and by using the grating equation. Subsequently, UV curable epoxy (NOA61, Norland Products Inc., NJ, USA) is spin-coated on top of the silver-coated nanostructures and a glass slide is carefully placed down and pressed uniformly to distribute the glue and remove any air in between. The structure is then exposed to UV light in an enclosed UV chamber (Novascan PSD-UV, Novascan Technologies Inc., IA, USA) for 30 min (Figure. C.2b). Once cured, the glass slide is meticulously removed to transfer the silver pattern. The excess of gDR1 is removed by rinsing with ethanol and DI water. Figure. C.2c shows Au TS-CSRG of 450, 550 and 600 nm successfully transferred to glass slides, which exhibit light diffraction patterns similar to the original CSRG.

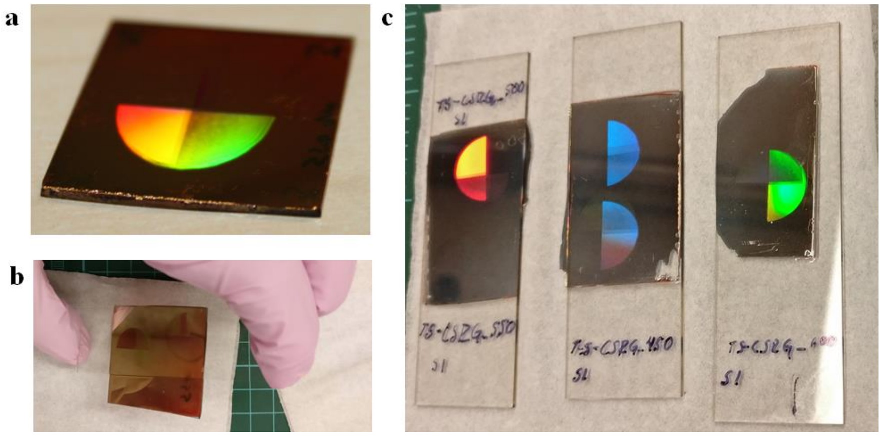

Figure C.2 CSRGs template stripping process. a) Silver-coated CSRG structure. b) Glass slide and CSRG structure after spin coating and UV exposure. c) TS-CSRG structures.

Scanning Electron Microscopy (SEM) Characterization

The surfaces of the Ag TS-CSRGs were investigated through the use of a high vacuum Scanning Electron Microscope (SEM) model Quanta FEG 150 ESEM (Field Electron and Ion Company, FEI, Oregon, USA) with BF/DF STEM detector, at 10kV. Figure C.3 shows images of TS-CSRG of 450, 500, 550 and 600 nm at magnifications of 16000x, 20000x and 25000x.

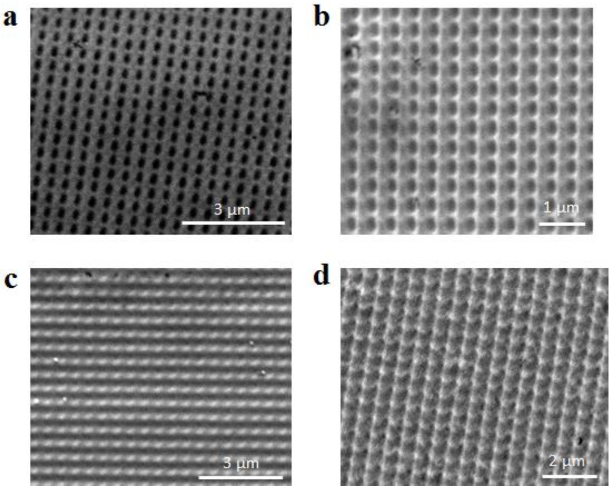

Figure C.3 SEM images of the Ag TS-CSRGs with pitches of a) 450 nm, b) 500 nm, c) 550 nm and d) 600 nm.

References

(1) Elbourne, A.; Crawford, R. J.; Ivanova, E. P. Nano-Structured Antimicrobial Surfaces: From Nature to Synthetic Analogues. Journal of Colloid and Interface Science. Academic Press Inc. December 15, 2017, pp 603–616. https://doi.org/10.1016/j.jcis.2017.07.021.

(2) Hasan, J.; Webb, H. K.; Truong, V. K.; Pogodin, S.; Baulin, V. A.; Watson, G. S.; Watson, J. A.; Crawford, R. J.; Ivanova, E. P. Selective Bactericidal Activity of Nanopatterned Superhydrophobic Cicada Psaltoda Claripennis Wing Surfaces. Appl. Microbiol. Biotechnol. 2013, 97 (20), 9257–9262. https://doi.org/10.1007/s00253-012-4628-5.